

Robot-based in-line measurement system for high-precision optical surface inspection

MASTER THESIS

Conducted in partial fulfillment of the requirements for the degree of a
Diplom-Ingenieur (Dipl.-Ing.)

supervised by

Univ.-Prof. Dr. sc. techn. G. Schitter
Dipl.-Ing. Dr. techn. E. Csencsics

submitted at the

Technische Universität Wien
Faculty of Electrical Engineering and Information Technology
Automation and Control Institute

by

Naverschnigg Christopher, BSc.
Matriculation number: 1326925
Graf-Starhemberg-Gasse 5/2/24
1040 Wien
Austria

Vienna, April 2021

Acknowledgement

At this point, I would like to offer my thank to all people who were there for me during my academic studies and who contributed in some way to the successful completion of the research work presented within this master thesis.

First and foremost, my sincere thanks go to my supervisor, Dipl.-Ing. Dr.techn. Ernst Csencsics, who supported me with his tireless effort, constructive feedback and by sharing his knowledge during many inspiring discussions over the whole course of this thesis. Next, I offer my gratitude to Univ.-Prof. Dr.sc.techn. Georg Schitter for the opportunity to write this thesis and his guidance, and to every other member within the Automation and Control Institute at the Technical University of Vienna, who participated in some way by creative talks or mental support.

I also want to express my sincere thanks to my friends, fellow students and work colleagues for your motivation, friendship and for the creation of unforgettable moments throughout the years of studies.

Finally, my deepest gratitude goes to my parents Brigitta and Johann for always putting their faith in me, their unfailing support and for being the reason why I am where I am at this point in life. At last, my special thanks go to my girlfriend Stefanie for her never-ending motivation, patience and affection over so many years. Thank you.

Abstract

Integration of metrology systems directly in the manufacturing process is seen as a key feature for future production lines to enhance product quality, manufacturing efficiency and to provide continuous information about manufactured goods. Fast, contactless inspection systems allow surface characterization, defect detection, dimensional inspection, and integration in industrial networks allows the adjustment of process parameters by utilizing measurement data. Industrial robots provide the necessary flexibility for the inspection of freeform surfaces and complex shapes. Optical inspection systems and sensors are a preferred choice due to their non-tactile character, submicrometre resolution and high measurement frequency but typically require a supplementary fine positioning system respectively actuation technique to perform a scanning motion. An additional positioning system also results as a consequence of limited accuracy and repeatability of industrial robots for both, pose and path.

Within the course of this thesis, a fully-automated robot-based in-line metrology system for optical surface inspection is designed and developed. A system based on a dual-stage approach consisting of a six-degree-of-freedom industrial robot arm for coarse positioning and additional stepper-motor-based linear stages is implemented as a prototype, which utilizes a triangulation sensor.

To provide necessary flexibility regarding sample size, optimally utilizing the optical sensor's measurement range and compensating for position and orientation deviations within a production line, feature detection, appropriate scanning trajectory selection and adjustment of the robot pose is performed. Based on the system requirements an error-budget is created, followed by a systematic analysis of individual system components to identify error sources and improve the overall performance.

For a measurement volume of $50\text{ mm} \times 50\text{ mm} \times 25\text{ mm}$ an out-of-plane resolution of $0.385\text{ }\mu\text{m}$, an accuracy of $3.4\text{ }\mu\text{m}$, a precision during a single scan of $22\text{ }\mu\text{m}$ and an overall repeatability for accumulative measurements of $7.2\text{ }\mu\text{m}$ is achieved.

Kurzzusammenfassung

Der Einsatz und die Integrationen von Messsystemen direkt in den Herstellungsprozess ist als essenzielles Element zukünftiger Produktionslinien angesehen um Produktqualität und Herstellungseffizienz zu erhöhen. Des Weiteren werden kontinuierlich Informationen über die hergestellten Güter bereitgestellt. Flexible und kontaktlose Inspektionssysteme ermöglicht die Charakterisierung von Oberflächen, die Detektion von Fehlstellen, Prüfung von Abmessungen und die entsprechende Anpassung von Prozessparametern. Industrieroboter bieten die notwendige Flexibilität um Freiformflächen zu inspizieren. Optische Messsysteme bieten kontaktlose Messung mit hohen Messfrequenzen und Submikrometer-Auflösung. Um eine Scanbewegung durchzuführen werden zusätzliche Feinpositioniersysteme benötigt. Dies folgt auch als Konsequenz der limitierten Positions- und Pfadgenauigkeit bzw. -wiederholgenauigkeit.

Im Rahmen dieser Arbeit wird ein voll-automatisiertes roboter-basiertes Messsystem für optische Oberflächeninspektion innerhalb einer Fertigungslinie entwickelt. Das System basiert auf einem „dual-stage“-Ansatz, welcher aus einem Industrieroboter mit sechs Freiheitsgraden zur Grobpositionierung und zusätzlichen schrittmotorbetriebenen Positionierplattformen besteht. Als Sensor, für das als Prototyp umgesetzte System, wird ein Triangulationssensor verwendet.

Um die notwendige Flexibilität bereitzustellen, Proben und Strukturen unterschiedlicher Größe zu vermessen, den Messbereich des optischen Sensors optimal zu nutzen und Positions- bzw. Orientierungsunsicherheiten innerhalb der Fertigungslinie zu kompensieren werden Möglichkeiten zur Objekterkennung, individuelle Scantrajektorien und Methoden zur Anpassung der Roboterausrichtung verwendet. Basierend auf den Systemanforderungen wird ein Gesamtfehler-Budget erstellt welches der Auswahl passender Komponenten dient. Anschließend wird eine systematische Identifikation von Fehlerquellen durchgeführt um deren Einfluss zu minimieren und die Systemperformance zu maximieren.

Für ein Messvolumen von $50\text{ mm} \times 50\text{ mm} \times 25\text{ mm}$ wird eine axiale Auflösung von $0.385\text{ }\mu\text{m}$, eine Genauigkeit von $3.4\text{ }\mu\text{m}$, eine Präzision während eines einzelnen Scans von $22\text{ }\mu\text{m}$ und eine Gesamtwiederholgenauigkeit aufeinanderfolgender Scans von $7.2\text{ }\mu\text{m}$ erreicht.

Contents

1	Introduction	1
1.1	Motivation	1
1.2	Challenges and Goals	2
1.3	Thesis Outline	2
2	State of the art	4
2.1	Sensing principles for surface and sub-surface inspection	4
2.1.1	Inspection methods	5
2.1.2	Overview and comparison	8
2.2	Actuation principles for precise positioning and scanning	9
2.2.1	Stepper motor-based actuators	9
2.2.2	Lorentz force actuators	10
2.2.3	Piezoelectric actuators	10
2.3	Scan strategies and trajectories	11
2.4	Role of industrial robots for metrology applications	12
2.5	Applied solutions and applications	14
2.6	Feature detection	15
2.7	Industrial communication and system architecture	15
2.8	Research objectives and questions	17
3	System concept and design	18
3.1	Sensor system	18
3.2	Workspace and requirements	19
3.3	Coarse to fine positioning system	20
3.4	Real-time data acquisition	22
3.5	Intelligent scan process	22
3.6	Error budgeting	22
3.7	Overview of the system requirements	27
4	System implementation and characterization	29
4.1	Main components of the prototype	29
4.1.1	Industrial robot arm	29
4.1.2	Stepper motor-based linear scan and positioning system	29
4.1.3	Sensor system	30
4.2	Mechanical components and adapter design	30
4.3	Intelligent scan and measurement process	34
4.3.1	Scan trajectory selection	35
4.3.2	Feature detection	37

4.4	Communication concept and sequence control	42
4.4.1	Communication concept	42
4.4.2	Sequence control	44
4.5	Experimental setup overview	46
4.6	Component performance verification	46
4.6.1	Linear stage performance verification	46
4.6.2	Industrial robot arm performance verification	54
4.6.3	Verification of the triangulation sensor behaviour	59
4.6.4	Summary of the verification process	61
5	Experimental validation of the system performance	62
5.1	Vibrations and acceleration forces	63
5.2	Out-of-plane resolution and precision	67
5.3	Measurement results	69
5.3.1	Repeatability	73
5.4	Robot pose adjustment	75
5.5	Error budget review	80
5.6	Specification overview	82
6	Conclusion and outlook	86
6.1	Conclusion	86
6.2	Outlook	88

List of Figures

1.1	Robot-based in-line measurement system for surface and material inspection.	2
2.1	Spot weld characteristics.	5
2.2	Lissajous pattern for (a) $f_x = 10$ Hz and $f_y = 11$ Hz, $T = 1$ s, (b) $f_x = 10$ Hz and $f_y = 12$ Hz, $T = 0.5$ s, (c) spiral trajectory.	12
2.3	Applied solutions.	14
2.4	Automation pyramid.	16
3.1	Overview of different robot configurations for individual workspaces, (a) Cartesian, (b) portal, (c) cylindrical, (d) spheric, (e) SCARA, (f) jointed arm.	20
3.2	Workspace environment.	21
3.3	Errors of linear stages due to manufacturing tolerances.	24
3.4	Provisional CAD-model of the metrology system based on the requirements.	28
4.1	3D printed elements of the prototype.	31
4.2	FE-analysis of the sensor adapter including the sensor.	32
4.3	Maximum frequency of stage movement when performing a raster trajectory, depending on the range of motion.	33
4.4	Adapter deformation due to accelerations of trajectories.	34
4.5	Spot diameter of the triangulation sensor (ILD1420) over absolute sensor distance (effective range 25 – 50 mm, points according to datasheet (continuous line), interpolation (dashed line)).	35
4.6	Resolution of a Lissajous trajectory based on Voronoi tessalation.	36
4.7	Resolution of a Lissajous scan depending on scan duration for an amplitude $A = 1$ mm (scan area: 2x2 mm).	37
4.8	Resolution of Lissajous scan depending on amplitude and scan duration.	38
4.9	Raster and Lissajous scan for the detection of features.	40
4.10	Scan area and detected edges (marked by black dots) for different scan durations (a-e) and scan result after $T = 10$ s (f).	41
4.11	Scan data and detected edges (marked by black dots) of a weld spot and its surrounding area, final data with and without edges (a-b), perspective view (c-d).	42
4.12	Communication structure of the prototype.	43
4.13	Sequence control of the measurement process for a single measurement location.	45
4.14	Prototype setup overview.	47
4.15	Measurement setup for the validation of the linear stage performance.	48
4.16	Drift of the measured displacement by the interferometer over time.	49
4.17	Standard deviation (STD) of the displacement drift within a moving window.	49

4.18	Position repeatability of the linear stages depending on the desired carriage position.	51
4.19	Position repeatability of the linear stages in the opposite direction depending on the desired carriage position.	52
4.20	Displacement profile (a) and velocity profile (b) of a movement over a distance of 50 mm, max. velocity: 120 mm/s, acceleration: 4000 mm/s. . .	53
4.21	Position error during a movement over the full range of motion.	54
4.22	Scaled image of the position error during a movement over the full range of motion.	55
4.23	Evaluation of repeatability by scanning reference samples and performing point cloud registration.	57
4.24	Illustration of the robot poses used during the evaluation process.	57
4.25	Translation (xyz) and orientation (PRY) for pose 1 and 2	58
4.26	Thermal drift of the triangulation sensor after switch-on.	60
4.27	Triangulation sensor turn on behaviour and disconnection of the robot joint's motor current.	61
5.1	Calibration samples for system verification, dimensions in mm.	62
5.2	Measurement setup to investigate the impact of acceleration forces on the mechanical structure of the system.	63
5.3	Triangular and sinusoidal trajectory for equal amplitude and frequency. .	64
5.4	Displacement due to raster and Lissajous trajectory for equal amplitude, frequency and maximum acceleration.	65
5.5	Displacement and acceleration of sinusoidal trajectories depending on the frequency.	66
5.6	Measurement setup to determine the resolution of the system.	67
5.7	Evaluation of the out-of-plane resolution for a displacement of 1 micro-step per second.	68
5.8	Evaluation of the out-of-plane resolution for a displacement of 15, 13 and 11 micro-steps during a scan movement.	68
5.9	Scan of a section of the reference sample using a coordinate-measuring machine (CMM), fixed lateral resolution of 50 μm	70
5.10	Raster scan of the reference sample, 50 μm lateral resolution in x.	71
5.11	Error normal to xy-plane between scans of the robotic measurement system and the CMM machine.	72
5.12	Scans of the reference sample with a rotation of 90° around the z-axis showing an identical periodic pattern along the x-axis.	73
5.13	Comparison of CMM (blue) and robot-based metrology system (red) for cross sections in yz (a-c-e) and xz (b-d-f) plane.	74
5.14	Error normal to the xy-plane between two scans of the robot-based system.	75
5.15	Comparison of least-squares and RANSAC algorithm.	77
5.16	Scan without repositioning (a), scan with optimal sensor distance after repositioning (b).	78
5.17	CMM-scan (a), sample in optimal distance (b) and scan in non-ideal distance (c).	79

5.18 Sectional view of the two smallest indentations at $x = 3$ mm.	80
5.19 Specifications of measurement system.	85

List of Tables

2.1	Comparison of applications and characteristics of NDT-methods.	9
2.2	Overview of six-degree-of-freedom industrial robots.	13
3.1	Overview of systematic and random errors.	26
3.2	Overview of the system requirements.	28
4.1	Main specifications of prototype components.	46
4.2	Measurement process of static analysis.	50
4.3	Robot repeatability for two poses, tool-center-point close to base and full extension.	58
5.1	Error standard deviation and mean value.	73
5.2	Overview of systematic and random errors.	82
5.3	Main specifications of prototype components.	83

1 Introduction

Over the past decades, industrial manufacturing has faced significant challenges under the impact of global trends. Resource efficiency, mastery of new technologies, flexibility and transparency, have developed to be the primary focus of production lines. In addition, a continuing interest in the increase of manufacturing efficiency and product quality sets a high demand on fast, precise, robust and flexible metrology systems [1] [2].

1.1 Motivation

In-line metrology eliminates steps such as unloading samples from the main assembly line, decreases the required time to detect problems within the manufacturing process, leads to a higher consistent throughput and enables the possibility of implementing statistical process control in order to identify equipment issues before they affect the final product [3]. Fast and contactless 3D-imaging and inspection systems allow material characterization, dimensional inspection and defect detection. Applications can be found especially in the automotive and aerospace sector, or semiconductor industry [4] [5].

The resolution of commonly used camera-based inspection systems, utilizing passive or active stereo vision, is proportional to the field of view and set by the camera system's design. Maximum resolution can only be achieved by decreasing the field of view, which results in a smaller scan area. To overcome this limitation and enable scans with micro-down to submicrometre resolution for varying sizes of measurement samples in the production line, optical measurement techniques are used. Optical metrology systems can provide fast scans with high lateral and in-plane resolution and are a preferred choice due to their non-tactile character [6].

Industrial robots with up to six degrees of freedom are indispensable in industrial manufacturing and are of growing importance for metrology tasks, e. g. the inspection of complex shapes. Nevertheless, their accuracy and repeatability for poses and paths are limited to multiple tenths of micrometres and therefore not suitable for high precision metrology on the micro- and submicrometre scale [7] [8].

Additional positioning platforms, e. g. voice-coil actuated or stepper motor based linear stages, which are mounted on the flange of the robot arm, lead to a dual-stage approach (coarse to fine positioning), which is a common choice if the desire for a wide range of motion has to harmonize with the need for a precise position and scan concept [9] [10].

The concept of an in-line metrology system utilizing a dual-stage approach, consisting of an industrial robot and an additional actuator system, equipped with an application-specific sensor system is illustrated in Figure 1.1.

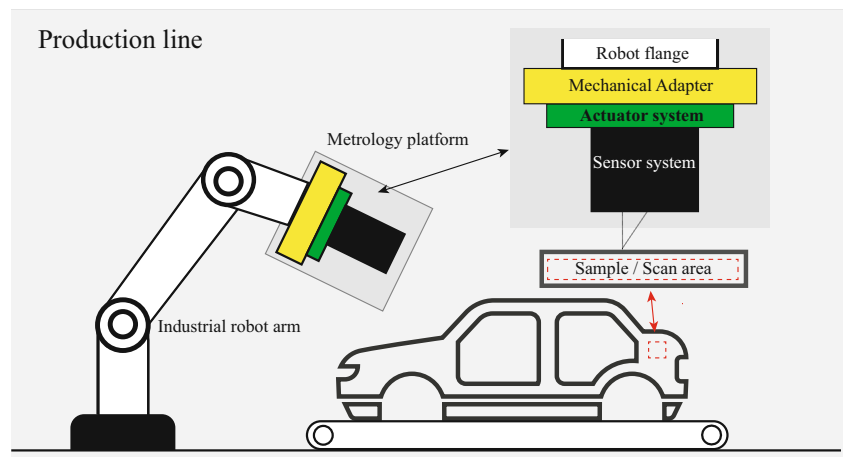


Figure 1.1: Robot-based in-line measurement system for surface and material inspection.

1.2 Challenges and Goals

Motivated by the need for a flexible fully automated robotic in-line surface inspection system, designs for a compact high-precision positioning and scanning system and their integration with appropriate sensor technologies are required. To supply additional flexibility and to be able to compensate for tolerances within the manufacturing process or the production area, the system should be able to detect relevant features and adjust scan parameters under the condition of optimal utilization of the measurement range. A flexible interface and communication structure is desired that allows integration of the system into already existing industrial networks and provides precise synchronization of position and sensor data during a scan process. This requires a solid understanding of the overall system, the interaction of components and the analysis and characterization of possible error sources to maximize precision and system performance.

In this relation, the main goals of this thesis are defined as follows:

- Design of a robot-based in-line metrology system for high-precision optical surface inspection and 3D-imaging with single micrometre resolution, accuracy and repeatability
- Selection of components, suitable hardware and software interfaces and creation of a fully automated process control
- Practical prototype implementation
- Experimental validation of the system performance

1.3 Thesis Outline

In this theses a fully automated robotic in-line metrology system is designed, prototyped and evaluated. Chapter 2 provides an overview of the current state of the art, regarding

3D-imaging, inspection systems and techniques, the role of industrial robots for metrology applications, actuation principles for precise positioning and scanning, and gives an overview of industrial communication concepts and system architectures. In the third chapter, the system requirements are analysed and the resulting information is used to derive the system specifications. Chapter 4 presents the prototype implementation with its components, software and hardware interfaces. Furthermore, different methods to improve the functionality and flexibility of robotic scan systems, e.g. trajectory selection, feature detection and robot pose adjustment for optimal utilization of the measurement range, are introduced. The fifth chapter presents the results of the experimental validation of the system performance. The last chapter summarizes the results and findings, and provides an outlook towards possible improvements.

2 State of the art

This chapter provides an overview of the current state of the art of inspection and 3D-imaging systems for freeform surfaces and their significance as part of the far greater sector of non-destructive testing. The essential role and growing importance of inspection systems, especially for in-line quality control and appropriate sensing principles and techniques, are discussed in the first part. Then the usage of industrial robots for metrology tasks is described. This is followed by the different state of the art actuation principles to fulfil the demand for a precise positioning and scanning motion depending on the desired resolution, speed and force. In extension to actuator systems, scan strategies and trajectories are discussed. Afterwards, an overview of applied solutions and applications is given. The chapter closes with an introduction to typical industrial communication concepts and system architectures, which allow integrating a robotic metrology system into an already existing industrial network and serve as a link between internal system components.

2.1 Sensing principles for surface and sub-surface inspection

This section starts with a short review of the year 2019. In that year, 67 million cars were produced worldwide, which is equal to a daily amount of around 183.000. A typical body-in-white (car body) consists of about 300 sheet metal parts, which have to be joined by approximately 4000 spot welds [11]. The analysis of at least 1% of them, especially of those which are of critical importance is desired to prevent failure during operation.

Spot weld quality refers to the static strength (e.g. tensile-shear, cross-tension and peel strength) and dynamic strength (impact and fatigue strength) of the spot weld, but is typically related to the physical attributed such as nugget size, penetration and indentation depth and size of the heat-affected zone [12]. This is illustrated in Figure 2.1. The main criterion is the nugget diameter which is selected depending on the metal sheet thickness, according to DIN EN ISO 18595. AWS D8.9M [13] specified that the surface indentation depth reflects the spot weld's static strength and could therefore also be used as a quality criterion. This requires precision measurement of the weld indentation [14]. Improper welding parameters affect the main characteristics and can lead to surface and subsurface defects, e.g. cracks, porosity and slag inclusions.

Different techniques have been developed to fulfil these and similar tasks, such as defect detection, characterization of surfaces, dimensional inspection, and material analysis. Non-destructive material testing has become an essential aspect of multiple industrial fields to enhance product quality and manufacturing efficiency. The downside is that, compared to manufacturing itself, non-destructive testing can be the slowest aspect in a production process and can lead to a bottleneck [15].

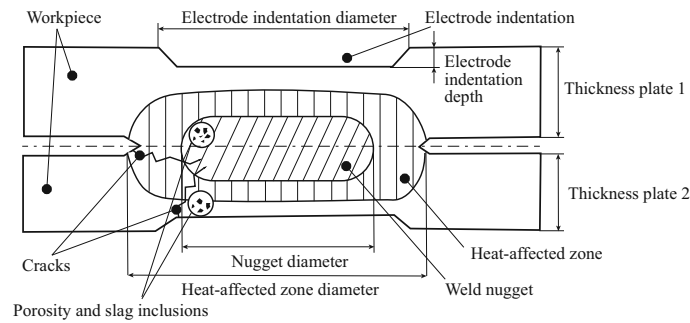


Figure 2.1: Spot weld characteristics.

Complex testing techniques are often carried out manually which requires trained technicians. This leads to an overall slow process, and it is challenging to achieve consistent repeatability. Therefore, there is a need for fully-automated, fast and preferably contactless in-line measurement systems.

2.1.1 Inspection methods

This thesis's focus rests on surface inspection, but additional methods for subsurface inspection are discussed briefly for the sake of completeness, and to illustrate that robot-based in-line metrology systems can also be equipped with different sensors depending on the application. The different techniques are split as follows, and their strengths and limitations will be discussed within the course of this chapter.

- Visual measurement and 3D imaging techniques for surfaces
 - Camera-based inspection
 - Optical sensing techniques
- Surface and subsurface defect detection
 - Eddy current testing
 - Magnetic particle testing
 - X-ray testing
 - Infrared thermography
 - Ultrasonic testing

Visual inspection and 3D imaging techniques for surfaces

Visual inspection is a standard technique in industrial processes and has high automation potential. Different systems depending on object size, desired resolution and image rate exist. Camera-only systems can provide high-resolution images, and by using stereo techniques, depth information can be obtained. Stereo Vision itself can be divided into

active and passive stereo with sub-techniques, respectively.

In active methods the illumination of a light source or a pattern is modulated, either temporally or spatially. Many active stereo methods are based on the human perception of shaded surfaces to extract the 3D shape of an object. Shape from shading aims to estimate depth information from one single image which leads to a mathematically complex problem structure. Therefore photometric stereo utilises multiple images under different lighting conditions to estimate 3D shape from shading cues [16]. Structured light projects patterns onto a surface which can be used to calculate heights of structures by finding correspondences between coordinates of a camera image and those of a projector image. On the other hand, passive stereo vision uses two cameras. This technique requires knowledge of camera parameters and precise calibration to compensate for aberrations and lens distortions. In addition, the most important aspect when using camera systems in an industrial environment is to provide constant light and illumination conditions. Commercial stereo vision systems with a field of view of several millimetres, a lateral resolution down to $6.7\ \mu\text{m}$, an accuracy (xyz) of $6\ \mu\text{m}$ and an out-of-plane repeatability down to $0.2\ \mu\text{m}$ are available. The image frequency is usually limited to a maximum of 10 Hz [17]. Due to the properties of the camera's lens system and sensor size, the desire for a larger field of view comes with a deterioration of resolution, accuracy and repeatability.

Next to camera systems, different optical sensor systems are used. Triangulation sensors determine the distance to the target by projecting a laser point onto the object surface. The scattered light is reflected onto a detector. Significant advantages of those sensor type are high accuracy, repeatability and insensitivity to illumination and surface texture. Measurement ranges of several hundred millimetres, resolutions in the sub-micrometre range and measurement rates up to 100 kHz can be achieved. Commercial triangulation sensors are available with resolutions down to 30 nm [18] [19]. Triangulation sensors are available as single-point measurement systems or line sensors.

Chromatic confocal sensors utilise chromatic aberrations of lens systems for optical distance measurement. A focused white light beam is sent through the optical system, which leads to a spread of the focal points of different wavelengths along the optical axis. The reflected light is analysed by a spectrometer. Therefore, the dominantly reflected wavelength determines the measured proximity. Chromatic confocal sensors are suitable for highly reflective, transparent and diffuse materials, even for liquids [20]. Commercial confocal sensors are available with resolutions down to 3 nm, minimum spot sizes of $3\ \mu\text{m}$ and sample rates, depending on the controller, up to 70 kHz. It has to be considered that higher requirements on the resolution are inversely proportional to the measurement range. Therefore, common chromatic confocal sensors with nanometre resolution usually have measurement ranges of a few hundred micrometres [21].

Surface and subsurface defect detection

Eddy current testing utilizes a current with a frequency in the range from kHz to MHz through a coil which generates a magnetic field. By the laws of electromagnetic induc-

tion, an eddy current is induced in a sample close to the coil. Material defects affect the behaviour of the eddy current, which produces a magnetic field by itself and can be inspected by using another coil or by measuring the impedance disturbance in the primary coil. This method is suitable to detect defects near the surface and has adequate automation potential. Nevertheless, the transducer needs to be close to the surface, which sets high demands on position accuracy, and eddy current testing is only applicable for conductive materials.

Magnetic particle testing is one of the oldest non-destructive testing techniques but is still extensively used in the surface crack detection of welded components. A ferromagnetic sample is subjected to a magnetic field, which is created by a permanent- or an electromagnet. Besides, a dry or wet suspension containing magnetic particles is applied to the surface. Discontinuities in the materials create an inhomogeneity of the magnetic field lines. Therefore, surface or subsurface cracks lead to a leakage field and lead to a clustering of magnetic particles at the defect area. Commonly high-ampere low-voltage current is used for testing. Alternate current is used when only surface defects are of interest since only the surface is magnetized. Direct current magnetization is more sensitive in detecting subsurface discontinuities. In general, discontinuities along the magnetic field lines can not be detected [22].

X-ray computed tomography (CT) is a common technique for analysing inner structures of materials and organisms. More recently, CT technologies are applied for dimensional metrology as an alternative to tactile or optical measurement systems. A measurement setup consists of a X-ray source and a detector. The source generates X-rays which propagate through a sample. The rays are attenuated depending on the travelled distance, material composition and density. By performing scans from different orientations, 3D reconstruction can be used to create a 3D voxel model. [23] The resolution of standard laboratory CT systems is in the range of multiple micrometres. However, systems with a resolution of around 100 nm have been published [24]. While typical laboratory-based scans can take upwards of 30 minutes rapid scan systems from modified airport baggage scanners allow real-time imaging with exposure times of 100 μ s [25].

IR thermography uses an infrared camera to detect temperature distribution or heat flow in a material. In non-destructive testing applications, active thermography is used by exposing the material to a laser or flashlight excitation. Measurements can be performed in single-sided reflective or double-sided transmission mode depending on the thickness of an object and its structural properties. Temperature resolution, spatial resolution and frame rate are the most critical parameters. The resolution of mainstream infrared thermal imagers has reached 0.01 °C and is, therefore, suitable for non-destructive-testing and inspection systems[26]. Systems for laser-based spot weld characterization are reported [27] [28].

Ultrasonic testing is performed by using an ultrasound source, for the excitation of broadband ultrasonic waves in materials or structures, and a detection system. Common measurement systems use either piezoelectric transducers as an ultrasound source which

are coupled to the sample or excitation lasers, while the detection is done by using laser-vibrometers [29]. The attenuation, velocity and spectrum of the signal changes depending on material properties and structures. To create a scan of an area, the point of excitation and detection, respectively are varied. All these technologies have their limitations. Piezoelectric transducers are cost-efficient but require contact to the surface and the usage of a coupling agent. Therefore, reproducible contacting is necessary for robust measurements over multiple samples which complicates integration into a fully automated process. The performance of vibrometry strongly depends on surface properties (reflectivity, roughness) of a sample [30]. More recently an optical microphone is used for the detection of ultrasonic waves. The optical microphone is based on a Fabry-Pérot etalon and has no moveable parts compared to common membrane-based microphones and can, therefore, achieve a high bandwidth between 5 Hz and 1 MHz [31].

2.1.2 Overview and comparison

The following Table 2.1, gives a summary of non-destructive-testing (NDT) techniques and their advantages and disadvantages, respectively.

Application	Method	Advantages	Disadvantages
Surface characterization, surface defect detection, 3D-imaging, dimensional and freeform surface inspection	Active stereo vision	High image rate independent of area size	Fixed field of view by design
	Triangulation laser	micro- to submicrometre resolution, high measurement range, high flexibility	Different laser sources necessary to cover specific material types like glass
	Chromatic confocal sensor	No limitation by material or geometry, nanometre resolution, allows double sided measurement (e.g. lenses)	Limited measurement range, sensitive to angle of incidence
Internal defect detection, 3D-imaging, dimensional inspection	X-ray testing	No limitation by geometry	Strict installation and safety requirements, high cost
Surface and subsurface defect detection	Eddy current testing	Only for conductive material, fast, contactless, high automation potential	Edges of complex structures perturb the eddy current (edge effect)
	Magnetic particle testing	High sensitivity for defects, simple setup, intuitive interpretation of results	Limited to ferromagnetic materials, dry or wet suspension has to be in contact with the sample

Infrared thermography	Fast, large detection area, intuitive interpretation of results	Effective mathematical model needed for defect depth evaluation, especially for complex shapes, low subsurface detection depth
Ultrasonic testing	High sensitivity for defects, fast and contactless, can also be used for dimensional inspection with appropriate data analysis	Interpretation of results can be challenging and gets more sophisticated with increasing complexity of structure

Table 2.1: Comparison of applications and characteristics of NDT-methods.

Especially single point measurement systems require additional positioning systems to perform a scanning motion to obtain a 3D-image. Therefore, different actuation principles will be discussed in the following section.

2.2 Actuation principles for precise positioning and scanning

The selection of an appropriate actuator depends on different factors like required accuracy, resolution, bandwidth and actuation range. The following types are commonly used for high-precision positioning:

- Stepper motor-based actuators
- Lorentz force actuators
- Reluctance actuators
- Piezoelectric actuators

2.2.1 Stepper motor-based actuators

Stepper motors are widely used in industrial applications such as robotic systems and CNC-machines in which requirements for high acceleration and speed, precise positioning and high torque have to be fulfilled. Over time three main types have emerged, reluctance-, permanent magnet- and hybrid stepper motors. In general, the design of stepper motors is defined by the number of stator coils, that can be independently excited to control the direction of the magnetic field, and by the number of poles on the rotor. Reluctance motors have an iron rotor without additional permanent magnetic elements. The force or torque is based on the change of the magnetic resistance (reluctance) during the rotation. For a permanent magnet stepper motor, a specific number of magnetic pole pairs is attached to the rotor. Hybrid stepper motors combine both types to achieve small stepsizes and high forces and torque by using a multi toothed construction for each pole pair.

The motor torque contains an electrodynamic component, a cogging torque due to mechanical rotor design and a component due to the reluctance effect [32]. In order to provide stepwise movement, the basic algorithm is full-stepping, where only one phase is excited at a time which results in 4 steps per rotation. When both phases are excited simultaneously, a stable operating point between two stator teeth is obtained, which is called half-stepping. In order to achieve higher resolution, additional setpoints are introduced by only using a fraction of the maximum coil current. For precise positioning, each step of a stepper motor, with multiples of a hundred steps per revolution, can be divided into multiple micro-steps to increase the resolution by a factor of up to 256 in commercial stepper motors [33]. To transfer the rotational movement into a lateral displacement for linear stages, precision lead screws and threaded spindles are used, which provide an additional ratio of gearing [34].

2.2.2 Lorentz force actuators

Lorentz actuators are predominantly applied in high precision positioning systems due to their low mechanical stiffness between the stationary and moving part. Low stiffness reduces the transmissibility of external motions which are transferred via the mechanical structure. These movements can be caused by floor vibrations or due to the excitations of eigenfrequencies in the support structure. A downside of the basic Lorentz actuator is a relatively modest force to current ratio and range of motion. The principle of the Lorentz actuator can be described by using the equation of the Lorentz force:

$$\mathbf{F} = q(\mathbf{E} + \mathbf{v} \times \mathbf{B}) \quad (2.1)$$

A basic configuration uses a high-efficiency permanent magnet configuration and a coil which sits partly within the magnetic air gap. The magnetic field lines are perpendicular to the direction of the current. Different variants have been developed to increase the performance of the basic configuration. Several coils and electronic commutation can be used to extend the range of motion. Zero-stiffness actuators can be achieved by suspending the moving part by air feet or magnetic levitation. This requires a heavier and larger mechanical structure but allows the suppression of errors within a range of ± 10 nm. In general, a trade-off between desired stiffness, acceleration and bandwidth has to be found [35].

Linear Lorentz actuators with a range of motion of several hundreds of millimetres and a minimum incremental motion of multiples of nanometres are available [36].

2.2.3 Piezoelectric actuators

Piezoelectric actuators are based on the inverse piezoelectric effect. A voltage applied to the electrodes at the piezo-surface creates an electric field which leads to an expansion of the piezoelectric material. Their main advantages are high resonance frequencies and sub-nanometre resolution. In addition, due to their high stiffness, high bandwidth and actuation forces of several kN can be achieved. The downside of high stiffness is high transmissibility for vibrations. Also, piezoelectric materials suffer from multiple effects

during operation and over time like creeping, hysteresis and ageing effects. Multiple commercial nanopositioning systems are available [37].

2.3 Scan strategies and trajectories

The selection of appropriate scan trajectories is an essential part of the design of a scanning system to achieve high scan speeds, high resolution and to utilize the maximum system bandwidth. Different subcategories of scanning probe microscopy, e. g. scanning tunnel microscopy, atomic force microscopy, and laser scanning applications require trajectories which are adapted to the system to increase the overall performance [38].

Fundamental raster scans remain the principle scan trajectory in both commercial and research applications [39]. Raster scans provide uniform resolution and distance between data points when using a fixed sample rate. Raster patterns are obtained by applying a triangular wave form to the fast axis and a ramp signal to the slow axis. Triangular waveforms contain all odd harmonics of the base frequency whose amplitude attenuates with $1/k^2$, where n denotes the harmonic number [40]. This can introduce mechanical resonances in the mechanical structure on turning points due to high acceleration forces, which might limit the bandwidth of a scanning system.

Recently attention has been shifted to Lissajous trajectories as an alternative to classic raster scans [41]. Lissajous trajectories provide a smooth acceleration profile, and their driving frequencies typically dominate their frequency spectrum. Besides, they provide an overview of the scan area within a small proportion of the duration. This property can be utilized when detection of features within the scan area is desired.

Lissajous trajectories are created by performing sinusoidal movements with different frequency in orthogonal scan directions. The trajectory is centred at X_0, Y_0 and defined by the peak-to-peak values X_{pp} and Y_{pp} . In the following equations (2.2) and (2.3) f_x and f_y denote the driving frequencies which determine the duration T and the shape of the trajectory. The duration can be calculated according to (2.4), where lcm denotes the least common multiple [42].

$$x(t) = X_0 + \frac{X_{pp}}{2} \sin(2\pi f_x t) \quad (2.2)$$

$$y(t) = Y_0 + \frac{Y_{pp}}{2} \sin(2\pi f_y t) \quad (2.3)$$

$$T = \frac{lcm(\frac{1}{f_x}, \frac{1}{f_y})}{f_x f_y} \quad (2.4)$$

Typically a small shift of the frequency can lead to a drastic change in shape, duration and resolution of the frequency. The properties of the least-common-multiple of two numbers can be utilized when a desired duration should be achieved. Selecting only integers and a prime number for one driving frequency always results in a duration of $T = 1$ s. By selecting non-prime integer frequencies, the resulting durations show a $T = \frac{1}{k}$ behaviour,

i.e. $T = 1\text{ s}, 0.5\text{ s}, 0.33\text{ s}, 0.25\text{ s}$ depending on the combination. In general, increased duration leads to a higher resolution. If a further increase of frequency is not possible, e. g. due to limited bandwidth, the duration can be increased above 1 s by using non-integer driving frequencies. Furthermore, both frequencies can be scaled by the same non-integer number, which leads to a linear change of the scan duration while the resolution remains constant for both frequency combinations. This can be utilized if frequency combinations for a certain resolution exceed the system bandwidth.

In figure Figure 2.2 two Lissajous patterns are shown, resulting from a variation of the frequency of one axis. An increased resolution comes with the cost of an increased scan duration.

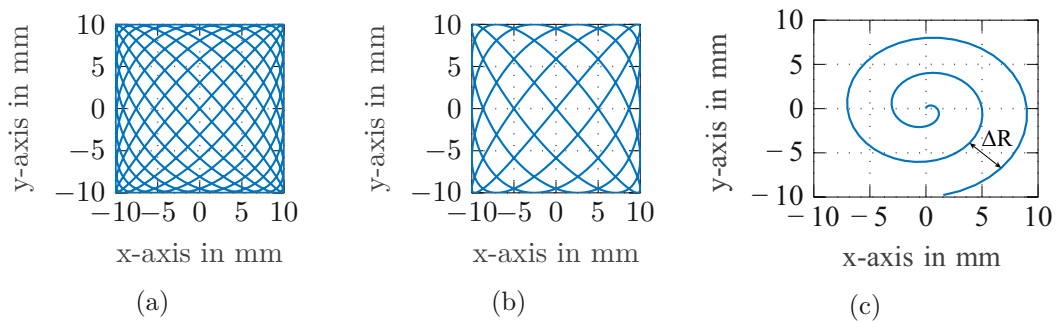


Figure 2.2: Lissajous pattern for (a) $f_x = 10\text{ Hz}$ and $f_y = 11\text{ Hz}$, $T = 1\text{ s}$, (b) $f_x = 10\text{ Hz}$ and $f_y = 12\text{ Hz}$, $T = 0.5\text{ s}$, (c) spiral trajectory.

While raster trajectories provide regularly distributed points over the complete area, which eases the definition of the spatial resolution, Lissajous trajectories lead to a varying lateral resolution. The resolution closer to the border of the scan area exceeds the resolution in the centre of the Lissajous figure, which typically shows the lowest value.

Next to raster and Lissajous trajectories, spiral trajectories are used in applications like atomic force microscopy [43]. A spiral pattern is obtained by applying sine and cosine signal with an identical frequency and varying amplitude to both axes as seen in Figure 2.2c. Similar to Lissajous trajectories frequency components which deviate from the base frequency can be suppressed. A constant change of amplitude leads to equal spatial radial resolution ΔR .

2.4 Role of industrial robots for metrology applications

High precision in-line metrology is seen as a key feature for future production lines to keep up with increasing demands on productivity, product quality and precision. Industrial robots enable additional flexibility regarding positioning, orientation and workspace size. Especially for complex structures and free-form surfaces robots enable dynamic repositioning and adjustment of a sensor head relative to the measurement sample. While

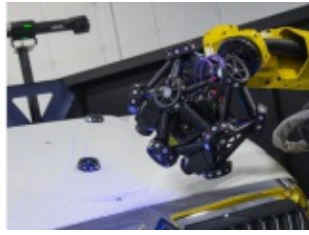
industrial robots are indispensable in modern production lines for pick-and-place, welding and general inspection tasks using camera systems, in general, they cannot be directly used for metrology tasks where a resolution of single micrometres is desired [44]. This is due to their limited path and pose accuracy where typically a maximum accuracy of $20\ \mu\text{m}$ can be achieved when the system has been properly calibrated. In [45], a robot equipped with a triangulation sensor without fine positioning or scan system was calibrated for metrology tasks. The results show that it is possible to perform metrology tasks with an error of approximately $50\ \mu\text{m}$. In addition, state of the art robots also use dynamic models to adjust control parameters when different loads are applied at the end-effector.

A large variety of industrial robot arms with a maximum working range between 1000 and 2000 mm, which enables sufficient flexibility in a large working volume, and a load capacity of 6 to 10 kg are available. In general, the load capacity is more than sufficient for metrology systems. Table 2.2 gives an overview of six-degree-of-freedom industrial robots from different manufacturers [46][47][48][49]. According to the international norm ISO 9283 (1998), most manufacturers only specify the pose repeatability. A pose repeatability down to $16\ \mu\text{m}$ is achieved for this working range and load capacity. In general, a higher working range and load capacity lead to a deterioration of the repeatability. Compact robots, e. g. the IRB120 by ABB with an operating range of 580 mm, and a load capacity of 3 kg can achieve a pose repeatability of $10\ \mu\text{m}$. Unlike other manufacturers, ABB also specifies the path repeatability for each robot, which can be up to 10 times the pose repeatability.

Manufacturer	KUKA	ABB	Fanuc	Yaskawa	
Type	KR 6 R1820	IRB 1600-6/1.45	ARC Mate 100iD/8L	Motoman MPX1950	
Pose repeatability	40	20	30	16	μm
Max. range	1820	1200	2032	1450	mm
Load capacity	6	6	10	7	kg

Table 2.2: Overview of six-degree-of-freedom industrial robots.

Especially in the automotive industry, aerospace and semiconductor sector fast, large-scale inspection of components, high resolution surface examination and defect detection, respectively characterization, for product and process optimization is desired, which led to a large variety of different metrology and inspection systems.



(a) Large scale inspection system based on active stereo vision



(b) Active stereo vision system



(c) Hybrid system combining active and passive stereo vision

Figure 2.3: Applied solutions [54][55][56].

2.5 Applied solutions and applications

Similar to Section 2.1 the subsequent solutions are divided into systems mainly for inspection tasks and defect detection on surfaces, which primarily utilize structured light due to high throughput, followed by robotic metrology systems, which utilize additional non-destructive testing techniques for surface- and subsurface inspection.

LMI Technologies offers various inspection sensors designed as a line scanner or based on structured light projection. These line scanners can achieve a lateral resolution down to $5.9 \mu\text{m}$ and an axial resolution of $1.1 \mu\text{m}$ with a line length of 10 mm and a measurement range of 6 mm [50]. Structured light systems with a lateral resolution down to $6.7 \mu\text{m}$ and an axial resolution of $2 \mu\text{m}$ are available with a corresponding field of view of $12.1 \times 13.2 \text{ mm}$ and measurement range of 7 mm [51]. An increase in the line length, field of view or out-of-plane measurement range always comes with a deterioration in axial and lateral resolution. In addition these sensor systems are compatible with industrial robots as shown in Figure 2.3b. Nevertheless the impact, e.g. of the robotic movement, on the overall accuracy is not defined and requires an additional evaluation process.

Furthermore, complete robotic 3D-scanning solutions for quality control and large-scale surface inspection are available, which are also mainly based on structured light projection as shown in Figure 2.3a. The accuracy is stated to be $25 \mu\text{m}$ while a volumetric accuracy of $78 \mu\text{m}$ for a working volume 16.6 m^3 is achieved [52]. State of the art systems based on stereo vision achieve an accuracy of $50 \mu\text{m}$ [53], see Figure 2.3c.

In [57] a robot equipped with an ultrasonic metrology system for the inspection of aerospace components is presented. The utilization of ultrasonic inspection allows the detection of surface and sub-surface defects. A robotic, in-line, stereo-camera assisted system equipped with an ultrasonic probe for the inspection of welding spots is stated according to [58]. The stereo-camera extends the functionality and flexibility of the metrology system by allowing the detection of the features position, i.e. weld spot. In-process calibration of a non-destructive testing system used for inspection of multi-pass welding is stated according to [59], which shows the application of a non-destructive testing system in

combination with robotic welding.

2.6 Feature detection

As discussed in previous chapters, robots show limited accuracy and repeatability for, both position and path. Also desired poses are either taught to a robot in a "teach-in" procedure or directly created by using CAD data. Especially in production lines where objects are constantly moving during assembly and inspection tasks, shifts in position and orientation can occur, which can impact the overall measurement result. By analysing car parts in the industrial field spot weld positions were found to deviate up to 19 mm from their desired positions [60]. Especially when using optical systems for surface inspection, these inaccuracies can lead to insufficient utilization of the measurement range. Besides, a non-parallel surface and scan plane, when scanning the sample, can lead to smearing of edges which varies depending on the scan speed and sample frequency. Therefore, robust measurement results are only possible when these inaccuracies are corrected.

To be able to correct distance and orientation of the robot tool-centre-point reference to the sample coordinate system the first step is to detect the sample itself or its feature points, e. g. on an assembly line or as a part of a bigger object. This can be done by using feature detection. For the following explanations, the measured surface profile can be seen as a two-dimensional image where each pixel's intensity is defined by the measured distance at specific xy-coordinates. Within this image, feature points can be thought of as corners, edges or to be more precise, areas with a fast change of intensity.

Feature detection is an essential aspect of machine vision which is part of a much broader subject called machine vision. This scientific sector has developed to be one of the fastest-growing fields in recent years and is an essential area of research due to the variety of applications. The goal of computer vision, in general, is to process images and provide results based on the observation. Machine vision refers to the use of computer vision in the industrial fields. Therefore many different algorithms have been developed, which can be used to increase manufacturing efficiency and enhance product quality. Nevertheless, many of those algorithms show huge differences when it comes to the computational effort, which is apparently even more noticeable with a growing amount of data [61].

Prominent representatives are the Canny edge detector [62], scale-invariant-feature-transform (SIFT) [63], speeded-up robust features (SURF) [64] and binary robust invariant scalable keypoints (BRISK) [65].

2.7 Industrial communication and system architecture

Large industrial facilities often contain thousands of automation devices with sensors, actuators and controllers being distributed over large areas. Different tasks within a facility set different demands regarding reaction times and reliability, sample rates and data size. Traditionally the flow of data and the assignment of devices with similar functionality to a hierarchical structure is defined by the so-called automation pyramid, which is shown in

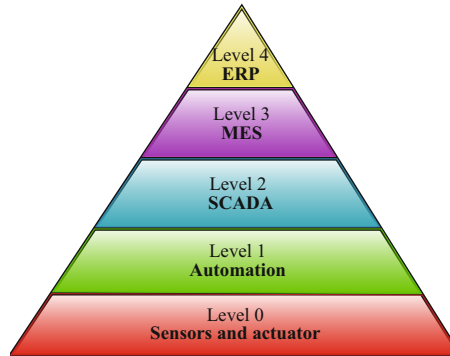


Figure 2.4: Automation pyramid.

Figure 2.4. The lowest level (field-level) contains sensors and actuators, which are in direct contact with the process. The task of the second level, the control level, is autonomous process control by using, for example, programmable logic controls (PLC) and utilizing devices based in the field-level to full-fill external requirements. These requirements are defined by the supervisory control and data acquisition (SCADA), which represents the third level. SCADA is used for the supervision of multiple processes by trained staff using suitable interfaces for visualization of process data and parameters, respectively. In the fourth level, which is also called the planing level, computer management systems known as manufacturing execution systems (MES) are used to monitor the workflow in a factory from raw materials to finished products. The enterprise resource planning level represents the top of the pyramid. It utilizes all previous level's technology and additional software for accounting, material management and logistics to achieve an efficient allocation of budget, operating materials and personal [66]. In general, the following concept applies, an increase of the level results in a growth of information while requirements on transmission speeds and real-time capability decrease [67].

In the early stages of industrial communication, fieldbus systems were developed to close the communication gap between the lowest levels of the automation pyramid with the initial ideal of the minimization of wiring tasks. Bus systems like PROFIBUS, controller area network (CAN), INTERBUS and DeviceNet have been developed. They mostly differ in achievable cable length, the number of bus participants and data bytes per package. Although the research was shifted to Ethernet-based networks (Industrial Ethernet) technologies to achieve higher data rates, traditional fieldbus systems were not replaced. This is due to the fact that many built facilities were developed before the era of industrial Ethernet [68]. Besides, Ethernet-based protocols like TCP, UDP and IP do typically not consider real-time requirements which prevented the development of one single Ethernet solution [69]. Today real-time Ethernet has become a standard in the industrial automation domain with cycle times below 1 ms. Representatives of this technology are PROFINET IRT, EtherCAT, Sercos III and Ethernet Powerlink [70].

The most commonly used automation device, which also serves as an interface between field- and SCADA level is the PLC. With the goal of non-proprietary, rational software cre-

ation the DIN EN 61131-3 serves as a foundation to provide a uniform concept for datatype and variable convention, program organization, syntax and tasks. PLC-programming allows utilization of five programming languages. While the ladder diagram, function block diagram and sequential function chart allow graphical programming, structured text and instruction list are characterized by textual programming. The program execution is based on a prioritizable, time-cyclic and event-oriented program control [71].

2.8 Research objectives and questions

State of the art shows that high precision in-line metrology faces several challenges depending on the application, positioning and sensor system. Structured light and stereo vision systems are commonly used due to their non-tactile working principle, large field of view, high speed and reasonable resolution, appropriate for their area of application. In addition, during image acquisition, the system is in a static position without moving mechanical elements. Nevertheless, the resolution is mostly limited to multiple tens of micrometres. To achieve higher resolution, typically optical sensor systems, e. g. triangulation sensors or confocal sensors, are used. Since industrial robots show a limited path and pose accuracy, repeatability and scan speeds, an additional scanning system is necessary to perform high-precision scanning motions. This leads to the formulation of the first research question of this thesis.

Research question 1:

Is it possible to create a robot-based metrology system for optical surface inspection that provides single micrometre resolution, accuracy and repeatability in axial and lateral direction?

In production lines static deviations between CAD-models, mechanical components or e. g. the position of samples on a conveyor belt are likely to occur within certain tolerance bonds. These can affect the resolution or even lead to an exceeding of the measurement range depending on the optical sensor systems. In addition, to maximize the overall performance, error sources have to be identified and separated into random and systematic errors, which can be handled by proper calibration of the system. Scanning systems require suitable trajectories for an efficient measurement process and to minimize the impact of acceleration forces and the excitation of structural modes. Therefore, the second research question can be formulated as follows:

Research question 2:

Can error sources of the robot-based metrology system components be captured in a systematic manner to improve measurement accuracy, repeatability and overall performance, and can this knowledge be used to optimize the measurement process?

3 System concept and design

The first step in creating a fully automated robot-based metrology system for surface inspection is to analyse the necessary requirements of the system and use the resulting information to derive the system specifications. In this chapter, suitable technologies for surface inspection, positioning and scanning are selected. Afterwards, the requirements for the acquisition and processing of measurement data will be outlined to fulfil the demands of a fast and efficient scan process. The requirements are evaluated based on the overall goal of creating a fully automated robotic in-line measurement system, which provides flexible surface inspection for manufacturing process and is capable of achieving micrometre resolution, accuracy and repeatability. In particular, the inspection of weld spots in the automotive sector is considered as mentioned in Section 2.1 which leads to concrete requirements of the system and its components.

3.1 Sensor system

First, a suitable sensor technology, capable of performing high precision surface measurements with a micrometre to submicrometre resolution is selected. As stated in the previous chapter, non-tactile surface inspection systems and 3D-imaging systems, can mainly be divided into camera-based systems and other optical systems. Camera-based systems require precise knowledge and calibration of the camera and its parameters. Furthermore, passive and active stereo-vision is not suitable for highly reflective or transparent materials. Due to the properties of the lens system and camera sensor size, a higher field of view leads to a deterioration of achievable resolution and accuracy. To provide the flexibility of covering a scan area of varying size, with a variable in-plane resolution and micro- to submicrometre out-of-plane resolution, an optical sensor system is a preferential selection.

Confocal sensors can achieve nanometre resolution but show a limited measurement range up to only multiple hundreds of micrometres when a maximum out-of-plane resolution is desired. In addition, these kinds of optical sensors are more sensitive to the angle of incidence but are suitable for all types of materials, e.g. matte, transparent and reflective surfaces.

Laser triangulation sensors have a measurement range of multiple tens of millimetres and micro- to submicrometre resolution and provide high versatility for an in-line inspection system, with the goal of achieving single micrometre resolution (cf. Section 2.8). Depending on the material and the application, different laser types can be used, for example, lasers with a wavelength in the range of 650 to 750 nm (red light) can achieve high intensity and are suitable for dark surfaces, which have a higher absorption coefficient, low reflectivity and coarse surface structures. On the other hand, blue-light lasers which have a shorter

wavelength provide the ability to scan liquids, glowing metals and transparent objects such as plastic or glass, by not being able to penetrate the object surface [72]. Furthermore, depending on the desired intensity and power, lasers are classified by their laser class according to DIN-EN 60825. In general, a higher laser class requires higher safety measures. Therefore, it might be necessary to assure that the triangulation laser is only active when the measurement head is close to the sample.

Following the inspection of weld spots or welding seams with varying geometrical structures depending on the sheet thickness, as mentioned in Section 2.1, a measurement range of multiple tens of mm is required to cover most applications. Simultaneously the characterization of surface properties (e.g. cracks, porosity) is desired, which requires micrometre to submicrometre resolution. This makes a triangulation sensor an appropriate choice. The weld and surrounding metallic surface can be considered as a matt surface with low reflectivity in hardened state, a red-light laser source is considered. This also offers high versatility for most other materials. Triangulation sensors can be carried out as single-point measurement systems or line scanners. Regardless of the type, an additional positioning system to perform a scanning motion is required.

3.2 Workspace and requirements

To satisfy the need for flexible manufacturing with a high level of automation, industrial robots are a common choice, with configurations regarding construction size, workspace size, degrees of freedom and performance depending on the field of application. Figure 3.1 shows an overview of typical configurations for robotic setups. In particular, these configurations represent systems based on serial kinematic and are a preferred choice over arrangements based on parallel kinematics due to lower complexity of the corresponding direct or inverse kinematic problems. Systems based on parallel kinematics typically provide a higher overall stiffness and velocity on the cost of workspace size. Nevertheless, the predominant proportion of industrial robots is based on serial kinematics. Cartesian, portal, cylindric and spheric configurations provide solutions with low complexity and limited degrees of freedom. SCARA robots (Selective compliance assembly robots) are a preferred choice for pick-and-place tasks or applications that require high stiffness in the z-axis. They come with one translative and three rotative degrees of freedom. Jointed robot arms provide the highest flexibility with up to six degrees of freedom (DOF) and allow positioning and orienting of a tool or the end-effector in every desired spatial pose. Therefore they are a preferable choice for inspection and testing tasks, especially when the sensor system has to be aligned depending on the surface curvature.

The main characteristics of industrial robots are their repeatability and accuracy for both poses and paths. Accuracy is a measure on how close an achieved position is to the desired position. Repeatability, on the other hand, is a measure of a systems ability to achieve identical results across multiple repetitions. While industrial robots, especially when used in the industrial field in "teach-mode", can achieve high position accuracy and repeatability, their ability to follow a path or trajectory is often lowered by a factor of ten.

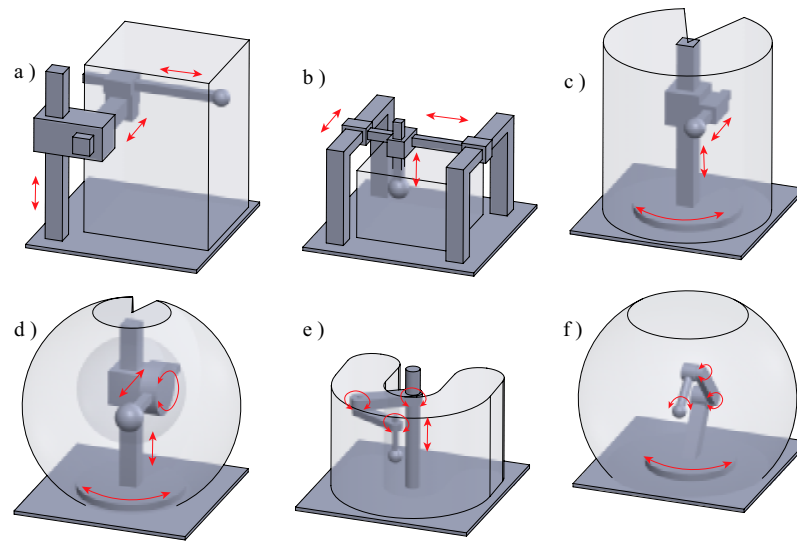


Figure 3.1: Overview of different robot configurations for individual workspaces, (a) Cartesian, (b) portal, (c) cylindrical, (d) spheric, (e) SCARA, (f) jointed arm.

Therefore, an industrial robot is not suitable for performing a precise scan movement with the desired micrometre accuracy and repeatability, and an additional fine positioning-, respectively scanning system is necessary to combine a large working volume of the overall design and flexible orientation of the metrology tool, with the task of high-precision optical surface inspection.

Depending on their desired working volume, industrial robots are available with an operating range of multiple metres. Typically the overall repeatability and accuracy decrease with an increasing construction size as discussed in Section 2.4.

The average car body shows a length of 4 to 5 m. This leads to the conclusion that high throughput, flexible spot weld inspection requires multiple 6-DOF industrial robot arms for simultaneous measurements with a reach of approximately 2 m, as illustrated in Figure 3.2. Nevertheless, the focus of this work lies on the design of a single system leaving aside the interaction of multiple systems and the merging of the acquired data. By considering an additional fine-positioning system, an optical sensor system and mechanical adapters a maximum applied load onto the robot end-effector of 2 kg is considered. This requirement can be fulfilled by a predominant part of available robots.

3.3 Coarse to fine positioning system

The main tasks of an additional fine-positioning system are point-to-point movements with high positioning accuracy and repeatability to minimize in-plane error, or the tracking of a scan-trajectory with desired acceleration and velocity. Depending on the application, speed, acceleration and frequency of movement and range of motion, a wide range of actuation principles are available, with linear actuators, in terms of either voice-coil-

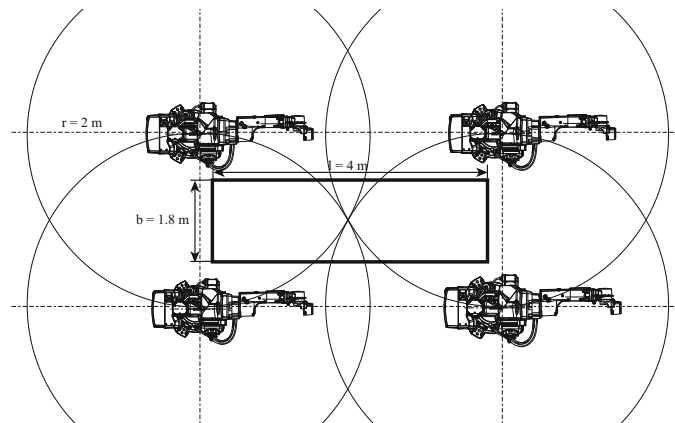


Figure 3.2: Workspace environment [73].

actuators or stepper-motor-based stages, being the most suitable choice. These linear actuators provide a wide range of motion of multiple tens to hundreds of millimetres, compared to, e.g. piezo-based actuators which are more suitable for applications where positioning with nanometre precision is desired. The downside of voice-coil actuators is their relatively low force to current ratio compared to their weight and construction size. Stepper motor-based stages can achieve high torque of multiple tens of Newton and provide a compact design while being able to keep up with micrometre precision, suitable for this application. Furthermore, due to the high torque, they support higher robot accelerations and velocity without the need for an additional locking mechanism to protect the carriage and the attached sensors.

A two-dimensional scanning motion can be achieved by a single actuator that provides a two-axis movement or separate linear stages. Single xy-actuators typically require a more robust mechanical frame which leads to an increase of the total mass. This can lead to a mass of multiple kg for a robust design [74], which is not appropriate for typical industrial robot arms as shown in Table 2.2. Compared to single-axis linear stages, they often offer a lower maximum velocity [75]. Therefore, to minimize the applied load onto the robot arm and provide maximum scan speed, an xy-scan system based on two stacked single-axis linear stages is preferred.

For a typical welding spot with a diameter of 5 mm a scan area of 5x5 mm is considered. A maximum scan time of 3 s is demanded to provide reasonable throughput. Linear stages with a velocity of at least 100 mm/s are available. By assuming a raster scan with a resolution of 100 μm and an acceleration 10 $\mu\text{m}/\text{s}^2$ of the upper stage of the stack, which performs the fast scanning motion (cf. sec:Types of scan trajectories), and carries a suitable adapter and the sensor system, with a maximum weight of 1 kg, a maximum thrust of 19.81 N is required for vertical orientation. A range of motion of at least 20 mm of both stages is demanded to provide flexibility for different feature sizes and to deal with uncertainties of the feature locations. As mentioned in Section 2.6, the actual position of spot welds can show an uncertainty of multiple millimetres. This also leads to

a requirement for the sensor system. To provide a spatial resolution of at least $50\ \mu\text{m}$ for the maximum velocity v_{max} , the measurement rate f_s should fulfil the following equation (3.1).

$$f_s > \frac{v_{max}}{50\ \mu\text{m}} \quad (3.1)$$

3.4 Real-time data acquisition

Depending on the application, surface structure, features, object size and most importantly, the used measurement principle, there are various scan strategies that can be realised. The easiest way is a trivial point-to-point scan with a fixed lateral shift of point of measurement and a defined measurement time in a steady position. While this is suitable for sensor systems which perform for example a long time measurements or whose measurement time is larger than the time needed to perform a lateral movement, point-to-point scans are not optimal for high speed measurement systems with a sampling rate of multiple kHz. Therefore a continuous scan movement is desired which requires synchronization of sensor and position data and can be achieved by utilizing real-time capable hard- and software. Cyclic data readout with a minimum cycle time equal to the maximum measurement frequency is demanded.

3.5 Intelligent scan process

In production lines fluctuations in the position or orientation of a sample or its feature, or deviations between a CAD-model and the actual product can affect the result of the inspection task. Optical sensor systems typically show a dominant focal point, e.g. due to the laser light's convergence. To minimize the scan duration, optimally utilize the optical sensor's measurement range and achieve maximum in-plane resolution robot pose adjustment is required. In-prior the position and orientation of the measurement target has to be determined, which requires feature detection and suitable data processing.

3.6 Error budgeting

In addition to the requirements an error budget based on dynamic error budgeting is created, which has proven to be an important tool to derive the total error of a system from dynamic contributors [76]. The goal is the creation of an overall error budget for the robotic metrology system by analysing and characterizing possible error sources of the system components. In general, all elements of a measurement system show deviations between their intended and actual performance, which may affect the measurement result and lead to an error. The error represents the difference between the measured quantity and the real value, which would be returned by a perfect instrument. Errors can be distinguished in systematic and random errors. Systematic errors either remain constant or show predictable behaviour over repetitive measurements. Identification of systematic errors allows the implementation of compensation measures. If they remain unknown,

they can not be compensated. Random errors are errors that vary in an unpredictable manner. These errors can only be characterized using statistical measures (e. g. probability distributions). In many cases random errors can be characterized by a normal distribution, defined by their mean value and standard deviation σ (STD). Random errors in signals can almost always be represented by this distribution. Measurement systems are often specified with either 2σ or 3σ [76]. Consequently, 95 % (99.7 %) of the signal values are varying within $\pm 2\sigma$ ($\pm 3\sigma$) around the mean value. Therefore, the error budget consists of all errors that are considered random and can't be compensated.

Environmental disturbances

For the application in the industrial field, environmental conditions can affect the precision of the metrology system. The main source of error results from ground vibrations and can lead to sub-micrometre disturbance of the measurement [77].

If metrology on nanometre-scale is performed, vibration compensation techniques are crucial. For the application of this thesis, ground vibrations can be considered as an additional random error under the assumption that passive vibration isolation measures are taken in the field of application depending on the required measurement accuracy. In [78] vibration measurements were performed in a production environment. A peak-to-valley value of 400 nm had been determined. By assuming a normal distribution an error with a standard deviation of $\sigma_f = 67$ nm resulting from floor vibrations is considered for this application.

Vibrations of the robot arm

Next to environmental disturbances, the robot arm's internal mechanical components can lead to vibrations in the submicrometre scale, which affect the measurement precision. Fluctuations can also arise from the noise of sensors that return respective joint angles to the controller, leading to a shake of the robot arm. This is considered a random error source if no actions are taken on the subordinate control. An resulting error with a standard deviation of $\sigma_r = 150$ nm is considered. Accuracy and repeatability are excluded from this evaluation since the robot is in a static position during the measurement.

Error sources of the sensor system

Electronic noise arises from internal components of the sensor system. Typical types of electronic noise are thermal, shot, excess (also known as one-over-f noise), burst and avalanche noise [76]. For this application, a complete sensor system is used. Therefore the error budget represents a combination of these error sources. Typical triangulation sensors show a repeatability between 0.1 and $1\ \mu\text{m}$ [79]. For the error budget, the maximum value is considered, which results in a standard deviation of $\sigma_s = 333$ nm. In addition temperature stability of the sensors is specified to 0.01 to 0.015 percent of the measurement range. For a measurement range of 25 mm this can result in a thermal drift of up to $\Delta T_s = 375\ \mu\text{m}$. This is considered a deterministic error and is excluded from the error budget.

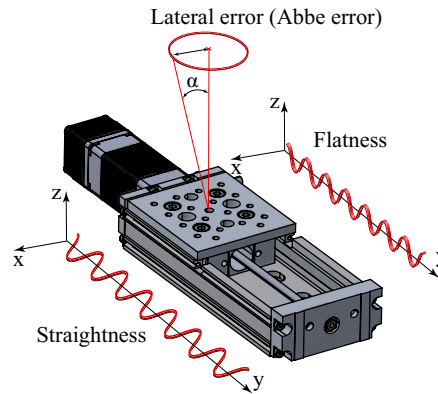


Figure 3.3: Errors of linear stages due to manufacturing tolerances [80].

Linear stage behaviour, flatness, straightness and Abbe error

Linear stages are typically characterized by their ability to perform repetitive movements defined by their repeatability. Precision stages can achieve a repeatability from multiple micrometres [34] down to [36] multiple tens of nanometres. Position repeatability introduces an in-plane measurement error for point-to-point measurements. For high-precision measurements a repeatability $< 2 \mu\text{m}$ is desired which results in a standard deviation $\sigma_p = 667 \text{ nm}$.

If a continuous scan motion is performed, position and sensor data have to be synchronized. Depending on the read-out principle of the linear stages' position data, the sample rate f_s of the sensor system might exceed the update rate f_p of the current position of the stage carriage. To utilize the full measurement rate of the sensor, the position data has to be interpolated. Following the assumption that the velocity control does not reduce the error between the desired and actual velocity to zero and might result in velocity fluctuation, a lateral error is introduced. By considering $f_s > 2f_p$ with $f_p = 1 \text{ kHz}$ and a maximum harmonic velocity fluctuation by 0.1% of the desired velocity v_d expressed as $v(t) = 10^{-3} \cdot v_d \cdot \sin(2\pi f_s t) + v_d$, a maximum lateral error of $3.2 \mu\text{m}$ arises. To simplify the estimation the amplitude of the fluctuation and the resulting error is assumed to be normal distributed which results in a standard deviation of $\sigma_d = 533 \text{ nm}$ considering the peak-to-valley value.

Furthermore, manufacturing tolerances due to limited precision of machine tools in mechanical parts production are omnipresent and can lead to errors when combined to a more complex system. For linear stages, these tolerances, e.g. the precision lead screw that guides the carriage, the surrounding mechanical guide, or the screw thread, can lead to multiple effects as shown in Figure 3.3.

Non-zero straightness of the stage leads to a displacement of the carriage over the range of motion along the x-axis, while non-zero flatness results in a displacement along the z-axis. In addition, the carriage can show orientation fluctuations around all three axes,

typically defined by Roll, Pitch and Yaw angle. RPY-angles correspond with rotations around zyx -axes. A combination of these rotations can lead to the so-called Abbe error [81]. Applied to the measurement system, first of all, this error leads to a lateral shift of the measurement point, which leads to an error between the expected and actual position of measurement. This error increases with the distance between the carriage plane and the mounting position of the sensor. Secondly, this results in an increase of the measured distance value under the assumption of a flat target parallel to the xy -plane of the measurement coordination system.

In theory, characterisation and compensation measures is feasible. Different measurement principles to analyse these error sources have been developed [82]. Also, complete systems that allow characterisation of these errors have been designed [83]. The successful compensation of the Abbe error for CMM's is stated according to [84].

Suitable stages from different manufactures in terms of range of motion, speed and thrust state specifications for straightness and flatness from $4\ \mu\text{m}$ [36] up to $7\ \mu\text{m}$ [34] and specifications for RPY-angles from 0.0057° [36] to 0.015° [34]. By considering the worst-case for two stacked stages and by assuming a normal distribution of the error, the straightness and flatness shows a standard deviation of $\sigma_{st} = 4\ \mu\text{m}$ in z -axis and a standard deviation of the lateral error of $\sigma_{fl} = 4\ \mu\text{m}$. The Abbe error due to a tilt of the stage carriage shows an error standard deviation of $\sigma_{az} = 0.087\ \mu\text{m}$ and $\sigma_{axy} = 27.83\ \mu\text{m}$, out-of-plane and in-plane respectively. It has to be noted that the assumption of a normal distributed error is not always permitted and only serves as an estimation in this case.

Data synchronisation

As discussed in Section 3.4 real-time capability of the soft- and hardware, used for data acquisition is demanded. Due to a minimum cycle time time-deviations due to runtime and internal processing of the stages controller and the sensor system may occur. By considering a minimum cycle time of $50\ \mu\text{s}$ and the required stage velocity of $100\ \text{mm/s}$ according to Section 3.3, an additional maximum lateral error of $5\ \mu\text{m}$ is introduced. This leads to a standard deviation of $\sigma_{sync} = 833\ \mu\text{m}$ by once again assuming a normal distribution of the error within the time frame.

Overview of the error budget

The following Table 5.2 gives a final overview of all error sources, their type and their standard deviation. In addition to the mentioned error sources, the impact of acceleration forces, emerging from the linear stages, has to be considered. Since the error depends on various factors such as stiffness of the robot joints, trajectory type and acceleration, an estimation is dispensed at this point. Nevertheless, the topic will be discussed in detail in Section 5.1. The repeatability of the robot arm has a neglectable impact compared to other dominant error sources and the impact is not determined at this point. The resulting error is split into a random and deterministic proportion since, in general, a

warm-up phase of sufficient duration is required to minimize the repeatability of the robot arm. This will be discussed in detail in Section 4.6.2.

Error type	Characterization	Quantity	
Random	Floor vibrations	σ_f	67 nm
	Robot vibrations	σ_r	150 nm
	Sensor noise	σ_s	333 nm
	Linear stage position repeatability	σ_p	667 nm
	Linear stage dynamic behaviour	σ_d	533 nm
	Data synchronisation	σ_{sync}	833 nm
	Robot repeatability		TBD
Systematic	Triangulation sensor thermal drift	ΔT_s	375 μm
	Abbe error of the linear stages (out-of-plane)	σ_{az}	0.087 μm
	Abbe error of the linear stages (in-plane)	σ_{axy}	27.83 μm
	Straightness of the linear stages	σ_{st}	4.66 μm
	Flatness of the linear stages	σ_{fl}	4.66 μm
	Robot warm-up phase		TBD
	Acceleration forces depending on trajectory		TBD

Table 3.1: Overview of systematic and random errors.

Under the assumption that the different random error sources are mutually independent normal distributed variables, their standard deviation can be combined by the method of the root of the sum of squares [76]. This leads to the following standard deviations, with the out-of-plane error σ_{zd} (3.2), the in-plane error for point-to-point measurements σ_{pxyd} (3.3) and the in-plane error for a continuous scanning motion σ_{cxyd} (3.4). The respective repeatability R_{zd} , R_{pxyd} and R_{cxyd} is defined by three times the standard deviation, as mentioned at the beginning of this chapter, this is a common specification for measurement systems. Robot and floor vibrations are considered to impact the in-plane and out-of-plane resolution. Nevertheless, all errors are mainly dominated by other errors sources, e. g. by the sensor noise and the behaviour of the linear stages, with the error due to synchronization having the largest impact on the in-plane error for a continuous scanning motion. These values represent the desired error values that should be achieved

by selecting appropriate components and will be compared to the achieved values of the prototype in Section 5.5.

$$\sigma_{zd} = \sqrt{\sigma_f^2 + \sigma_r^2 + \sigma_s^2} = 371 \text{ nm} \quad (3.2)$$

$$R_{zd} = 1113 \text{ nm}$$

$$\sigma_{pxyd} = \sqrt{\sigma_f^2 + \sigma_r^2 + \sigma_p^2} = 686 \text{ nm} \quad (3.3)$$

$$R_{pxyd} = 2058 \text{ nm}$$

$$\sigma_{cxyd} = \sqrt{\sigma_f^2 + \sigma_r^2 + \sigma_d^2 + \sigma_{sync}^2} = 1003 \text{ nm} \quad (3.4)$$

$$R_{cxyd} = 3009 \text{ nm}$$

Errors that are considered deterministic are not considered for the calculation. It has to be noted that the deterministic errors strongly exceed the random errors. This suggests that compensation of deterministic errors and calibration is crucial.

3.7 Overview of the system requirements

The analysis in the previous section leads to the following system requirements and minimum requirements for system components as listed in Table 3.2. Figure 3.4 shows an illustration of a schematic system design based on the requirements, consisting of a six-degree-of-freedom industrial robot arm, stacked stepper-motor-based linear stages as a xy-scan system, triangulation sensor and adapters for the components.

System requirements and design choices:

- High precision surface inspection with varying scan area in minimal scan time by utilizing non-tactile optical methods
- Micrometer resolution, accuracy and repeatability of the overall system
- Coarse and fine positioning system
 - Industrial robot with six degrees of freedom for the inspection of complex shapes within a large workspace
 - Additional fine positioning and scanning systems with micrometre precision
- Real-time capability of the system components with cycle times of multiple tens of microseconds, preferably equal to maximum measurement frequency of the sensor
 - Detection of a sample or feature points within the measurement volume
 - Re-adjustment of the robot pose to optimally utilize the measurement range

Component	Value		
Robot arm			
Degrees of freedom		6	
Maximum range		2	m
Load capacity		3	kg
Linear stage			
Travel range	\geq	20	mm
Velocity	\geq	100	mm/s
Thrust	\geq	20	N
Unidirectional position repeatability	\leq	2	μm
Triangulation sensor			
Resolution	\leq	1	μm
Sample rate	\geq	$v_{max}/50$	Hz
Wavelength	\sim	650 - 750	nm
Repeatability	\sim	1	μm

Table 3.2: Overview of the system requirements.

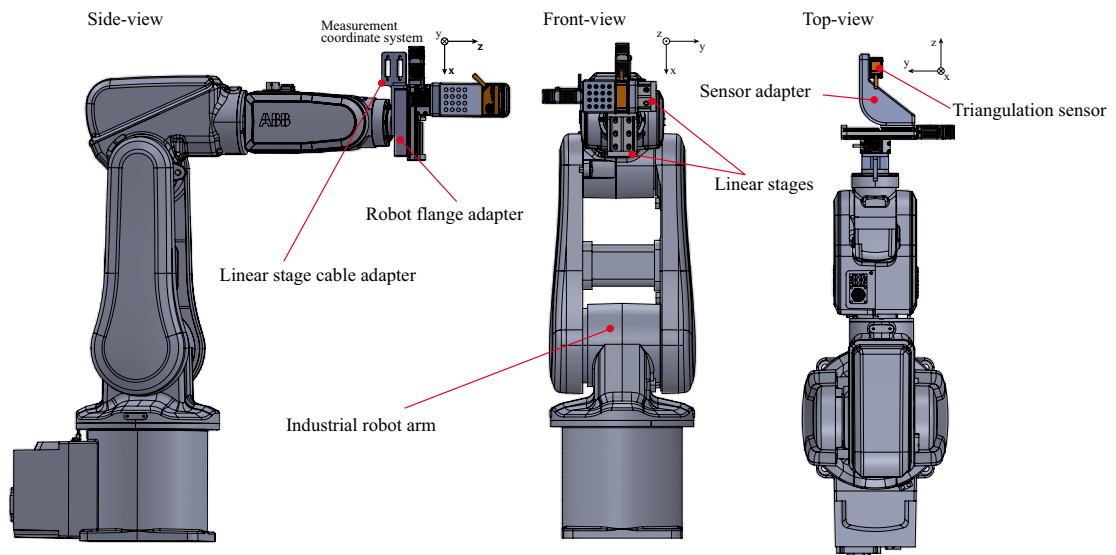


Figure 3.4: Provisional CAD-model of the metrology system based on the requirements.

4 System implementation and characterization

A prototype of a fully automated robot-based in-line measurement system for optical surface inspection is created based on the requirements defined in Chapter 3. In this chapter, the selected components are introduced and their specifications are listed. Furthermore, the used communication interfaces, software and sequence control is presented.

4.1 Main components of the prototype

4.1.1 Industrial robot arm

For the prototype of the metrology system, a six degree-of-freedom industrial robot arm (IRB120, ABB AG, Sweden/Switzerland) is used. The robot itself has a range of motion of 580 mm and with a weight of only 25 kg, therefore belongs to one of the most compact models provided by ABB. Nevertheless, this six-degree-of-freedom industrial robot has a load capacity of 3 kg and can achieve a maximum tool-centre-point (TCP) velocity of 6.2 m/s and a TCP-acceleration of 28 m/s². Position accuracy and repeatability according to the datasheet are equal to 20 μm and 10 μm . Regarding linear paths, the accuracy and repeatability lie in a range of 7 - 16 μm and 21 - 38 μm , respectively. These specifications, especially when considering a scan movement, once again show, that the robot itself is not suitable for performing high precision metrology tasks as already discussed in previous chapters. The robot is controlled by the standard motor controller (IRC5 compact, ABB AG, Sweden/Switzerland). The controller provides additional analogue and digital input/output modules and allows communication via PC- and Fieldbus interfaces (e. g. PROFINET, DeviceNet). In addition, an interface based on socket communication between the robot controller and Matlab is established to exchange information and send movement commands. The communication concept is explained in detail in Section 4.4.1.

4.1.2 Stepper motor-based linear scan and positioning system

The industrial robot arm is equipped with two stepper motor based linear stages (LSM050B-E03T4, Zaber Technologies Inc., Canada). The stages are stacked and serve as an xy-scan system with a maximum speed of 120 mm/s. Compared to commercial voice-coil actuated stages, these stepper motor based stages have a large travel range of 50 mm and can generate a peak thrust of 25 N, respectively. Since thrust is a function of velocity, maximum thrust is achieved at lowest velocity. Therefore, this type of stages can also withstand high acceleration and velocity movements of the robot arm without additional locking mechanisms. The carriage is prevented from slipping into end-positions by the coil hold

current.

According to the datasheet, the accuracy and repeatability are stated to be $25\ \mu\text{m}$ and $< 6\ \mu\text{m}$. It has to be considered that these values are defined by the maximum error possible, which is not a common approach by the definition of accuracy and repeatability. The achievable accuracy and repeatability are reevaluated in Section 4.6.1 by using an interferometer.

To minimize the weight of the metrology system and its impact onto the robot arm, the motor controllers (X-MCB1, Zaber Technologies Inc., Canada) are not directly integrated within the linear stage's mechanical structure and instead connected separately via motor extension cables (D-sub 15pin). They allow micro-stepping with a resolution of up to 256 in addition to the basic number of 200 motor steps per revolution.

4.1.3 Sensor system

The positioning system is equipped with a triangulation sensor (ILD1420-25, Micro-Epsilon Messtechnik GmbH & Co. KG, Germany). This sensor has a measurement range of 25 mm, a minimum laser spot size of $55\ \mu\text{m} \times 50\ \mu\text{m}$ (slight ovality) and a resolution of $0.385\ \mu\text{m}$, while the repeatability is equal to $1\ \mu\text{m}$. The measurement range is shifted by an offset of 25 mm orthogonal to the front of the housing. This design is necessary due to the physical properties of the components and the principles of triangulation. The laser has a wavelength of 670 nm (red laser light) and a laser class 2 according to DIN-EN 60825-1 [85]. In general brief exposure does not damage the human eye but preferably the triangulation sensor should only be activated if the sample position is reached. The measurement frequency can be adjusted between 250 and 4000 Hz. For a high speed scanning motion a higher measurement frequency is desired to avoid motion blur. The distance value can be read as an analogue or digital value. The analogue output signal, which results from once more converting the value from digital to analogue, is scalable by twelve bit within the measurement range. Since the utilization of the whole measurement range is desired, additional conversion and 12-bit resolution result in a loss of precision compared to the usage of the digital output. The distance value is represented as a 16-bit digitized value. Furthermore, these sensors allow simple integration into industrial Ethernet networks which are base on the EtherCAT or PROFINET technology.

4.2 Mechanical components and adapter design

Mechanical adapters are required to mount the positioning system onto the robot arm and to attach and orient the sensor appropriately as illustrated in Figure 3.4. The adapter between the robot flange and linear stage requires a solid mechanical structure to support acceleration forces and the weight of the additional components. Due to a short cable length of the linear stage's 15 pin D-Sub connector, an additional adapter for fixation is required to avoid possible damage to the components during rotations of the robot joints. To avoid additional measurement errors, an alignment of the sensor orthogonal to the

measurement plane is desired.

For the sake of rapid prototyping, lightweight design and to minimize load onto the robot arm, mechanical elements such as stage, cable and sensor adapters, are 3D printed. The used filament is polyethylenterephthalate glycol-modified (PET-G), showing a density of 1.27 g/cm^3 and Young's modulus of 2.2 GPa .

When designing mechanical elements, the possible excitation of eigenfrequencies more specifically eigenmodes within the bandwidth of the system has to be considered. In general, structural modes limit the control bandwidth of systems and lead to an error when performing high precision measurements. The evaluation of the behaviour of mechanical elements is a common task in structural analysis. Due to the fast-growing complexity of boundary value problems for partial differential equations, usually, finite-element-methods (FEM) are used.

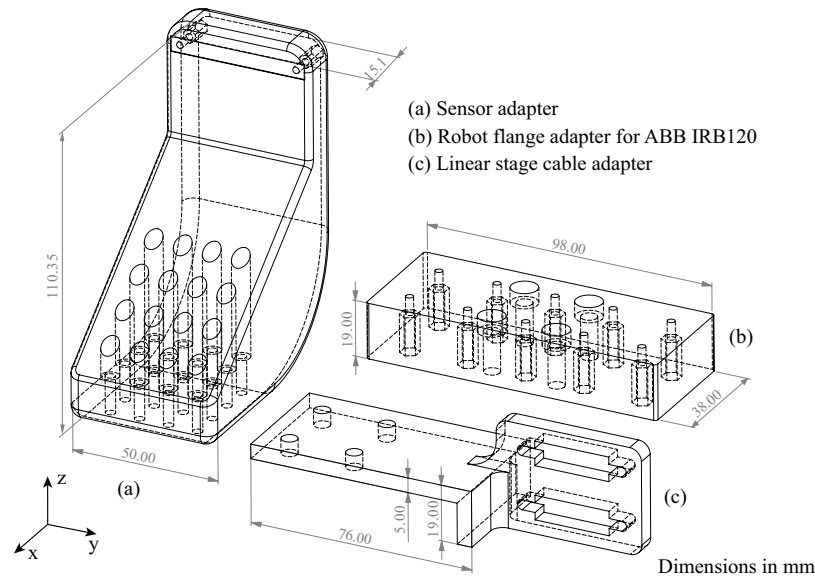


Figure 4.1: 3D printed elements of the prototype.

The specific CAD-models of the mechanical parts can be seen in Figure 4.1. The shape of the sensor adapter allows inspection of complex structures and parallel alignment of the robot flange axis and the laser of the triangulation sensor. The base plate allows montage of the linear stages onto the robot flange. In-between the cable adapter is mounted to serve as a fixation for the 15 pin D-Sub connectors. By assuming the mechanical parts to be rigid bodies, the weight of the sensor adapter is 242 g and the total mass of all 3D-printed parts is equal to 363 g . Generally, fused filament fabrication printers create a honeycomb structure, with variable in-fill factors which define the size of the comb. This reduces weight, the amount of necessary filament and increases stiffness and the overall robustness of the part depending on the in-fill ratio. In general 3D-printed elements show

a higher compressive strength and Young's modulus within the xy-plane, with the z-axis representing the extrusion direction [86]. By applying a-priori information about forces involved, the print direction can be adjusted to increase stiffness in the desired direction. The highest forces during the scan process are expected to occur in x and y direction according to the coordinate system Figure 4.1 and Figure 3.4. Therefore, the components are printed on the xy-plane with the extrusion direction along the z-axis. An infill ratio of 70 % is used, thus the actual weight of the prototype elements is lower. The mass of the sensor adapter is critical to minimize the influence of the moving mass onto the robot arm, which can result in a displacement of multiple micrometres and leads to a decrease of measurement precision. Furthermore, a lower hold current of the stages is necessary, and higher accelerations are possible.

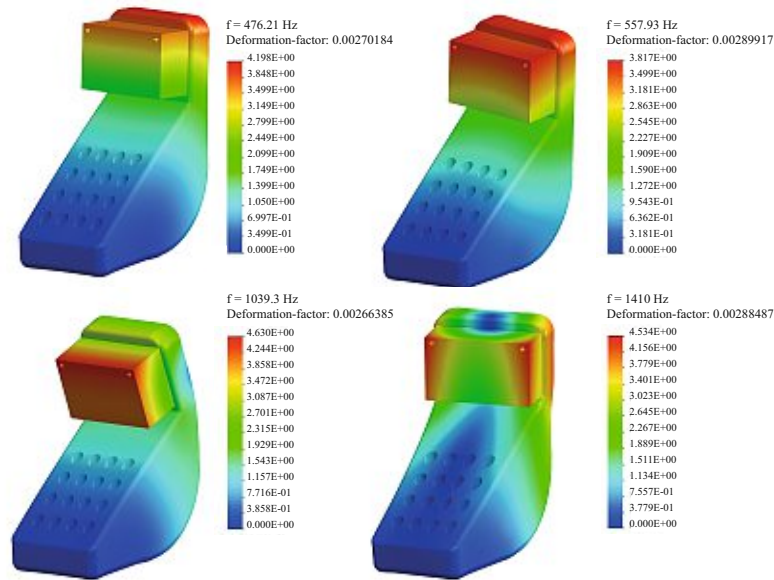


Figure 4.2: FE-analysis of the sensor adapter including the sensor.

In Figure 4.2 the first four eigenfrequencies are shown. The simulation was performed using the software SolidWorks by defining a fixation at the bottom of the adapter, representing the connection to the linear stages, and by considering the additional mass of the sensor. The structural mode shapes occur at 476 Hz, 558 Hz, 1039 Hz and 1410 Hz. Figure 4.3 shows the maximum frequency of the stage movement depending on the travel range along the stage axis for a raster trajectory with a maximum velocity of 120 mm/s and different acceleration limits. By considering constant acceleration until the desired velocity is reached. At the end of the travel range, the carriage is slowed down with the desired acceleration until the velocity reaches zero at the turning point, representing a typical raster trajectory. Due to an internal limitation of the stage controller, the acceleration setpoint is limited to 13 m/s².

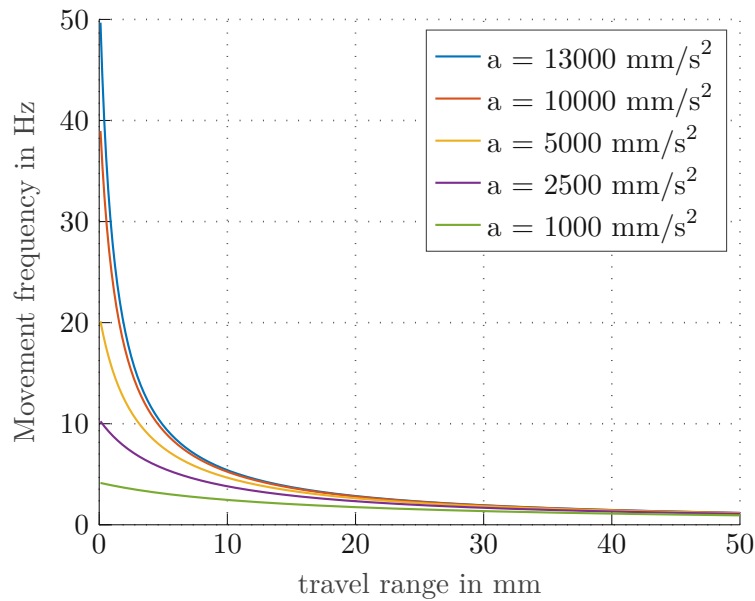


Figure 4.3: Maximum frequency of stage movement when performing a raster trajectory, depending on the range of motion.

As mentioned in Section 2.3 the spectrum of raster trajectories, resulting from a triangular actuation signal, contains all odd harmonics of the base frequency. According to [87] at least the first seven harmonics have to lie within the system bandwidth. For a maximum frequency of 50 Hz and a frequency of 476 Hz of the first structural mode shape, the first nine harmonics are covered by the system bandwidth. This leads to the conclusion that the designed adapter is suitable for the scanning process. Even though the linear stages are limited in their movement frequency, depending on the range of motion, maximum speed and acceleration the analysis of the dynamics is of great importance to identify possible error sources which reduce the overall precision.

By using SolidWorks, the impact of a sinusoidal trajectory with an amplitude $A = 0.5$ mm in a frequency range from $f = 0$ to 50 Hz is analysed. The results are displayed in Figure 4.4 and show that a displacement due to temporal elongation and compression of the material occurs. Figure 4.4.a represents maximum values which occur at top side of the sensor, while Figure 4.4.b shows the maximum deformation of the adapter. The required acceleration a for a specific frequency of a sinusoidal movement is defined by $a = A(2\pi f)^2$. As mentioned previously the maximum acceleration of the controller is limited to 13 m/s. Therefore, for a range of motion of 1 mm the maximum frequency is equal to 25.7 Hz which results in a maximum displacement of the sensor endpoint of $3.93 \mu\text{m}$ according to the simulation. This value can also be taken into account for raster trajectories due to the identical limitation of maximum acceleration. For a spot diameter of the triangulation sensor of 55 x 50 mm this error is considered small.

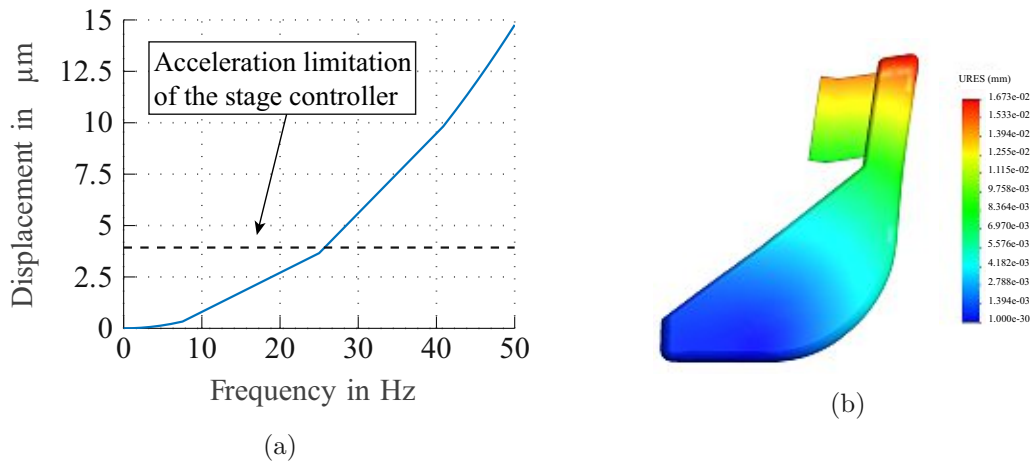


Figure 4.4: Adapter deformation due to accelerations of trajectories.

4.3 Intelligent scan and measurement process

As discussed in Section 3.5 fluctuations in production lines of the position or orientation of a sample or its feature, or deviations between a CAD-model and the actual product can affect the result of the inspection task. A precise "teach-in" procedure for industrial robots can consume a significant amount of time, and costs [88], especially for production lines with varying batches (e.g. products of different geometry). Instead of performing a basic robotic movement to a fixed position, followed by a scan over an area with defined dimensions, an intelligent scan and measurement process is desired to improve the quality of measurement data and provide additional flexibility for production lines. This leads to the following concept of an intelligent process.

By considering the inspection of welds, the robotic metrology system can be roughly aligned either by an operator or by utilizing CAD data. The only prerequisite is that the weld spot is located within the measurement volume of $50.8 \times 50.8 \times 25$ mm. By utilizing suitable trajectories which provide a fast overview of the scan area, as discussed in Section 2.3, in combination with feature detection algorithms according to Section 2.6, the feature (e.g. weld spot) can be identified within the measurement volume. This leads to a refined scan area. Optical sensor systems typically show a dominant focus point with minimum spot-size as seen in Figure 4.5 according to the specifications of the triangulation sensor. A realignment of the robotic arm follows the detection step to achieve optimal distance of 31 mm to the sample, according to Figure 4.5, and parallel alignment of measurement and sample plane. After the repositioning process, the refined scan area is scanned with an adjusted trajectory and scan parameters.

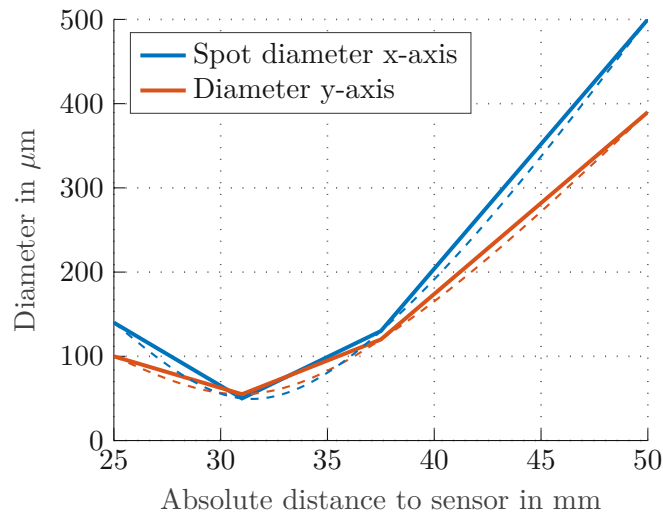


Figure 4.5: Spot diameter of the triangulation sensor (ILD1420) over absolute sensor distance (effective range 25 – 50 mm, points according to datasheet (continuous line), interpolation (dashed line)).

4.3.1 Scan trajectory selection

As already mentioned, Lissajous trajectories provide a fast overview of the scan area and are therefore suitable for locating features. Depending on the feature's expected size, by using a-priori information, the trajectory requires at least a resolution that undercuts the largest geometrical dimension of the feature to be able to locate it. This requires a suitable metric and selection of the driving frequencies.

To quantify the resolution of Lissajous trajectories different metrics can be used, e.g. the maximum distance between the intersection points of scan lines in x and y direction. A robust metric which utilizes Voronoi tessellation was already applied for Lissajous Trajectories by [39]. Since this metric is used for the following discussion, a short introduction is given.

Voronoi tessellation is based on the partitioning of a space into a set of Voronoi cells, more specifically -polygons $C(i)$. In this case, a cell is assigned to every data point $P(i)$ along the trajectory defined by an xy-position in space. Therefore the number of data points respectively cells $i = 1, 2, \dots, N$ depends on the sample rate (e.g. the acquisition speed of a sensor or a data acquisition card), size of the scan area and scan duration. A cell is defined as a subregion in which all data points are closer to the data point, assigned to the cell, than to any other point. By applying this procedure, every cell is afterwards represented by a complex polygon. The centroid, area size and radius from the centroid to the vertex, farthest from the centre, can be calculated and provide useful metrics.

In Figure 4.6 the calculated Voronoi cells for Figure 2.2b ($f_x = 10$ Hz and $f_y = 12$ Hz)

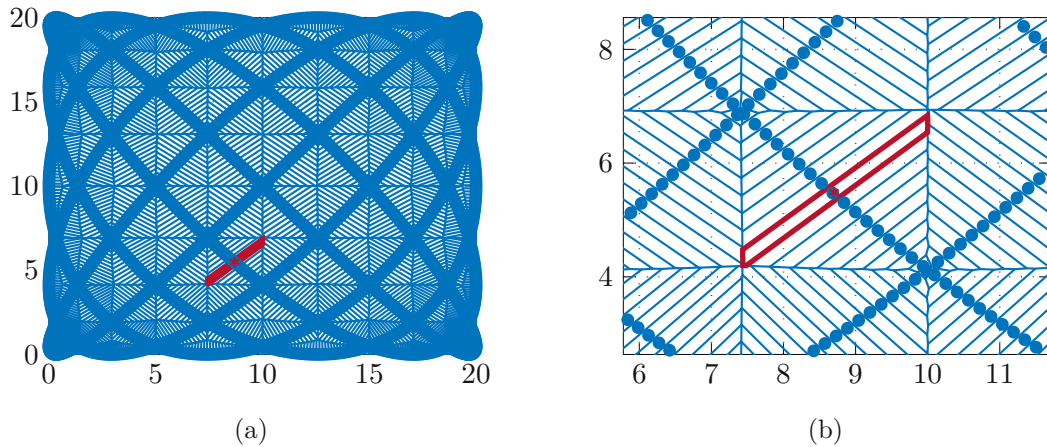


Figure 4.6: Resolution of a Lissajous trajectory, (a) Voronoi tessellation for $f_x = 10$ Hz and $f_y = 12$ Hz, $T = 0.5$ s, Sample rate $f_s = 4000$ Hz (see also Figure 2.2b), (b) close-up of the largest cell.

and a close-up of the largest cell for the maximum sample rate $f_s = 4000$ Hz of the triangulation sensor can be seen. The maximum radius is equal to 1.874 mm for an area of 20x20 mm ($X_{pp} = 20$ mm, $Y_{pp} = 20$ mm according to equation (2.2) and (2.3)). By representing the radius of the largest cell this value is equal to the lowest resolution within the scan.

By assuming a square scan area, linear scaling of both, X_{pp} and Y_{pp} leads to a linear change in resolution. Therefore by adjusting the size to 10x10 mm in the previous example, the resolution is doubled from 1.874 mm to 0.9369 mm. This property can be considered when a dynamic adjustment of the scan area, is necessary to avoid extensive computing of suitable frequencies. It can be applied if a coarse Lissajous scan to locate an object should be followed by a fine Lissajous scan and as long as the proportional increase of resolution fulfils the required resolution of the fine scan. For example, a feature with an area of 2x2 mm should be located in an area of 20x20 mm and scanned with a lateral resolution of at least 200 μ m. A coarse scan resolution of 1.874 mm leads to a fine scan resolution of 187.4 μ m for a resulting amplitude reduction of X_{pp} and Y_{pp} by a factor of 10 and satisfies the requirement. If a higher resolution is desired, a different frequency combination has to be found.

Figure 4.7 shows the resolution of a Lissajous scan for an amplitude of 1 mm (2x2 mm) scan area depending on the duration. As discussed in Section 4.2, due to a limited stage velocity, the maximum frequency is a function of the range of motion. To achieve maximum resolution and minimize duration, the frequency of one axis is assumed to be close to the maximum possible value. This also reduces the selection process to one dimension. In this case a maximum frequency of stage one $f_x = 38$ Hz is selected while f_y is varied from $f_y = 0.1$ to 37.9 Hz. Due to the properties of the least-common-multiple, various frequencies lead to an identical duration. Therefore, also lower frequencies, which lead to

less excitation of the mechanical structure, can be selected. e. g. for a duration of $T = 1$ s, frequencies starting from 1 to 37 Hz in 2 Hz-steps are suitable. A minimum resolution of $42.9 \mu\text{m}$ is reached for $f_y = 31$ Hz. The worst resolution for $T = 1$ s is $55.1 \mu\text{m}$ for $f_y = 5$ Hz. Lateral resolutions in this range are already suitable for the used triangulation sensor, due to its minimum spot size, as it will be shown in later chapters. To achieve an equal resolution for double the amplitude $A = 2$ mm (scan area: 4×4 mm, area increase by a factor of 4) a minimum time of 5 seconds is necessary, also due to the fact that the possible frequency range decreases. This increase in time is more significant for lower ranges of motion due to an inverse proportional decrease of the maximum frequency over the travel range.

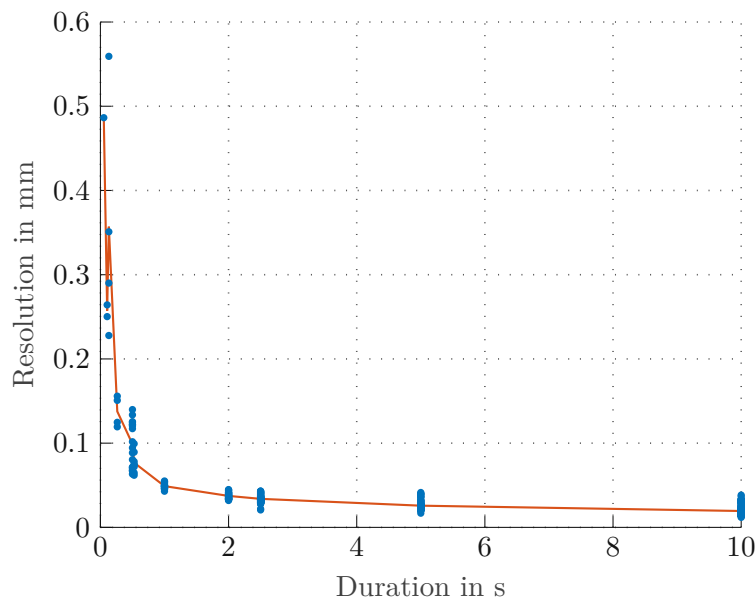


Figure 4.7: Resolution of a Lissajous scan depending on scan duration for an amplitude $A = 1$ mm (scan area: 2×2 mm).

Following the guidelines of this chapter, Figure 4.8 extends Figure 4.7 by the amplitude as third dimension, under the assumption of a square scan area. This data serves as a look-up table for the measurement process to find a frequency combination that leads to the desired resolution in minimal time for a certain scan area. This reduces computational effort between scans.

4.3.2 Feature detection

The goal is to use a robust algorithm to be able to detect the features of interest and to meet the following requirements:

- The object should be detected by performing a coarse scan of an area where the object is to be expected.

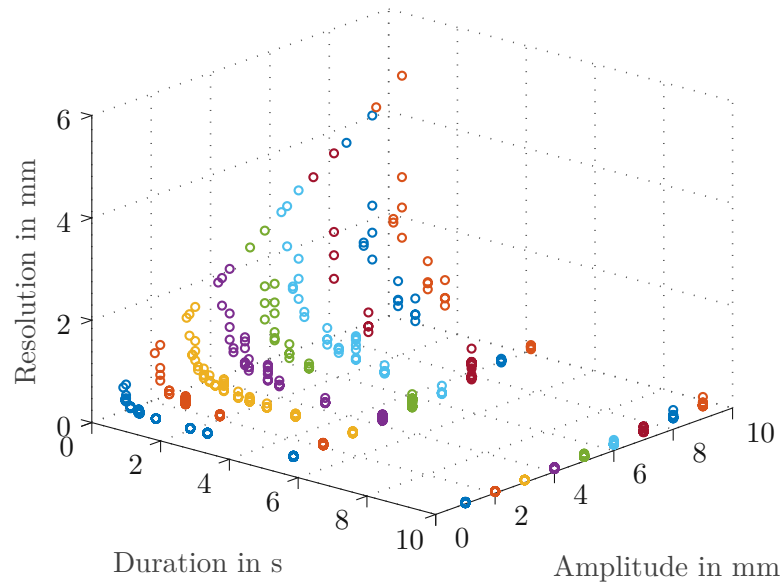


Figure 4.8: Resolution of Lissajous scan depending on amplitude and scan duration.

- The detection process has been finished within the duration T of the Lissajous trajectory (cf. (2.4)) and the coarse scan should be preferably interrupted as soon as the object is detected.
- Soft-realtime is demanded. Therefore the algorithm is called repeatedly during the scan while new data is added, and the expected object data is refined. When the coarse scan is finished the fine scan should start without a noticeable delay. To keep the overall process time as short as possible.

A simple, computationally cheap and efficient way is to implement a basic edge-detection algorithm. Edges can be defined as a location of a rapid intensity variation. Mathematically, the intensity variation can be defined through the magnitude and orientation of the image gradient. Calculating the derivative of images leads to an accentuation of high-frequency components and hence amplification of noise. Therefore, a smoothing of the image before the differentiation is recommended. One of the most prominent representatives based on this procedure is the Canny edge detector [62]. Over time various edge detection algorithms have been developed [89] [90].

During the prototype creation, a form of a Canny edge detector is implemented to allow the detection of the sample during a coarse pre-scan. This algorithm is discussed briefly. In the first step, the image is smoothed by applying a gauss-filter to remove noise and reduce the impact of outliers. The strength of the filter is defined by the standard deviation σ of the Gaussian distribution. The window size is selected depending on the standard deviation. A higher standard deviation leads to a bigger window which results in stronger smoothing and noise suppression.

Afterwards, the Sobel operator, which is a typical filter used image processing, is applied by convoluting the image and the filter to calculate the derivative for both, x and y direction. The Sobel operator is defined by the following matrices (4.1) and (4.2):

$$G_x = \begin{bmatrix} -1 & 0 & 1 \\ -2 & 0 & 2 \\ -1 & 0 & 1 \end{bmatrix} \quad (4.1)$$

$$G_y = \begin{bmatrix} -1 & -2 & -1 \\ 0 & 0 & 0 \\ 1 & 2 & 1 \end{bmatrix} \quad (4.2)$$

Additional information about the scan area or object can be taken into account to increase the robustness of the algorithm. For example, filter parameters can be adjusted when coarse surfaces are scanned to prevent areas of high-intensity change from being classified as an edge. By using approximate data of object or feature size, thresholding can be performed to suppress outliers. Furthermore, multiple features can be detected by performing clustering on condition that dimensions of targets are known, e.g. the diameter of a spot weld.

The result of the implementation, in combination with the robotic scan system, can be seen Figure 4.10. An area of a 3D-printed reference sample is scanned. The sample area contains four rectangular indentations with a width from 500 down to 200 μm , a constant length of 5 mm and a depth of 200 μm . The sample was created by a high-resolution 3D-printer based on the stereolithography (SLA) technology (cf. Chapter 5). As already mentioned, the edge detection algorithm is called continuously during the scan process. A Lissajous trajectory with a duration of 10s was selected. As discussed in Section 2.3 the duration and frequencies determine the resolution of a Lissajousscan, while the achievable frequency depends on the range of motion. The figure shows the development of the scan result over time, sections which are characterized as edge are marked with black dots. As discussed Lissajous scans already provide an overview of the scan area within a small proportion of the duration. In this case, after approximately one-fifth to one-third of the scan duration, all indentations are included in the refined area marked by the red square. The last two subfigures show the result after full duration. Compared to Lissajous trajectories, a raster scan shows an overall slower convergence of the algorithm. If a features is located at the opposing end of the scan area a raster scan can require up to the full scan duration as illustrated in Figure 4.9.

Also, the smallest two indentations are detected, and parts of them are characterized as an edge. Nevertheless, it can be seen that the depth is not measured correctly, which is due to the following reason. The triangulation sensor, respectively robot arm is not positioned in the optimal distance, which leads to a deterioration of the lateral resolution due to the characteristics of the triangulation sensor. This issue can be overcome by repositioning the robot after the coarse scan is done or rather an abort criterion for the feature detection is full-filled. The data of the coarse scan can be used to compensate for

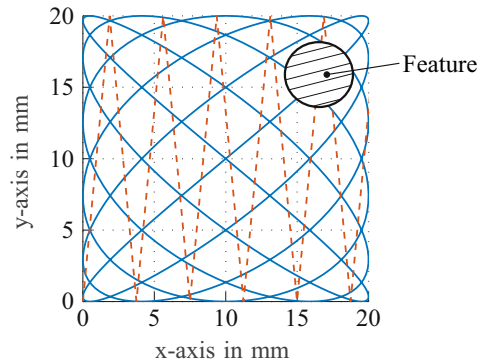


Figure 4.9: Raster and Lissajous scan for the detection of features.

the translation and orientation of the robot arm with respect to the sample. This will be shown in detail in Section 5.4.

Figure 4.11 shows the scan data of a spot weld and its surrounding area. The area is scanned by using a coarse scan. The red square marks the area in which the features are detected and used for a high-resolution scan. After the fine scan, both datasets are combined which leads to Figure 4.11b. Figure 4.11c and Figure 4.11d show a perspective view of the xy - and xz - plane. The resulting data can also be used to characterize the diameter of the weld spot and the indentation depth, which serves as a quality measure. This weld spot shows a diameter of approximately 4.45 mm and a maximum indentation of 194 μm . According to DIN EN ISO 18595 [91], the indentation depth must not exceed 20% of the thickness of one sheet metal. For a sheet thickness of the sample of 1 mm this weld spot fulfils the criteria. The elevation next to the welding spot results from residuals of the welding process. Furthermore, the weld spot does not show surface cracks or porosity. Therefore, this weld is considered of good quality, which has been confirmed by the supplier of the sample.

In conclusion the implemented edge detector allows fast detection of feature points during a coarse scan process which can be stopped when desired criteria are fulfilled. This can be used when specific features on a more massive object should be identified, whose high-resolution scan is of interest or if the exact position and orientation of a sample is unknown. Furthermore, this allows compensation for CAD-model or in-line tolerances. The parameters have to be adjusted depending on the sample to achieve equal sensitivity for different structures or surfaces. Filter and threshold parameters have to be adjusted depending on the sample. The obtained data allows refining of the scan area and repositioning of the robot to achieve maximum resolution for a fine scan. Elementary structures such as circular objects, e.g. weld spots can be characterized within a small proportion of the total scan duration due to the properties of a Lissajous scan. By using a-priori information of the expected diameter, only a few feature points are sufficient.

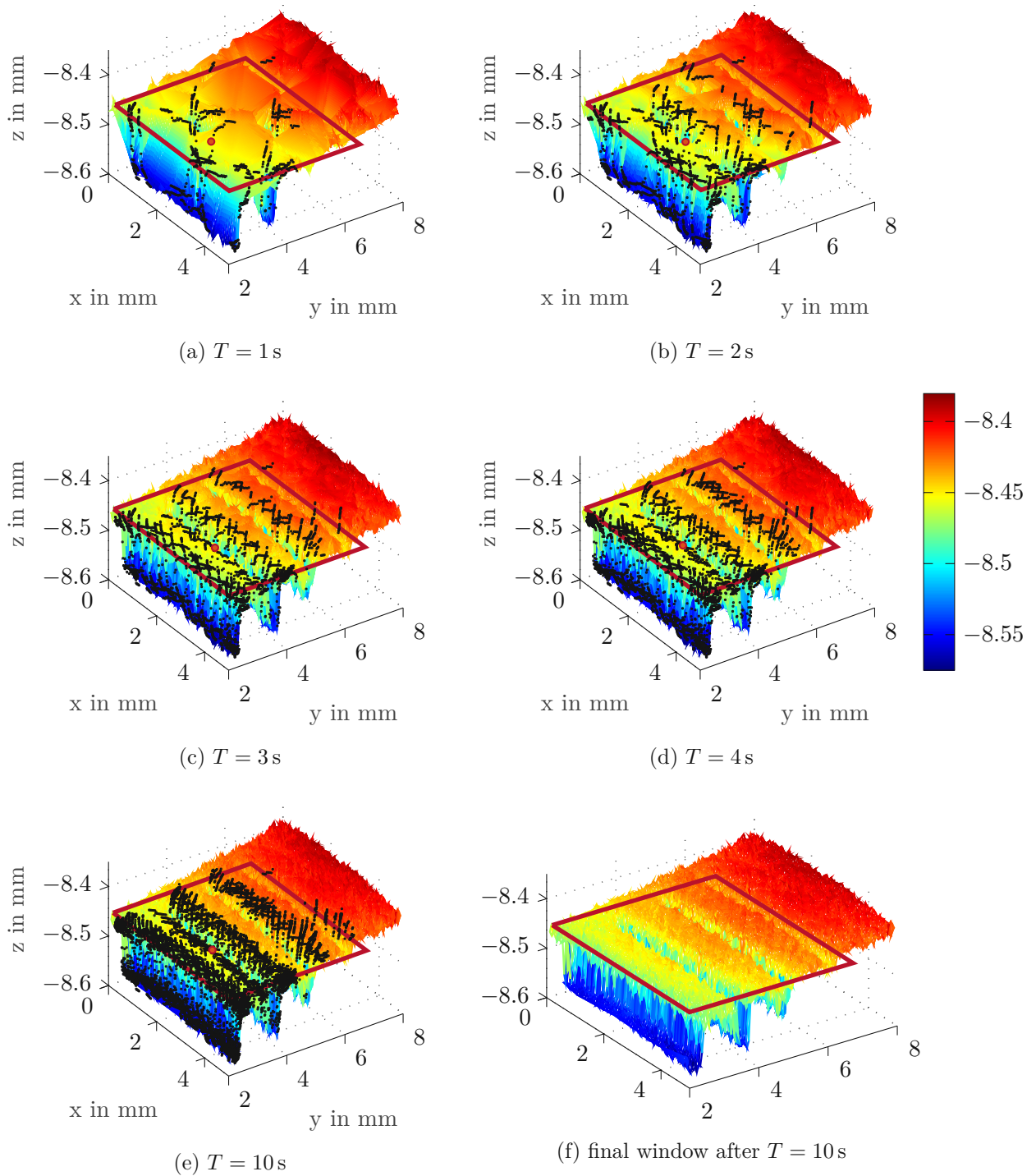


Figure 4.10: Scan area and detected edges (marked by black dots) for different scan durations (a-e) and scan result after $T = 10$ s (f).

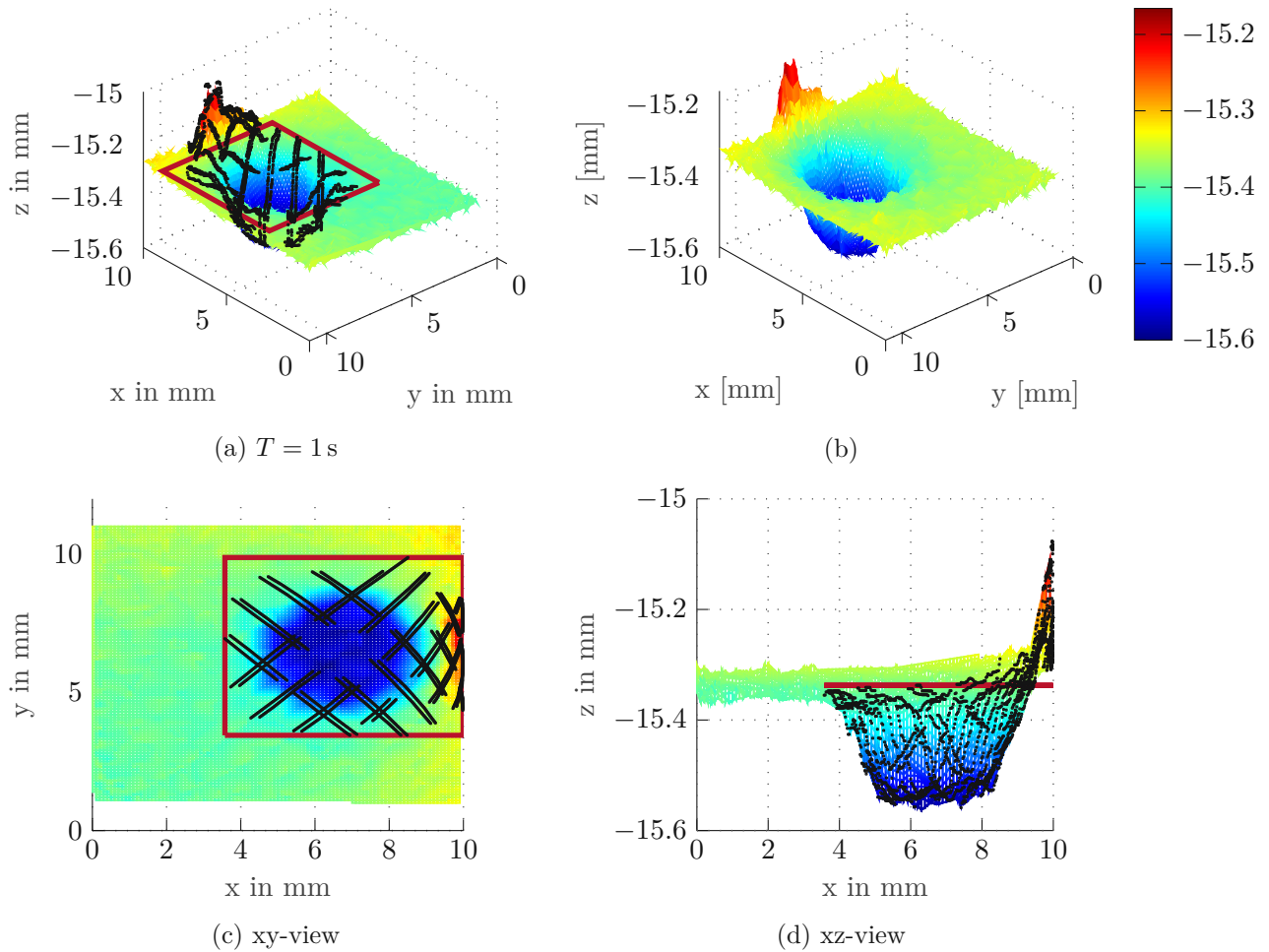


Figure 4.11: Scan data and detected edges (marked by black dots) of a weld spot and its surrounding area, final data with and without edges (a-b), perspective view (c-d).

4.4 Communication concept and sequence control

4.4.1 Communication concept

To enable real-time information- and data exchange between system components, modules of Beckhoff Automation were selected. These modules provide a cost-efficient, modular setup based on the EtherCAT technology. The system can be integrated into an existing industrial network via, in control cabinets mounted industrial computers or via EtherCAT-couplers. Depending on the field of application, the system can be connected to different Fieldbus or Industrial Ethernet technologies like CANopen, DeviceNet, PROFIBUS,

PROFINET IRT via a master/slave terminal.

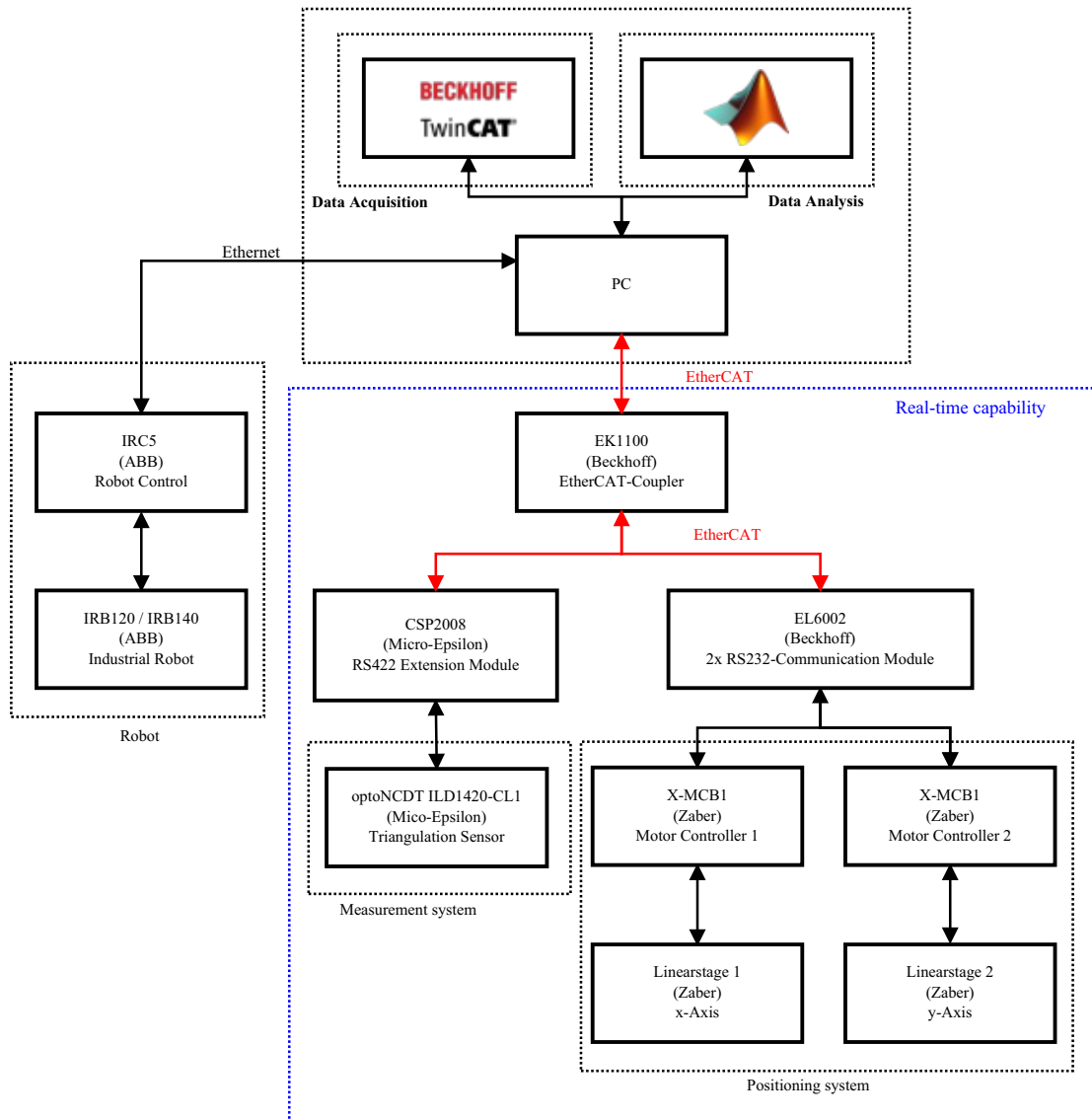


Figure 4.12: Communication structure of the prototype.

In Figure 4.12 the communication structure of the prototype is shown. The system is mainly split into items, respectively tasks, which demand real-time capability and those, whose completion allows more flexibility regarding their time-frame. The data acquisition is implemented by utilizing the Software TwinCAT by Beckhoff Automation which allows real-time communication with corresponding modules in combination with an Intel-chipset network card and an EtherCAT-coupler. Furthermore, the software provides isolation of CPU cores from other tasks. TwinCAT is based on cyclic execution of tasks in terms

of a Soft-PLC, if not integrated on an industrial PC, with a minimum cycle time of $50 \mu\text{s}$. Nevertheless, subsampling for analogue modules down to $5 \mu\text{s}$ is possible if desired. As mentioned in the previous section, the triangulation sensor allows integration into EtherCAT networks via an RS422 module and allows cyclic data read-out and parameter adjustment. Since a continuous scan motion is desired, the current position of the stage's carriage has to be read out within a fixed time frame to allow synchronization with the sensor data. RS232-interfaces are used to communicate between corresponding modules and the motor controllers. In general, the limiting factor of serial interfaces regarding communication speed is the baud rate. The baud rate of an RS232-interface is equal the bitrate. Furthermore, each symbol, e. g. ASCII-symbol, consists of 8-bit and additional start-, stop- and parity bits depending on the configuration. The selected linear stages provide an ASCII and a binary protocol with a varying and a fixed number of symbols per message, respectively. The usage of the binary protocols provides faster communication due to a specified message length of 6 Byte but shows limited flexibility due to missing commands provided by the ASCII protocol. In this specific case, position readout rate can be increased by a factor of approximately eight from 142 Hz to 1142 Hz, this includes the request and receiving of position data.

To interface Matlab, which is used to perform data analysis, TwinCAT provides the ADS (Automation Device Specification) - Interface. The ADS describes a device- and Fieldbus-independent interface to access ADS devices, e. g. TwinCAT system, TwinCAT PLC and Windows programs. Data exchange with Matlab can not be performed in hard real-time, but the task of data analysis does not require this functionality. Although, Matlab is used to detect features during an initial coarse scan with continuous data exchange between TwinCAT and Matlab, e.g. pose requests, movement commands.

As already mentioned ABB supplies robots with a uniform controller which offers various interfacing options. To access and manipulate the robot pose a script based on TCP/IP socket communication was integrated on the controller by using the specific program language for ABB robots, Rapid. This socket allows communication between Matlab and the IRC5 controller.

4.4.2 Sequence control

Figure 4.13 shows the primary sequence control of the complete scan process, which is split into a fine scan and, if necessary, a coarse scan in prior to the main scan. The coarse scan utilizes the properties of Lissajous trajectories, as discussed in Chapter 4.3, to obtain a fast overview of the scan area. The resulting data is used to detect features or the object position and orientation, which is executed parallel to the coarse scan process. Therefore, the coarse scan can be interrupted if a stopping criterion is fulfilled. The stopping criterion can be defined by applying a-priori information about the feature size. If the refined area reaches a size within a certain threshold the coarse scan is finished. Next to the feature detection, the orientation and position are calculated by using RANSAC or least-squares algorithms, to reposition the robot parallel to the surface and in the optimal distance for the optical sensor system. After reorienting the robot, a scan with the desired resolution

is performed on the area, defined by the feature detection result, and the final data is evaluated.

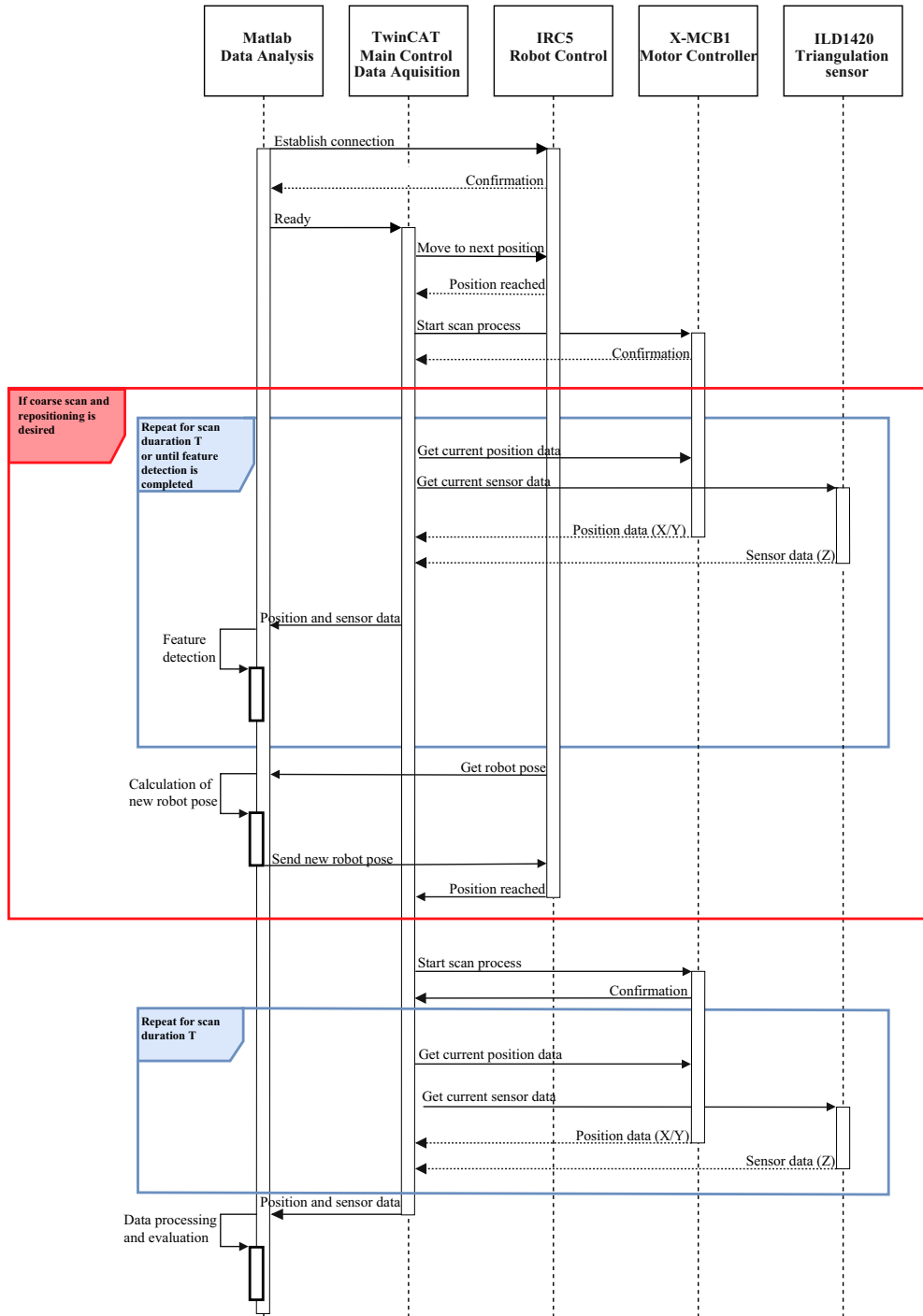


Figure 4.13: Sequence control of the measurement process for a single measurement location.

4.5 Experimental setup overview

This section gives a brief summary of the main specifications of components used for the prototype setup, which is also shown in Figure 4.14. In the following sections, these specifications according to the data sheets, are evaluated based on the requirements of the robot-based in-line measurement system.

Component	Specification	Value
Robot arm	Pose accuracy	0.02 mm
	Pose repeatability	0.01 mm
	Maximum range	580 mm
	Load capacity	3 kg
Linear stage	Travel range	50.8 mm
	Accuracy	25 μm
	Repeatability	6 μm
	Maximum velocity	120 mm/s
	Maximum force	25 N
Triangulation sensor	Measurement range	25 mm
	Resolution	0.385 μm
	Repeatability	1 μm
	Minimum spot size	55 x 50 μm
All components, including 3D-printed parts	Weight	983 g
Software environment (TwinCAT)	Minimum cycle time	50 μs

Table 4.1: Main specifications of prototype components.

4.6 Component performance verification

4.6.1 Linear stage performance verification

As a first step, the static and dynamic behaviour of the linear stages which serve as the xy-scan system is analysed by using an interferometer (IDS3010, Attocube Systems AG, Germany). The interferometer has a sensor resolution of 1 pm, repeatability of 2 nm and a measurement bandwidth of 10 MHz, according to the datasheet. It utilizes a laser

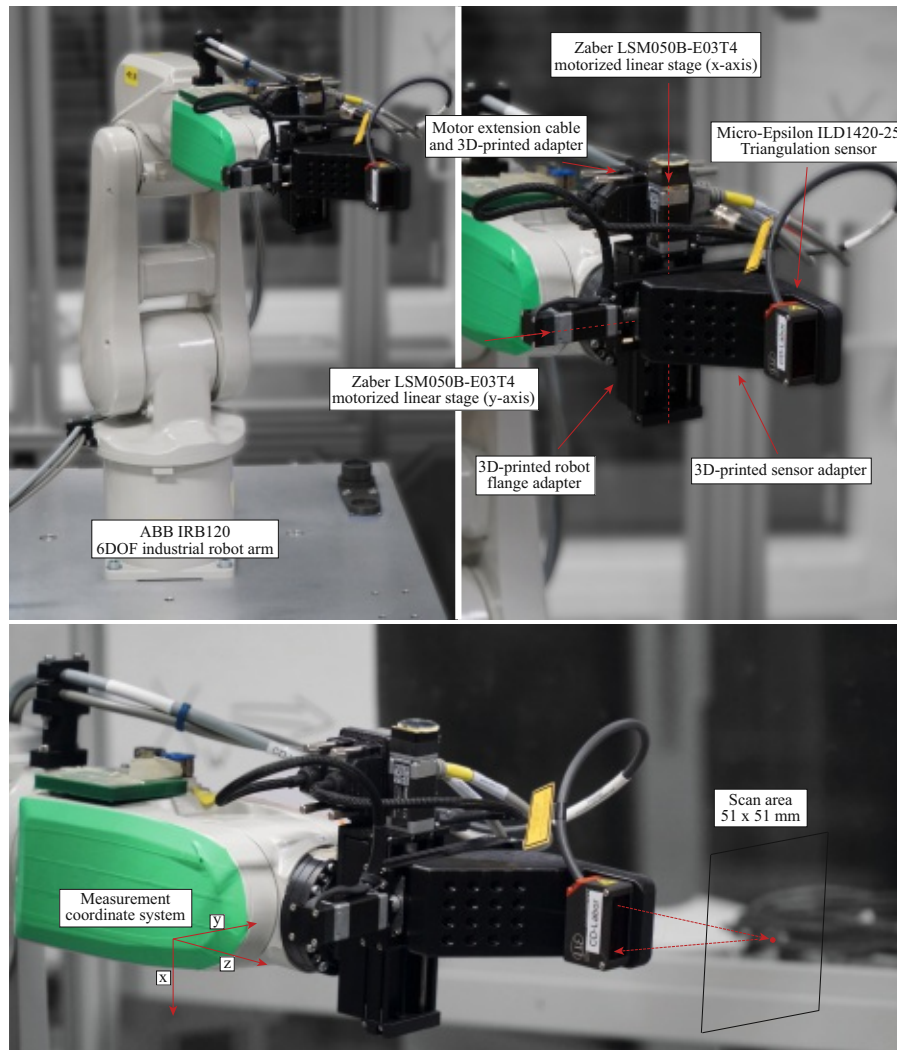


Figure 4.14: Prototype setup overview.

source with a wavelength of 1530 nm. The working distance depends on the selection of the sensor head. A compatible fixed focus fibre collimator (F240FC-1550, Thorlabs GmbH, Germany) is used. The collimator is designed for an alignment wavelength of 1550 nm, a beam divergence angle of 0.073° and a waist diameter of 1.6 mm. But it is also designed to show a low sensitivity of the laser beam divergence to the wavelength of the used source of approximately $0.75 \cdot 10^{-3} \text{ }^\circ/\text{nm}$. Therefore, this collimator can be used in combination with the interferometer, which leads to a divergence angle of 0.0745° . The Rayleigh distance is approximately 5.19 m which is more than sufficient for the desired measurement range of 50.8 mm [92]. The waist distance, which is measured from the front of the collimator housing is equal to 7.26 mm.

The experimental setup is presented in Figure 4.15 all mechanical components are mounted

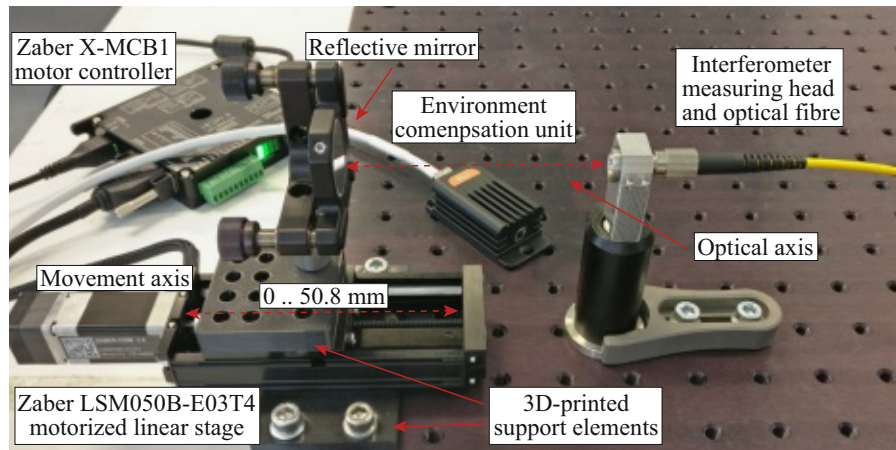


Figure 4.15: Measurement setup for the validation of the linear stage performance.

on an anodized aluminium plate for optical applications with additional rubber bumpers to reduce the impact of ground vibrations. 3D-printed support elements are used to mount a reflective mirror on the stage's carriage and the stage itself on the breadboard. The fixed focus fibre collimator is mounted in a distance of approximately 30 mm to the mirror. This distance is chosen to ease the alignment process, prevent a loss of beam intensity over large distances and perform measurements with planar wavefronts within the Rayleigh distance. The setup is aligned by minimizing the Abbe error, which is the case when the optical axis and movement axis are exactly parallel. The interferometer has an additional environment compensation unit to improve measurement precision.

In the beginning, the behaviour of the interferometer is investigated to specify the quality of the measurement. Errors may occur to temperature fluctuations in the laboratory environment, and thermal drift of the internal components of the interferometer has to be considered. In addition, ground vibrations can lead to an increase in the noise level due to the sensitive measurement process. In Figure 4.16 the measured displacement value is shown relative to a stationary object over a time of three hours after turning on the interferometer. In the first hour, a strong thermal drift by $2\ \mu\text{m}$ is visible which is followed by a decay to a more stable signal. For the following measurements of the static and dynamic behaviour, a maximum measurement window of 400 s is used before adjusting the reference value to the current displacement value, to minimize the influence of drifts. To evaluate the precision and the drift within the measurement window the standard deviation of the displacement data, within a moving window is calculated. The result is shown in Figure 4.17. Therefore, after waiting for the temperature drift to decay, the measurement values are distributed with a standard deviation between 6 and 30 nm and an average STD of 15 nm. This leads to a precision of three times the standard deviation of 45 nm within the measurement window under the assumption of a normal distributed measurement quantity. Due to the specifications of the linear stages, this serves as a more than sufficient precision for characterization.

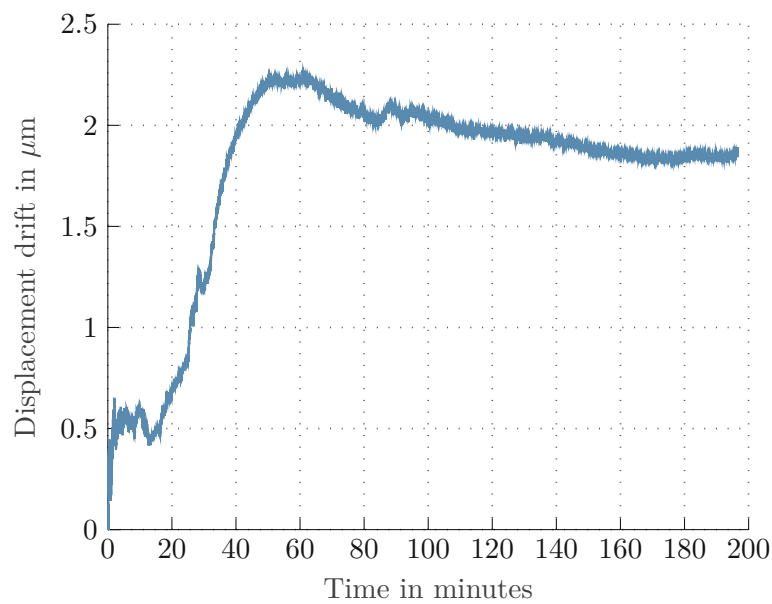


Figure 4.16: Drift of the measured displacement by the interferometer over time.

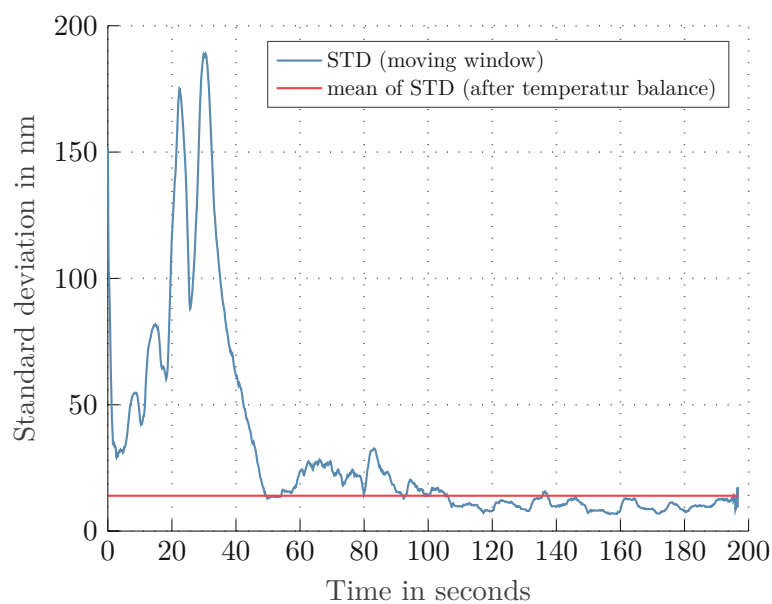


Figure 4.17: Standard deviation (STD) of the displacement drift within a moving window.

Static analysis

For various positioning systems, e. g. robots, linear actuators or rotary tables, the ability to achieve high repeatability in repetitive tasks is of great importance. In this section, the static accuracy and repeatability of the stepper motor based linear stages when performing point-to-point movements are investigated. This is done for both directions of movement, either by starting from $x_1 = 0$ mm (initial position) or $x_2 = 50.8$ mm (maximum position). The carriage of the stage is controlled to move from x_{start} to each position \hat{x} within the range of motion in 1 mm steps one-hundred times and back to the starting point. Before and after one-hundred repetitions the stage is homed to receive a reference position and achieve same prerequisites for all positions \hat{x} . This justifies the choice of the considered measurement window for the analysis of the interferometer behaviour as discussed in Section 4.6.1, thus within 100 repetitions, the precision of the measurement is approximately 45 nm. This measurement process is described in detail in Table 4.2. The measurement is performed with maximum stage velocity of 120 mm/s and an acceleration of 4000 mm/s. Velocity and acceleration set point are handed over to the Zaber X-MCB1 motor controller.

The data is acquired by using a Matlab interface provided by Attocube Systems AG via TCP/IP connection. This interface does not offer real-time communication but is suitable for static analysis. For dynamic analysis synchronization of displacement data, provided by the interferometer, and timestamps are necessary. Therefore, the interferometer's real-time output in combination with modules by Beckhoff Automation is used. This will be discussed in Section 4.6.1.

Initialisation	Set $x_{start} = x_1$, $\hat{x} = 1$ mm, reference stage, use currently measured displacement as reference and go to step 1
Step 1	If $\hat{x} > 50$ mm and $x_{start} = x_2$ go to END. If $\hat{x} > 50$ mm set $\hat{x} = 0$ mm, $x_{start} = x_2$ and go to step 2
Step 2	Move from x_{start} to \hat{x} , measure displacement and return to x_{start} . Repeat Step 2 one-hundred times and go to step 3
Step 3	Increase \hat{x} by 1 mm, reference stage and use currently measured displacement as reference for next 100 repetitions and go to step 1
END	Measurement for both directions of movement is finished.

Table 4.2: Measurement process of static analysis.

In Figure 4.18 and Figure 4.19 the results for both directions of movement are shown. In the first figure, the movement is performed between x_1 and desired position \hat{x} , while in the second figure, the carriage moves between the maximum point x_2 and desired point \hat{x} . The error is defined by the difference between target and actual position. The blue line shows the average error of a hundred repetitions each and the standard deviation, respectively. The average error for both tasks is in the range of submicrometre (0.428 μm and 0.282 μm), with the maximum error exceeding 5 μm as a worst-case. The

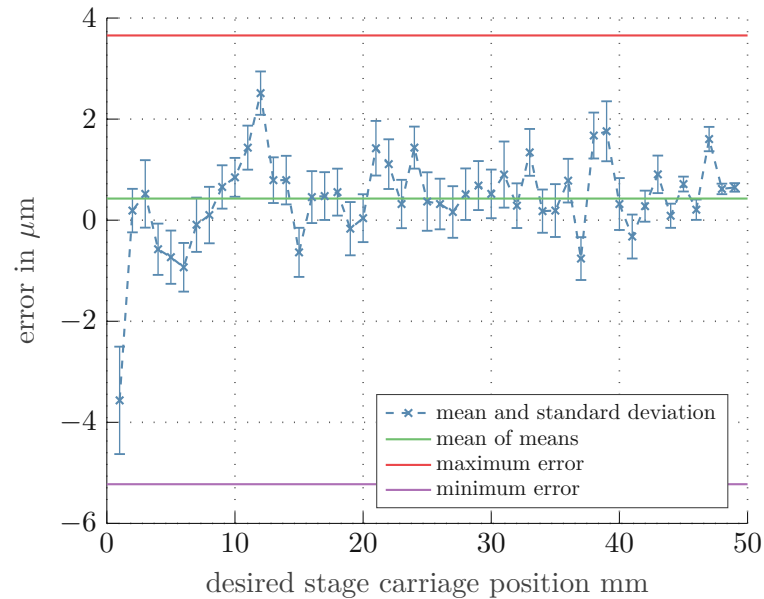


Figure 4.18: Position repeatability of the linear stages depending on the desired carriage position.

average standard deviation σ is equal to $\sigma_1 = 0.4566 \mu\text{m}$ and $\sigma_2 = 0.4583 \mu\text{m}$. Therefore σ only shows a difference of 1.7 nm and serves as a good characterization for the repeatability of the stages and supports the measurement approach. Under the repeated assumption of a normal distributed behaviour of the error variable, the absolute accuracy is equal to $0.355 \mu\text{m}$, as an result of the mean of both average errors, and the repeatability is equal to $1.372 \mu\text{m}$ ($3/2(\sigma_1 + \sigma_2)$). The maximum error in repeatability is $3.203 \mu\text{m}$.

Accuracy and repeatability according to the manufacturer are defined by the maximum possible error (cf. Section 4.5) as $25 \mu\text{m}$ and $< 6 \mu\text{m}$. The measured data shows that the maximum error is lower by a factor of approximately 5 and 2, respectively. Overall they fulfil the specifications according to the datasheet and even perform better. In general, the stages tend to surpass the target position rather than stop below but are suitable for tasks where an average accuracy and repeatability of single-digit micrometres is desired. This also leads to the conclusion that they are a suitable choice for optical surface inspection when single-point measurements are desired. Nevertheless, short throughput times are a critical factor in production lines, requiring a continuous movement to minimize scan time. This requires the analysis of the dynamic behaviour.

Dynamic analysis

After analysing the static behaviour, the dynamic behaviour during phases of constant acceleration and velocity, is evaluated in this chapter. This analysis is of particular interest when a continuous scanning motion is desired. Being aware of the behaviour and the error

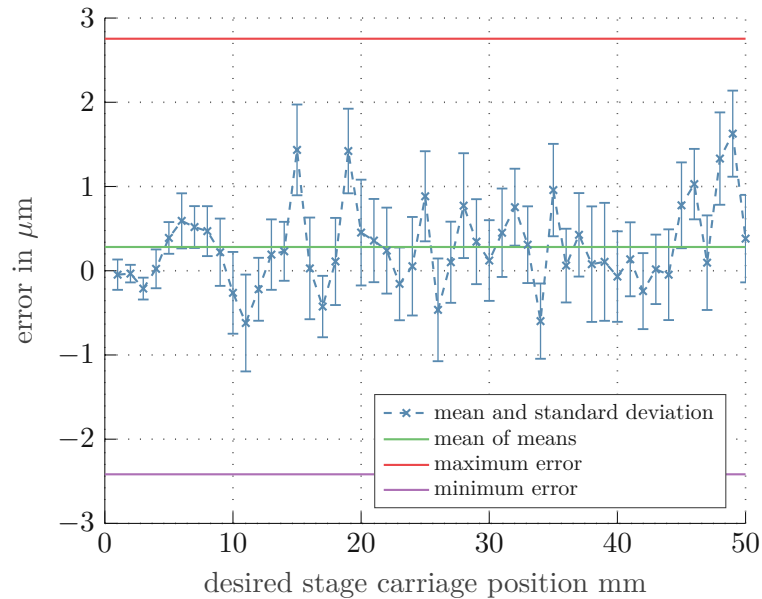


Figure 4.19: Position repeatability of the linear stages in the opposite direction depending on the desired carriage position.

fluctuation during phases of constant velocity is of great importance due to the limited baud rate of the linear stage's communication interfaces and the feasible measurement frequency of the triangulation sensor exceeding the position update rate by a factor of 4 to 32 when using binary or ASCII protocol, as discussed in Section 4.4.1. Therefore, assumptions about the behaviour between position samples can be made, and appropriate interpolation methods can be used. The measurement setup is ident to Section 4.6.1. With the exception of using the real-time output of the interferometer to capture the movement and the dynamic behaviour precisely.

The IDS3010 interferometer provides different output modes (High-Speed-Serial-Link-mode (HSSL) and AquadB-mode represented as LVTT-signal or Sine-Cosine-mode represented as an analogue signal) [93]. AquadB-mode is an incremental protocol that only transfers change of the displacement. Sine-Cosine-mode typically leads to a loss of resolution for an extended measurement range. HSSL-mode periodically transfers the current displacement as a bit series and is the preferable choice for this experiment. A workaround by using modules by Beckhoff Automation is implemented due to temporary unavailability of a data-acquisition-card with a suitable sampling frequency. The cycle time when using these modules is typically limited to $50 \mu\text{s}$. But analogue input modules (EL3702 2-channel analogue input, Beckhoff Automation, Germany) with a sub-sampling frequency up to 200 kHz are available. The HSSL-mode is adjusted for a maximum displacement of 68.7 mm and a resolution of $0.524 \mu\text{m}$. This results in a 20-bit sequence, including one stop bit. The transmission frequency of the output is set to 100 kHz (half of the sampling frequency) since the digital signal has to be reconstructed when capturing a LVTTTL-signal with an

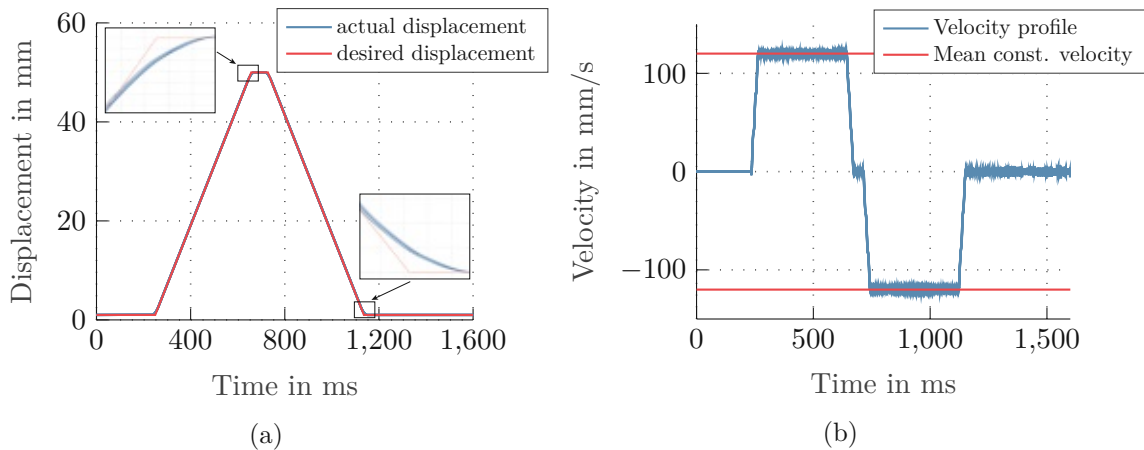


Figure 4.20: Displacement profile (a) and velocity profile (b) of a movement over a distance of 50 mm, max. velocity: 120 mm/s, acceleration: 4000 mm/s².

analogue input module. This results in an overall sample rate of 5kHz for a bit sequence, which is equal to a temporal resolution of 200 μ s.

A movement of the carriage from $x_1 = 0$ mm to $x_2 = 50$ mm (x_+) and back to $x_1 = 0$ mm (x_-) is performed, this is shown in Figure 4.20a. Setpoints for a velocity of 120 mm/s and an acceleration of 4000 mm/s² are set in the controller. Figure 4.20a shows the actual and desired displacement without considering acceleration and braking phases. The velocity is calculated by numeric differentiation of the distance data, using the central difference quotient. The velocity profile can be seen in Figure 4.20b. During phases of constant velocity a mean of $v_+ = 120.088$ mm/s and $v_- = 120.087$ mm/s is measured. A maximum deviation from the desired velocity, during phases of constant velocity of 7.016 mm/s is measured which is equal to 5.84%. In addition, the figure shows that numeric differentiation typically accentuates high-frequency components, e. g. noise, ground vibrations.

Figure 4.21 and Figure 4.22 show the displacement error between the desired and actual position of the stage carriage over a certain time, following the trajectory defined by Figure 4.20a for the ident ten repetitions, and the maximum and minimum error during phases of constant velocity. An overlay of multiple repetitions is shown to illustrate the deterministic behaviour. The spikes represent the two acceleration and deceleration phases, resulting from the desired instantaneous reach of maximum velocity. By measuring the acceleration times, which have shown to vary within a range of one millisecond over multiple repetitions and comparing them to the desired acceleration set in the controller, the actual acceleration is found to exceed the reference value by a factor of 7 – 11%.

In Figure 4.22, an enlarged section is shown. The two phases of constant velocity show a superposition of a harmonic signal and higher frequency components. By performing a Fourier transformation, the lowest frequency component is found to be between 12 to 13 Hz, which might result from the behaviour of the motor controller or the mechanical

construction, e.g. the threaded spindle which guides the carriage. By fitting a sine into the data, using Matlab's integrated trust-region method, the amplitude results to $2.9\ \mu\text{m}$ which is equal to an RMS-value of $2.05\ \mu\text{m}$. This is an error which has to be considered during the scan process and that will lead to a lateral error within the measurement plane. Higher frequency components are expected to be caused by the measurement setup since they are also present after the deceleration and decay afterwards. Especially the 3D-printed mirror support might be vulnerable to structural modes or vibrations being excited due to high acceleration forces. The peak error during phases of constant velocity is found to be approximately $11\ \mu\text{m}$. Therefore, as discussed in the previous chapter, the mechanical design is crucial to achieve high bandwidth.

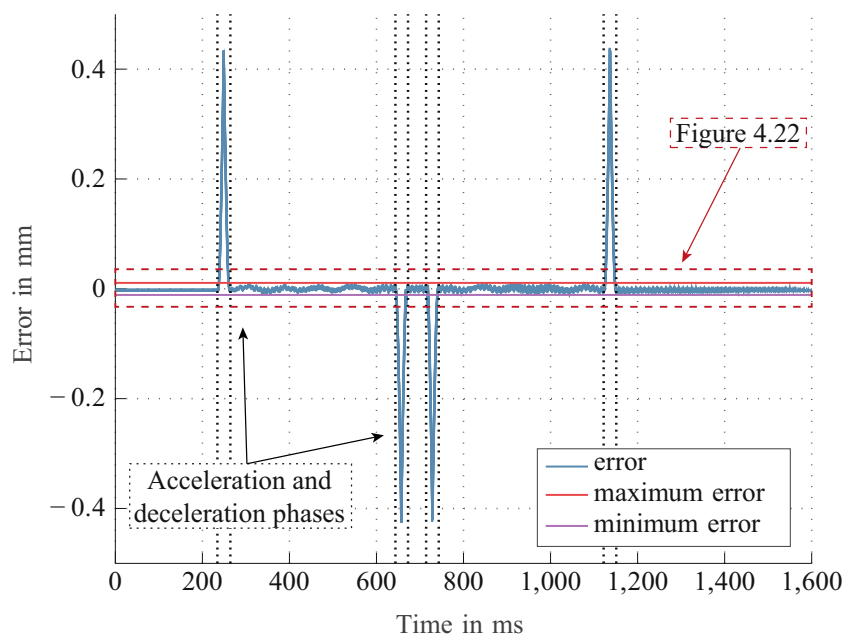


Figure 4.21: Position error during a movement over the full range of motion.

4.6.2 Industrial robot arm performance verification

As already mentioned, the main specifications of industrial robots next to their degrees of freedom, reach and load capacity are their accuracy and repeatability. Evaluating the absolute accuracy of an industrial robot requires precise distance measurement with known reference points within the workspace. In addition, tasks like laser welding, pick-and-place tasks or in-line metrology set higher requirements on repeatability than absolute accuracy since the absolute accuracy error can be adjusted depending on the task. Therefore, the repeatability in xyz-axis and the angular repeatability, resulting from the orientation of the end-effector, defined by the roll, pitch and yaw triplet, are investigated. The measurement coordination system is defined according to Figure 4.14, with the z-axis along the robot-flange and x- and y-axis parallel to the direction of movement of the

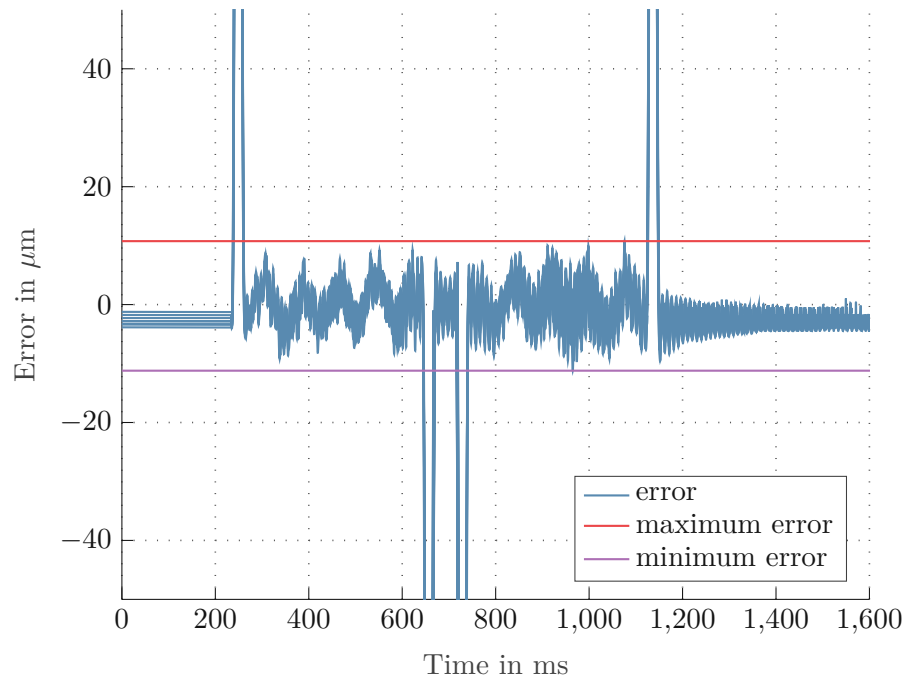


Figure 4.22: Scaled image of the position error during a movement over the full range of motion.

linear stages. In this case, the RPY-angles represent the rotation around the zyx-axis, respectively.

In general, the international norm ISO 9283 [94] specifies robot performance criteria and the evaluation process of those. Most industrial robot manufactures use this norm to determine repeatability specified in the datasheet, by referring to the unidirectional repeatability. Multidirectional repeatability can be twice the unidirectional repeatability or more according to [95]. This value is evaluated by performing a so-called inclined plane test according to the ISO 9283 norm, by defining a plane of a maximized area size within the robot workspace. Five poses are defined which should be tested with maximum load mass and velocity of the robot, within a defined time frame for a specific number of cycles. This leads to a complex characterization process. Nevertheless, manufactures tend to specify the performance only by single measures which do not represent the complexity of the evaluation process. Direct comparison is often not possible since the actual repeatability depends on, measurement points, poses, warm-up procedure and tracking model. Furthermore, the tracked location of the robot is often not defined. [95].

In addition, the thermal drift depends on the intensity of the robot movement, which leads to a varying time of decay. With thermal effects accounting for between 40 and 70 per cent of the total error in a machine tool, direct comparison is only possible with knowledge of the exact measurement parameters. [96].

In this thesis, a different approach is used to evaluate the repeatability of all three axes and orientation at the same time. For this measurement the robot is equipped with the presented metrology system, consisting out of the two linear stages and the triangulation sensor. As single point measurements are considered inconclusive, a reference sample (Figure 5.1) is scanned with a raster scan. The sample contains multiple structures that allow the determination of the orientation and the determination of the repeatability in xyz-direction. Multiple scans, whose data can be represented as point-clouds, as illustrated in Figure 4.23 for 2 individual scans, are matched by finding a transformation (translation and rotation) that minimize the euclidean error between the datasets. The interpolated data in Figure 4.23 only serves as an illustration. The matching process is also known as point cloud registration and can be realized by using an Iterative-Closest-Points (ICP) algorithm [97]. This algorithm allows the registration of point clouds by minimizing the difference between two data sets. The basic workflow consists of matching points between a moving and a fixed point cloud, the removal of incorrect matches, and determination of a transformation matrix. These steps are repeated to minimize the error until a particular stop criterion, or tolerance is reached. The result is a transformation matrix containing the translation vector and rotation information. The algorithm uses least-squares to minimize the sum of squared residuals which leads to reproducible results over multiple fits.

As discussed in Section 3.6 random errors such as sensors noise and robot vibrations can be represented by a normal distribution. Experiments have shown that if the algorithm is applied to two normally distributed datasets with additional offset and rotation, representing the robot repeatability, the translation and orientation can be determined with an error below 0.001 %. For a pose repeatability of 10 μm according to the manufacturer specifications this is more than sufficient. A large sample size is required to ensure that the scan's random error approximates the normal distribution. Therefore, a raster scan with a velocity of 50 mm/s, an acceleration of 1000 mm/s² and a lateral spacing of 400 μm over a sample area of 20x20 mm, which results in 50 scan lines, is performed. With a measurement frequency of 4000 Hz, these settings result in 90.000 data points.

For the experiment, the robot arm performs a repetitive movement between its initial pose, represented by the joint configuration shown in Figure 3.4, and the position of the sample. When the robot reaches the sample location, the scan is performed. Afterwards, the robot moves back to the initial pose. This process is repeated until temperature effects are decayed, and the steady-state repeatability can be determined. For the evaluation, each scan for one pose is matched to the first scan. This procedure is performed for two poses of the robot arm, one with the end-effector position close to the base, and one for full extension of the arm. This is illustrated in Figure 4.24. The maximum velocity of the tool-centre point is set to 1.6 m/s for both poses. This value is also used for the evaluation of the repeatability by the manufacturer for this robot type.

The results are shown in Figure 4.25. Figure 4.25a and Figure 4.25c represent the displacement along the x-y-z-axes compared to the first scan, referenced to the robot flange coordinate system over multiple scans for pose 1 and pose 2. Figure 4.25b and d represent the angular change compared to the first scan over multiple scans for pose 1 and pose 2. Using a different scan as a reference only leads to shifting along the vertical axis of the

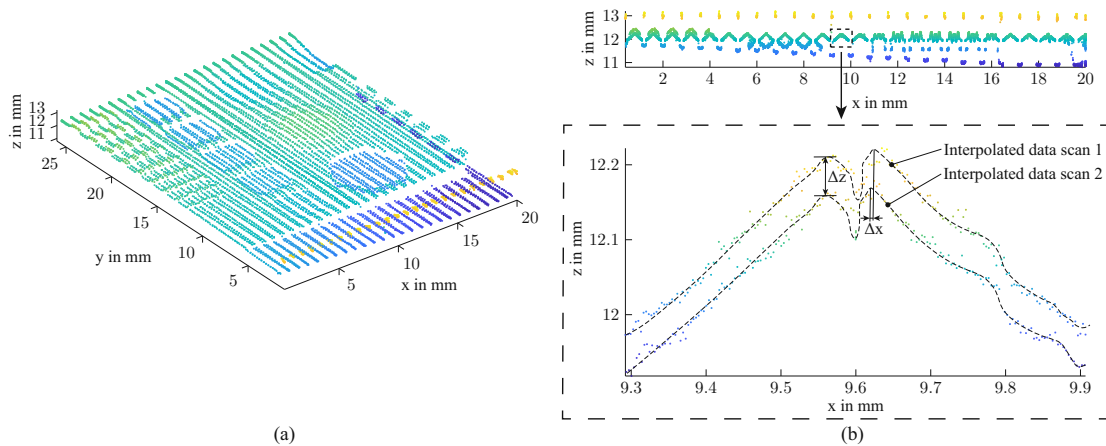


Figure 4.23: Evaluation of repeatability by scanning reference samples and performing point cloud registration.

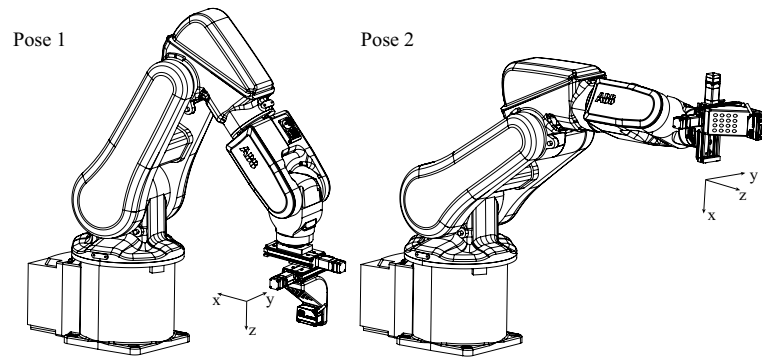


Figure 4.24: Illustration of the robot poses used during the evaluation process.

diagrams.

Due to the appearance of the curve, especially the change of translation in z-axis over multiple terms indicates thermal balancing. Thermal effects can arise from the axis motors, internal friction or changes in the ambient temperature.

The definition of the repeatability is used according to the ISO 9283 norm, which defines repeatability as three times the standard deviation and for a state of temperature balance. Table 4.3 gives an overview of the analysed data from the plots and the resulting repeatability after the decay of thermal drift.

For both poses, a strong drift of multiple tens of micrometres along the z-axis is visible. For the pose close to the base a steady state is reached after approximately 40 repetitions, while the pose of full-extension requires up to 400 repetitions for the thermal drift to decay. The first pose shows a maximum drift of $50 \mu\text{m}$ while the drift for the second pose results in up to $180 \mu\text{m}$. This might arise from more excessive utilization of joints to reach

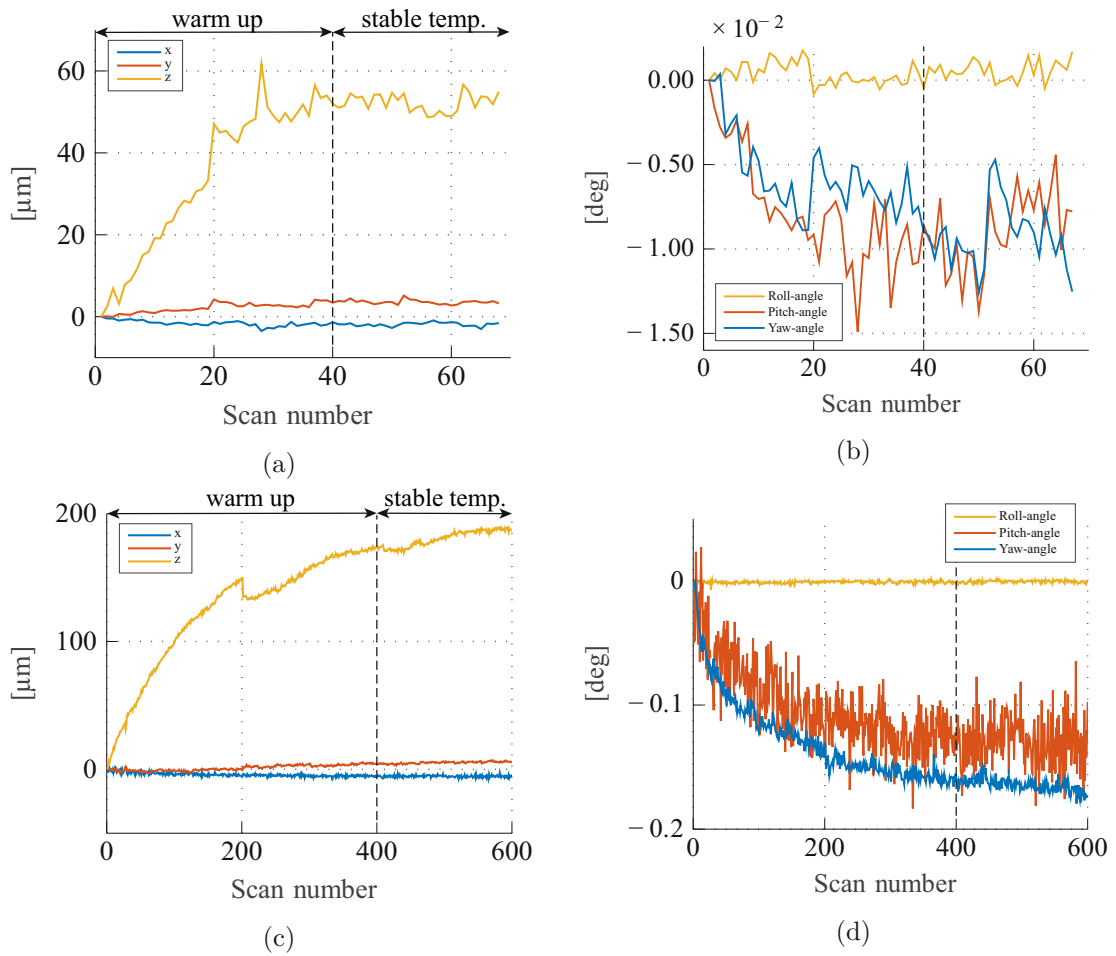


Figure 4.25: Translation (xyz) and orientation (PRY) for pose 1 and 2

	Repeatability in μm			Angular repeatability in deg.		
	x	y	z	R	P	Y
Pose 1 - close to base	1.5	1.8	6	0.0018	0.006	0.006
Pose 2 - full extension	2.1	3.3	4.4	0.0027	0.0558	0.015

Table 4.3: Robot repeatability for two poses, tool-center-point close to base and full extension.

this pose. The repeatability in the direction of z , which is the factor of main interest for this application, is found to be $4.4\ \mu\text{m}$ for pose 1 and $6\ \mu\text{m}$ for pose 2. Furthermore, the second pose measurements show that at number 200, a break of 5 minutes leads to a step due to cool down.

The repeatability in x and y , which represents a lateral displacement of the entire scan area, shows a relatively stable behaviour over all repetitions without being strongly affected by thermal effects. This also applies to the roll-angle of the angular repeatability as seen in Figure 4.25b and Figure 4.25d. The angular repeatability shows a lower, therefore better value for the first pose. Especially the pitch-angle shows a strong deterioration to 0.0558° . The reason might lie in the necessary axes configuration to achieve this pose, which requires a high angular displacement.

Generally, poses which are closer to the border of the workspace show worse performance due to a larger geometrical lever. Also, the number of involved axes when performing a movement affect the overall repeatability. A sufficient warm-up phase is required to guarantee a minimization of the repeatability. It also has to be noted that the repeatability, according to ISO 9283 (1998) is specified for the maximum supported load mass. In this case, the components show a weight of approximately 1 kg which is only a third of the maximum load mass (cf. Figure 4.14). Therefore, a lower weight might improve the performance of the robot compared to the specifications.

The experimental results lead to the following conclusion by considering that the triangulation sensor's lateral resolution depends on the laser spot size on the sample surface [98] and under the assumption that the robot is initially positioned at the optimal distance for a spot size of $55 \times 50\ \mu\text{m}$. If no sufficient warm-up phase has been performed a displacement drift along the z -axis of up to $180\ \mu\text{m}$ leads to an increase of the spot size to $56.35 \times 52.7\ \mu\text{m}$ according to Figure 4.5, under the assumption of linearity within this range. The resulting error of 1.35 and $2.7\ \mu\text{m}$ is small compared to the actual spot size and is in the nanometre range for the state of temperature balance and repeatability of up to $6\ \mu\text{m}$. This leads to the conclusion that the resulting error is neglectable for this setup and the used triangulation sensor. Nevertheless, the behaviour of the robot is of great interest for various applications in particular for applications where a closer distance to the target is required, e. g. if a chromatic confocal sensor with a measurement range of multiple hundreds of micrometres is used as discussed in Section 2.1.1.

4.6.3 Verification of the triangulation sensor behaviour

This section deals with the behaviour of the triangulation sensor and the impact of the robot and floor vibrations on the measurement precision. In Figure 4.26 the signal of the triangulation sensor, after approaching a target position with the robot and by measuring on a fixed position, can be seen. A measurement point on an anodized aluminium plate with additional rubber bumpers to reduce the impact of ground vibrations on the target represents the target position. In this case, the laser is turned on after the position is reached, and the measurement is initiated. This is set as a requirement due to laser class

2 of the laser source as discussed in Section 4.1.3. Exponential decay is visible and by performing multiple repetitions the time constant of the fitted exponential functions is found to be in a range of 5.2–7.8 s. This slow dynamic indicates that a thermal drift of the triangulation sensor’s components is responsible for this effect. When performing raster trajectories, this effect leads to a tilt of the measurement plane. Especially for Lissajous trajectories, the consideration of the impact on the measurement result is essential since the decay can introduce a ripple in the data.

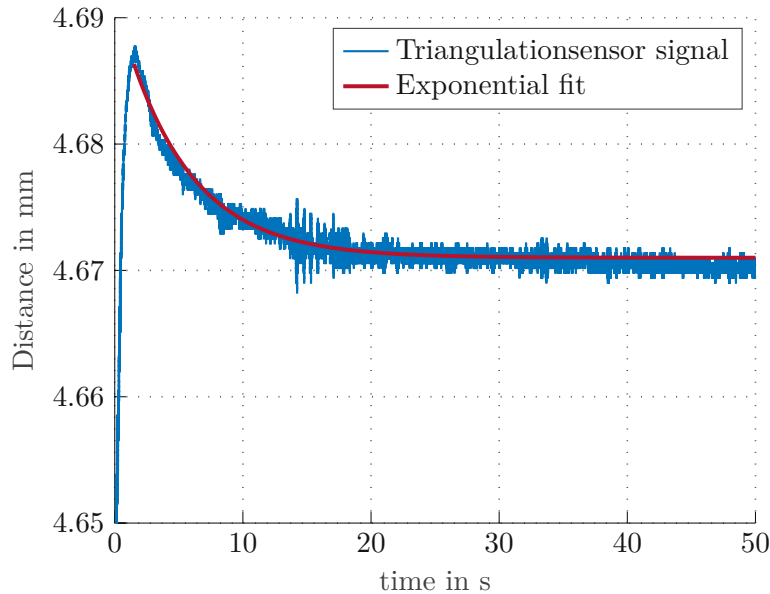


Figure 4.26: Thermal drift of the triangulation sensor after switch-on.

Within ten repetitions a maximum drop-off of $15.3 \mu\text{m}$ was measured. By assuming that the noise amplitudes are normally distributed, this leads to a standard deviation in a range of $0.4 - 0.6 \mu\text{m}$ and therefore to a degradation of the repeatability of the sensor signal from $1 \mu\text{m}$ to $1.2 - 1.8 \mu\text{m}$. Figure 4.27 allows the separation of the noise into a proportion linked to the sensor and second part resulting from floor vibrations and vibrations of the robot arm. After the robot is in a static position for more than two minutes, the robot control turns off the motor’s hold currents and locks the joints. This leads to a drop-off of the tool-centre-point by up to $45 \mu\text{m}$ or more depending on the load mass. In this current-free state, the noise is defined by the sensor repeatability and floor vibrations, which is approximately $1 \mu\text{m}$.

As a final experiment the sensor is mounted in a static position on a profile bar attached to the anodized aluminium plate with additional rubber bumpers to separate the behaviour of the triangulation sensor from floor vibrations. This measurement results again in a standard deviation of 333 nm which is equal to a repeatability of $1 \mu\text{m}$. This leads to the conclusion that floor vibrations in this laboratory environment fall below the sensor resolution. Nevertheless, they have to be considered for the application in an industrial environment, as discussed in Section 3.6.

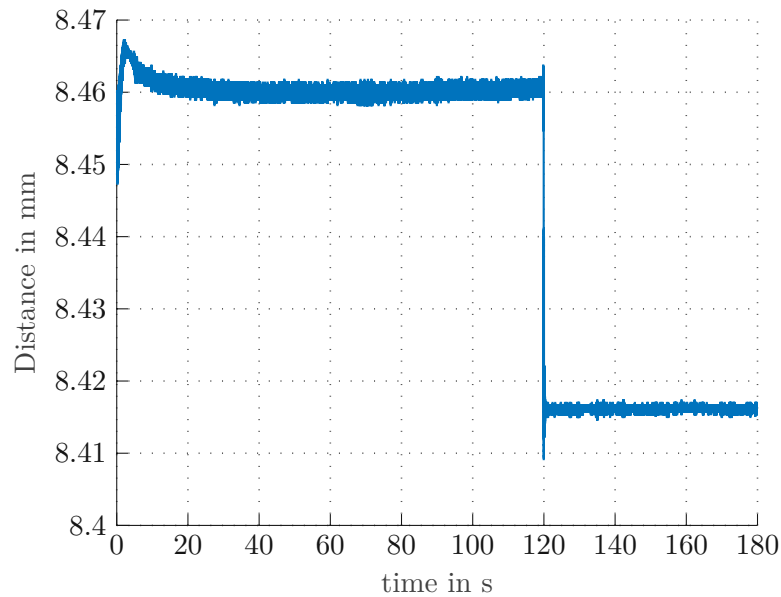


Figure 4.27: Triangulation sensor turn on behaviour and disconnection of the robot joint's motor current.

As discussed in Section 3.6 mutually independent normal distributed variables can be combined by the method of the root of the sum of squares. A sensor noise standard deviation of 333 nm and a combined standard deviation of sensor noise and robot vibrations of 600 nm lead to a standard deviation of the robot vibrations of 499 nm.

4.6.4 Summary of the verification process

The findings of the previous sections can be summarized as follows. The linear stages fulfil the specifications stated by the manufacturer. For point-to-point movements, an accuracy of $0.355 \mu\text{m}$ and repeatability of $1.372 \mu\text{m}$ is achieved. For a continuous movement, a velocity and acceleration fluctuation up to 5.84 and 11 percent respectively, of the desired value can occur. A deterministic harmonic error with an amplitude up to $2.9 \mu\text{m}$ is present during phases of constant velocity for maximum velocity. The industrial robot arm can achieve a repeatability down to $6 \mu\text{m}$ if a sufficient warm-up phase is performed. Without warm-up phase, a displacement drift up to $180 \mu\text{m}$ was measured. For this application, this leads to a neglectable error. The triangulation sensor fulfils the specifications, and the repeatability was found to be $1 \mu\text{m}$. Nevertheless, a thermal drift of up to $15.3 \mu\text{m}$ was measured, which can be considered to be a deterministic error. While floor vibrations of the laboratory environment were found to fall below the sensor resolution, vibrations of the robot joint's motors lead to a random error with a standard deviation of 499 nm.

5 Experimental validation of the system performance

After the prototype creation, accuracy, precision, repeatability and the overall performance of the system is evaluated by various experiments which are presented and discussed within this chapter.

A reference sample, as shown in Figure 5.1 with defined step heights and dimensions was designed to evaluate the accuracy and resolution of the scanning system. The sample was 3D printed using by using a printer based on the stereolithography (SLA) technology. SLA-printers are suitable for fast prototyping and can achieve consistently higher resolution and accuracy than fused deposition modelling (FDM) printers. The resolution of FDM printers is defined by its nozzle size and the precision of the extruder movement. In addition, when printing elevated surfaces, artefacts might occur due to the pull-off of the filament. SLA printers harden light-curable polymers by utilizing ultra-violet laser light which is directed by using mirror systems. After the sample creation, a coordinate measuring machine (CMM), equipped with a chromatic confocal sensor was used to perform a reference scan [99].

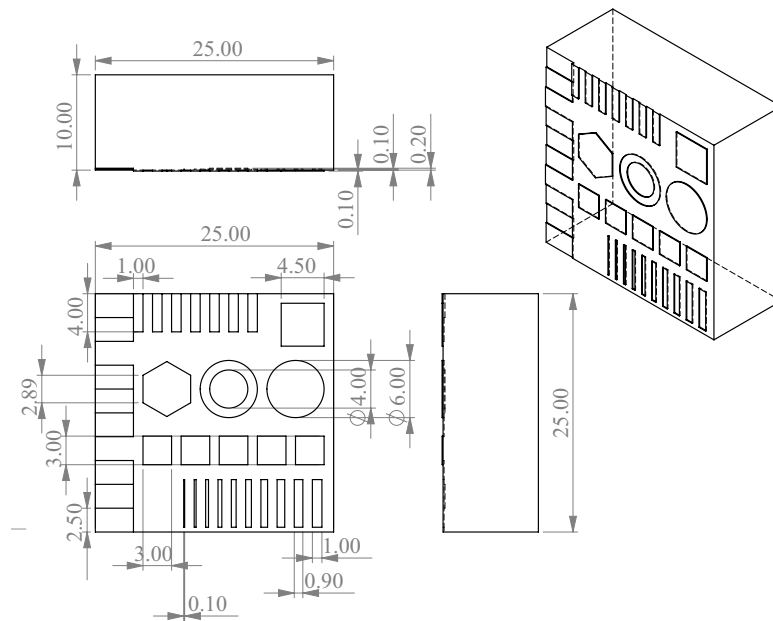


Figure 5.1: Calibration samples for system verification, dimensions in mm.

5.1 Vibrations and acceleration forces

In this section, the impact of high accelerations and different trajectories, e. g. raster- and Lissajous trajectories, on the mechanical structure of the robot is investigated. As already discussed in Section 2.3 raster trajectories tend to excite higher frequency components or structural modes within the mechanical structure due to high acceleration forces around the turning points. This leads to a decrease in overall measurement accuracy. Smooth scanning trajectories may overcome this issue. For comparison fundamental raster trajectories and Lissajous trajectories are selected. As discussed in Section 2.3 Lissajous trajectories can provide a fast overview of the scan area and are of special interest for this applications, in particular for feature detection as shown in Section 4.3.2.

The measurement setup is shown in Figure 5.2. The impact of trajectories is analysed using the IDS3010 interferometer by Attocube Systems AG once again by using the ident fixed focus fibre collimator F240FC-1550 by Thorlabs GmbH measurement head. An additional mirror with precision screws is mounted between the measuring head and the reflective mirror attached to the metrology system to simplify the alignment process. This leads to a measurement distance of approximately 300 mm. A maximum displacement in the range of multiple tens of micrometres is expected. As discussed in Section 4.6.1 the interferometer shows a Rayleigh distance of 5.19 m which is more than sufficient for this measurement range. The second reflective mirror is attached to the linear stage closest to the robot flange to measure the maximum possible displacement since the intermediate stage has to support the weight of the sensor, adapter and the second stage. This leads to higher reaction forces for a desired acceleration set in the controller due to higher mass.

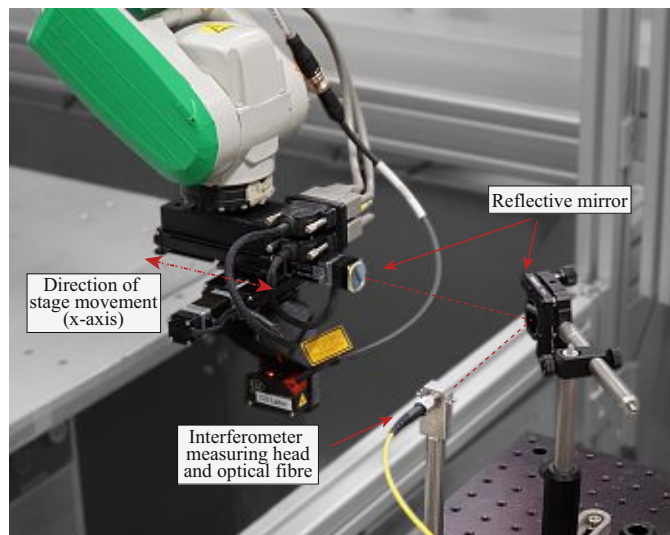


Figure 5.2: Measurement setup to investigate the impact of acceleration forces on the mechanical structure of the system.

Measurements have shown that the impact of an orthogonal motion, e. g. the movement

of the second axis, on the displacement along the optical axis, is in the submicrometre range and therefore neglectable for this characterization. For the experiment only the carriage of the intermediate stage is moving cyclical between $x_1 = 0$ mm and $x_2 = 50.8$ mm. Since this is a one-dimensional movement the trajectories are defined by a triangular and sinusoidal motion for the following experiments.

For direct comparison, equal amplitude A and frequency f of the trajectories are selected, as shown in Figure 5.3 for a range of motion of 50.8 mm. In addition, the acceleration of the triangular trajectory is set identical to the maximum acceleration of the harmonic movement. The maximum acceleration of a sine-motion is calculated according to (5.1). In general, the frequency is limited due to the maximum velocity of the stages. The frequency is inverse proportional to the amplitude according to (5.2). This leads to a frequency of $f = 0.76$ Hz, a maximum acceleration for both trajectories of 570.1 mm/s², a maximum velocity of 120 mm/s for the sinusoidal trajectory and a constant velocity of 76.72 mm/s between acceleration phases for the triangular trajectory.

$$a_{max} = A(2\pi f)^2 \quad (5.1)$$

$$f_{max} = \frac{v}{2\pi A} \quad (5.2)$$

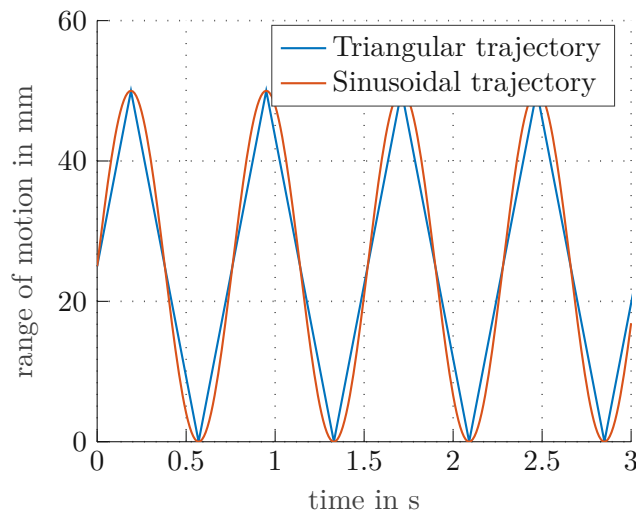


Figure 5.3: Triangular and sinusoidal trajectory for equal amplitude and frequency.

Figure 5.4 shows the resulting displacement of the mechanical structure along the axis of movement for triangular and sinusoidal trajectory according to Figure 5.3. It can be seen that the usage of triangular trajectories leads to the excitation of higher frequency components in addition to the visible linear decrease and increase, which can lead to a drastic reduction of the lateral measurement precision. The maxima are located at turning points, and decay of the high-frequency amplitude over phases of constant velocity

is visible. On the other hand, sinusoidal trajectories show a smooth harmonic displacement with a frequency equal to motion frequency. The triangular trajectory results in a maximum displacement amplitude of $18.5 \mu\text{m}$, while the maximum error amplitude of the sinusoidal trajectory is $3.67 \mu\text{m}$, which leads to a decrease by an approximate factor of five. The visible steps are caused by the selected resolution of $0.524 \mu\text{m}$ of the interferometer's real-time output used in HSSL-mode as discussed in Section 4.6.1.

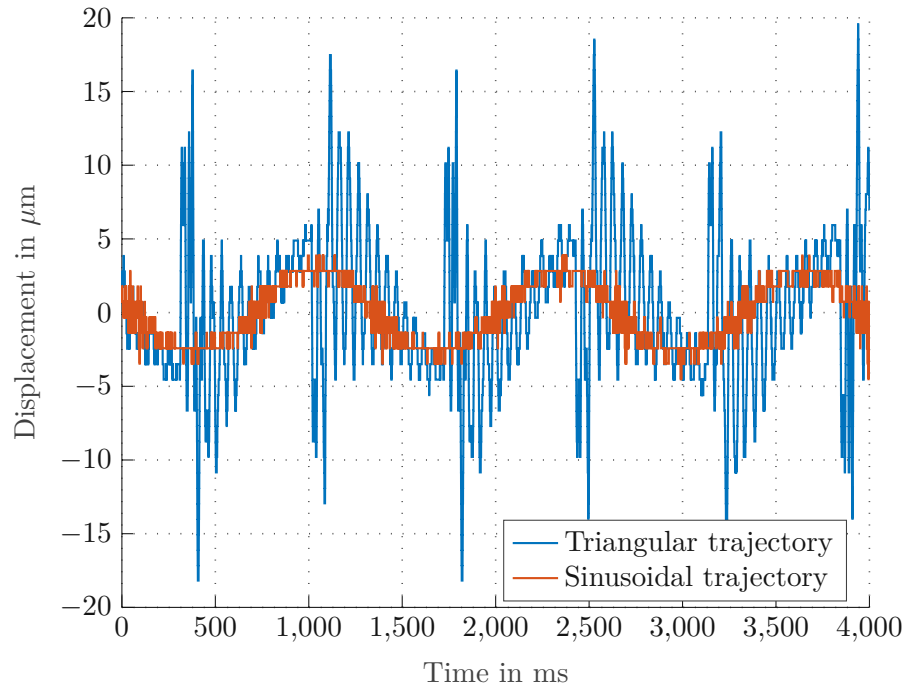


Figure 5.4: Displacement due to raster and Lissajous trajectory for equal amplitude, frequency and maximum acceleration.

Due to the fact that no additional frequency components are excited by the sinusoidal trajectory, a model of displacement depending on the frequency can be created. This characterization of the displacement error allows post-processing respectively correction of the measurement data, e. g. the lateral position data according to a model based on the displacement data.

As a second experiment, the resulting displacement along the axis of motion depending on the frequency is investigated. Smaller scan areas allow higher frequencies but may lead to stronger displacement. The maximum acceleration setpoint for the controller is limited to approximately 13 m/s^2 . A specified maximum force of 25 N and weight of 760 g (sensor, sensor adapter, top stage and carriage of the intermediate stage) would result in a maximum acceleration of 32.9 m/s^2 , which would exceed the motor current limit and could lead to a reduced lifetime of the components.

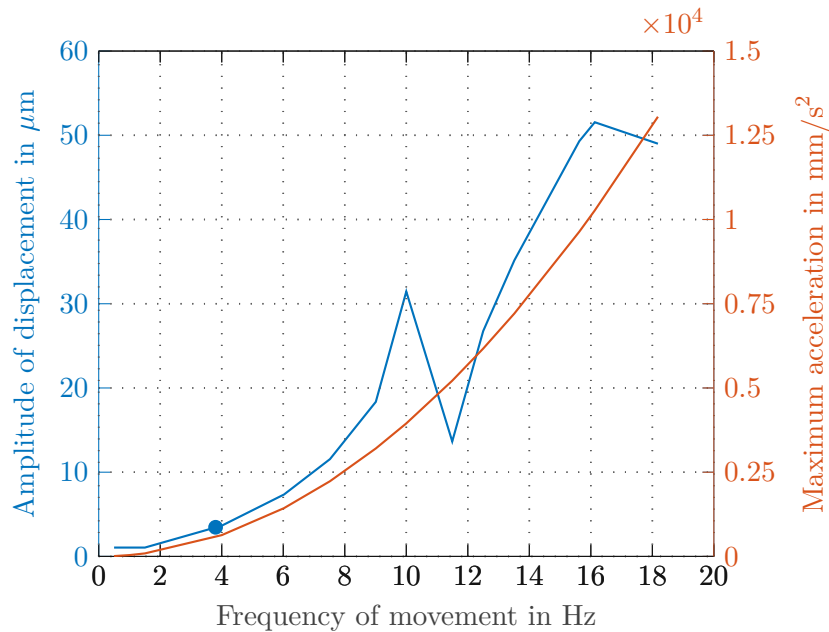


Figure 5.5: Displacement and acceleration of sinusoidal trajectories depending on the frequency.

For the experiment the carriage of the intermediate stage is moving cyclical between $x_1 = 0$ mm and $x_2 = 1$ mm. The frequency is increased up to the maximum value of 18.18 Hz for this range of motion. Figure 5.5 shows the resulting displacement along the axis of movement and the required acceleration for the specific frequency. By considering the settings from the previous experiment, a distance of 50.8 mm allows a maximum frequency of 0.76 Hz and requires a maximum acceleration of 570.1 mm/s². This is equal to a frequency of 3.8 Hz for a distance of 1 mm. The resulting displacement fits the curve from the second experiment, marked as a blue dot. In addition, at 10 and 11.5 Hz a small resonance and anti-resonance is visible, which might be a consequence of the limited stiffness of the robot joints and an excitation frequency close to an eigenfrequency of the robot arm.

The experiments conclude that both trajectory types result in a displacement of the metrology system along the axis of movement, due to a limited stiffness of the robot arm. The resulting displacement of triangular and sinusoidal trajectories show a deterministic behaviour (cf. Figure 5.4). A model can be created to compensate for the displacement and can be applied to Lissajous and raster trajectories. This task is simplified for Lissajous trajectories due to the dominant frequency component equal to the movement frequency. Scan data can be post-processed by utilizing this model. Raster trajectories require a more complex model due to high acceleration forces around turning points. For surface inspection, the dynamic adjustment of the scan area depending on the sample size is of interest. Figure 5.5 shows that the resulting displacement error can be estimated depending on the frequency, range of motion and required acceleration.

5.2 Out-of-plane resolution and precision

After evaluating the main error sources and their characterization as systematic or random errors, this section describes the determination of the overall system's out-of-plane resolution. The resolution is defined as the smallest measurable change in quantity, leading to a detectable change in the measured value [76]. The measurement setup is presented in Figure 5.6. One linear stage is mounted on an anodized aluminium plate in a vertical orientation by using 3D-printed adapter components. On the stage carriage, an adapter with the SLA-printed reference sample is mounted. One micro-step of the stepper-motor-based linear stages leads to a displacement of $0.1905 \mu\text{m}$. Since the sensor resolution is equal to $0.385 \mu\text{m}$ the usage of the linear stage, to produce changes in height along the z-axis, is reasonable for this task.

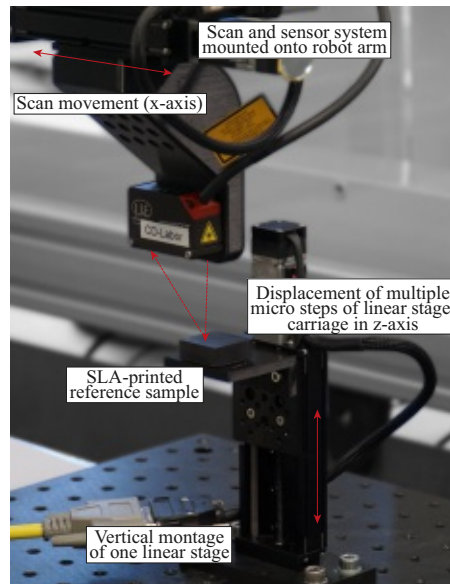


Figure 5.6: Measurement setup to determine the resolution of the system.

For the first experiment, the robot moves to the sample position and a measurement in a static position without stage movement is performed. Meanwhile, the vertically mounted stage performs a displacement of one micro-step per second. The result can be seen in Figure 5.7. As evaluated in Section 4.6.3 the triangulation sensor shows a repeatability of $1 \mu\text{m}$. Nevertheless, the result proves that a change of height equal to two micro-steps of the linear stage can be distinguished clearly. This leads to the conclusion that the resolution of the measurement system is equal to the sensor resolution of $0.389 \mu\text{m}$. Changes of height equal to a single micro-step, e.g. at time $t = 1, 3, 5 \text{ s.}$, can not be captured since they fall below sensor resolution.

For a second experiment the goal is to simulate a typical scan process, e.g. a part of a raster scan where only one axis is active at a time. Therefore, the robot moves to the

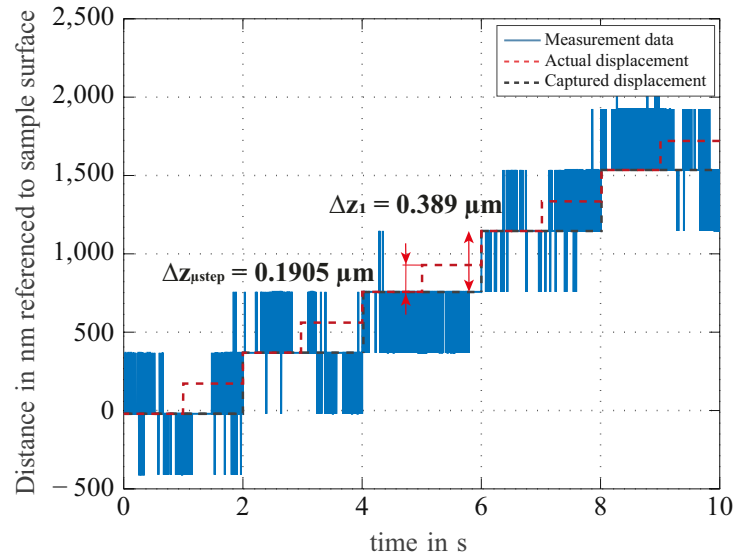


Figure 5.7: Evaluation of the out-of-plane resolution for a displacement of 1 micro-step per second.

position of the sample, and a line scan over the reference sample is performed, while the vertically mounted stage performs a displacement of the carriage of multiple micro-steps.

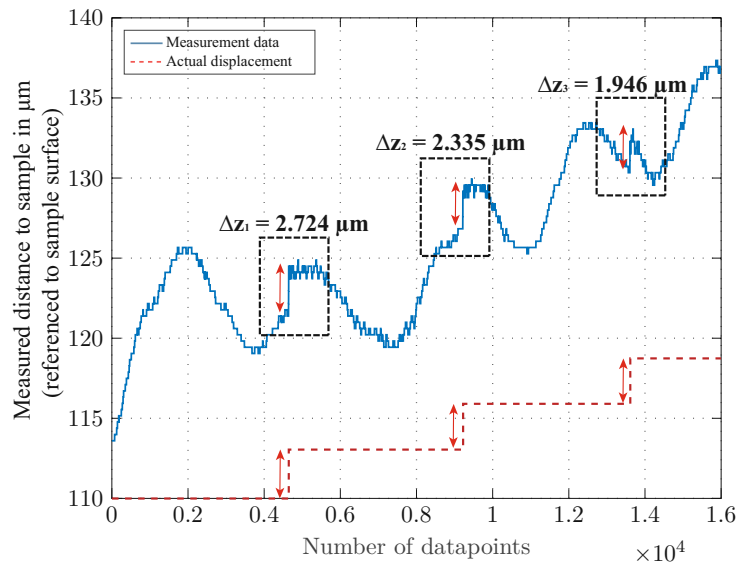


Figure 5.8: Evaluation of the out-of-plane resolution for a displacement of 15, 13 and 11 micro-steps during a scan movement.

Figure 5.8 shows a part of a line scan over a flat area of the reference sample without

structures, with an additional displacement of 15, 13 and 11 micro-steps, which is equal to a 2.888, 2.476 and 1.905 μm step. By analysing the data, the measured difference in height between the steps is found to be exactly equal to 0.385 μm . Even for the maximum stage velocity and the additional impact of sensor noise and robot vibrations it is possible to distinguish between changes in height with the resolution of the sensor.

Nevertheless, additional information can be gained from this data. Measurement and sample plane are not perfectly parallel which leads to an overall increase of the measured distance from 114 to 136.5 μm . The sample might show a curvature too. But in addition, a harmonic displacement is visible, which can impact the precision of the scan result if, e.g. the positioning system is responsible for this behaviour. Since this effect was not characterized yet, a comparison between a scan of a reference sample of a coordinate-measuring-machine and the robot-based system is necessary. This is carried out and analysed in the following section and allows an assignment of the error to the sample surface or the system.

5.3 Measurement results

In this section, the result of a raster scan of the robotic measurement system is compared to a raster scan of a coordinate-measuring-machine (CMM), created by [99], to determine the accuracy and precision of the system and to investigate additional effects on the measurement result. The CMM performs point-to-point measurements and shows precision and resolution in submicrometre range and serves as a fair comparison. The CMM performs a basic raster scan with a grid spacing of 50 μm . The slow, but precise CMM-setup leads to a scan duration of multiple days due to the area size. Due to the long duration only a section of the reference sample is scanned, as shown in Figure 5.9. This scan results in a smooth result with low noise. Although the scan shows grooves parallel to the y-axis, which might be caused by eccentricity of the spindles which guide the sample carriage of the CMM.

The reference sample with an area of 25x25 mm (cf. Figure 5.1) is scanned by using a raster scan with a lateral spacing between two lines of 50 μm which results in 500 lines for the entire sample. The direction of fast axis is along the y-axis while the second stage only performs the 50 μm displacement between two lines. The measurement coordinate system is aligned according to Figure 4.14. To limit the impact of high-acceleration forces for the comparison of the two raster scans, the stage acceleration is set to 500 mm/s^2 . This results in a maximum velocity of 111.8 mm/s at the centre of the stage and results in an uneven distribution of measurement points along the raster line. Nevertheless, the resulting lateral data point spacing still exceeds the reference scan's resolution by a factor of 1.66 at the point of lowest resolution and allows reasonable comparison. These parameters result in an overall scan time of 223.5 s. For practical application, the scan time could be strongly reduced down to approximately 105 s for this specific example by using higher acceleration and by compensating for errors caused by high acceleration forces as discussed in Section 5.1 to avoid a loss of measurement precision around turning points. The result can be seen in Figure 5.10.

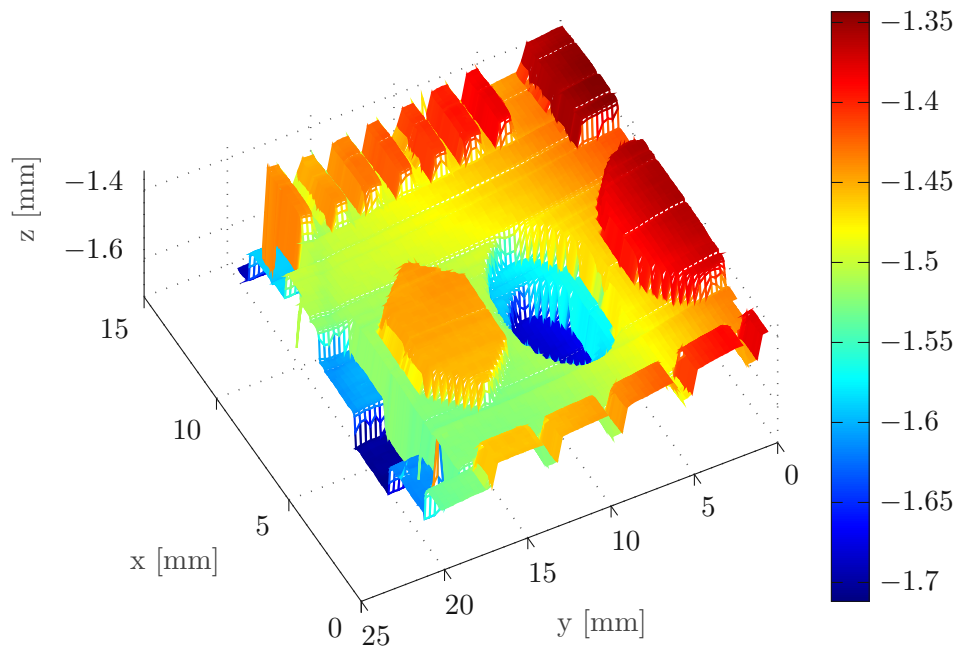


Figure 5.9: Scan of a section of the reference sample using a coordinate-measuring machine (CMM), fixed lateral resolution of $50\ \mu\text{m}$.

Grid and data point spacing are not completely identical and the scans results from systems referenced to a different coordination system. To directly compare both sets of data, where each data point is represented by its xyz-distance value respectively, the data sets have to be registered. Point cloud registration is carried out by using an ICP-algorithm [97] and following the same procedure as discussed in Section 4.6.2. Compared to Section 4.6.2 the data is unevenly distributed between the datasets and the registration is complicated. Therefore, the data sets are aligned manually in first place to increase the convergence speed of the ICP algorithm, which also leads to a higher likelihood of a correct alignment. To calculate the error between the two datasets, data points, which lead to a minimization of the euclidean distance within the xy-plane, are matched with each other using a k-nearest-neighbour- (KNN-) algorithm to process large data sets efficiently [100]. Afterwards the out-of-plane error is calculated which is shown in Figure 5.11. The CMM-scan only covers a part of the reference sample, therefore the coordinate system of Figure 5.11 is equal to Figure 5.9 while the other plots showing the full sample are referenced to Figure 5.10.

The borders of structures indicate a remaining error due to a small misalignment of the datasets concerning orientation and translation from the registration process. These errors will be neglected for the determination of the overall error and the determination of the

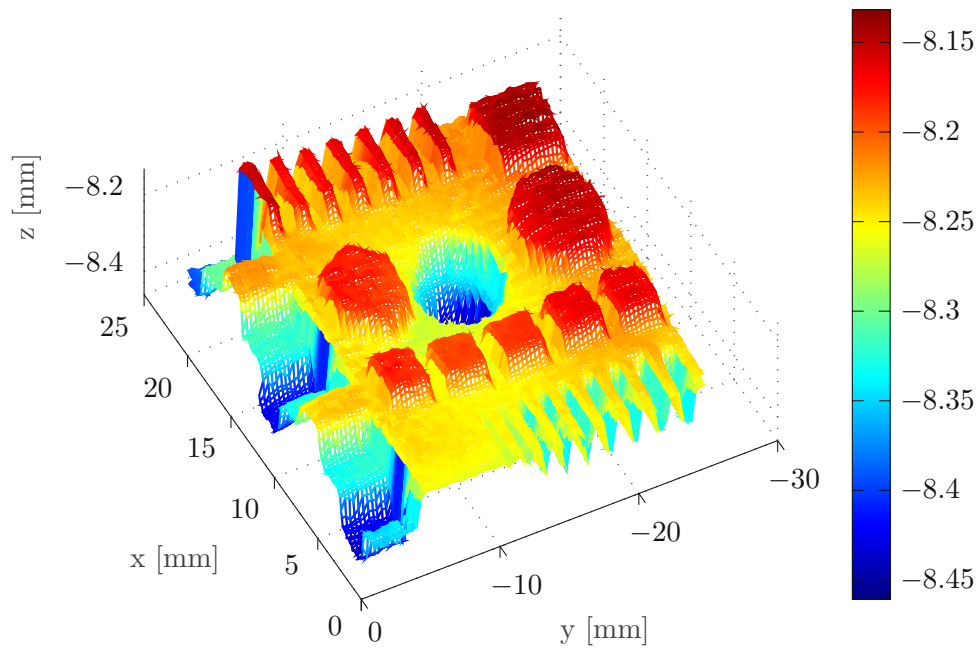


Figure 5.10: Raster scan of the reference sample, $50\ \mu\text{m}$ lateral resolution in x .

systems precision and accuracy.

Similar to the observed harmonic waves in Section 5.2, the scan and the resulting error show a periodic pattern. This is not visible in the CMM-scan and a rotation of the sample during scan processes by 90° (see Figure 5.12) proves that this pattern must be associated with the scanning system. The dominant frequency of the pattern shows a spatial wavelength of $0.82\ \text{mm}$ which is equal to a spatial frequency of $1.22\ \text{mm}^{-1}$ and is the main remaining uncompensated error source to impact the overall accuracy and precision of the system. This effect is considered to result from a combination of straightness, flatness and the Abbe error as discussed in Section 3.6.

Figure 5.13 shows the direct comparison of the results of both measurement systems as cross-sections through yz - and xz -plane, which directly result from the point cloud registration process.

In Section 4.6.3 the impact of the robot motor current switch off on the tool-center-point's position was discussed as shown in Figure 4.27. This is visible in the error plot as a dividing line at $x = 2.4\ \text{mm}$ along the y -axis. Also the right column of the section views show a higher divergence between the two measurements from $x = 0$ to $4.5\ \text{mm}$ due to this effect.

Table 5.1 shows an overview of the resulting error standard deviation for overall scan

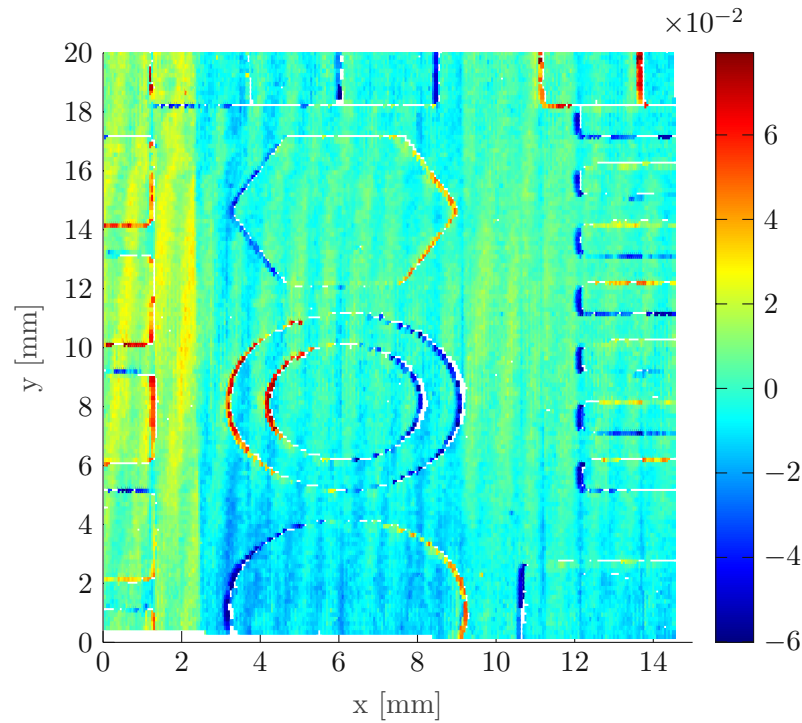


Figure 5.11: Error normal to xy-plane between scans of the robotic measurement system and the CMM machine.

(Figure 5.11) and each sectional view in Figure 5.13. The error due to the robot-arm drop-off is taken into account and compensated for the evaluation. Nevertheless, the table shows the result for the scanning data without additional usage of filters. The usage of filters for postprocessing of data, preferably edge-preserving filters can further decrease the error standard deviation of the final result down to approximately $5 \mu\text{m}$ without strongly affecting the out-of-plane and in-plane resolution due to too strong smoothing. A possible choice is a median- or Savitzky-Golay filtering, which leads to a preservation of edges but requires parameter adjustment depending on the application [101].

With the resulting data, the accuracy and precision of the system can be defined. The accuracy indicates an error that is inherent to the measurement. While the precision similar to repeatability represents the scatter of data around their actual value typically expressed in terms of standard deviation or variance.

To evaluate the accuracy in z, the error of all areas of constant height is calculated individually and expressed by its mean value. Afterwards, an overall mean value for the error is calculated, representing the accuracy of the scan. Individual consideration of constant height areas leads to equal weighting independently of the area size and serves as a more general representation. The accuracy is equal to $3.4 \mu\text{m}$

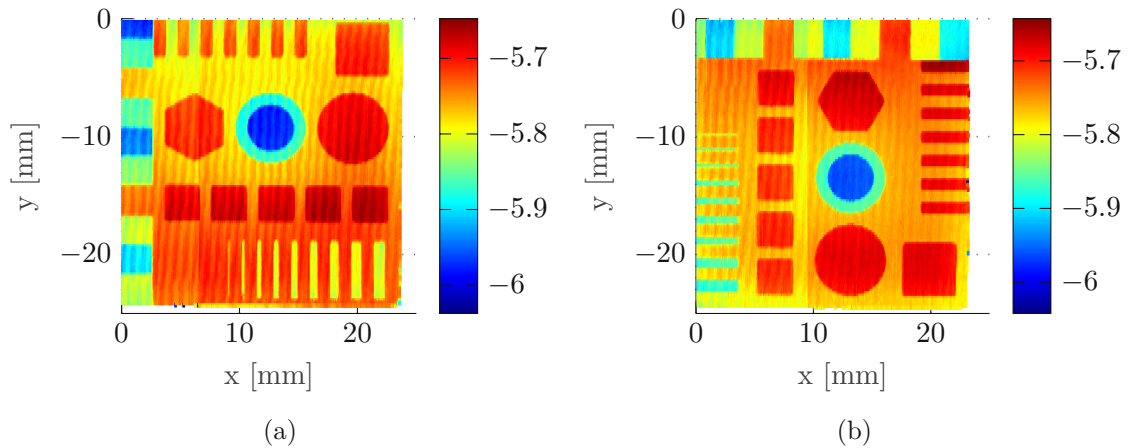


Figure 5.12: Scans of the reference sample with a rotation of 90° around the z-axis showing an identical periodic pattern along the x-axis.

Sectional view	Standard deviation of error in μm (cf. Figure 5.13)
yz-view, line at $x=12$ mm	5.4
yz-view, line at $x=6$ mm	7.1
yz-view, line at $x=1$ mm	6.9
xz-view, line at $y=19$ mm	6.2
xz-view, line at $y=9$ mm	6.4
xz-view, line at $y=4$ mm	6.1
Overall standard deviation of error in μm	7.4
Mean of error in μm	3.4

Table 5.1: Error standard deviation and mean value.

The precision of the measurement is affected by random errors, e.g. sensor noise, robot vibrations, vibrations induced by the positioning system, and the positioning system's behaviour. Therefore, precision is defined by three times the overall error standard deviation and is equal to $22.2 \mu m$.

5.3.1 Repeatability

Next to the precision of the measurement during the scan, the complete measurement process's repeatability is evaluated. In order to determine the repeatability, the entire process sequence is carried out according to the sequence control (cf. Figure 4.13). Since the sample's exact position within the measurement coordination system is not of interest, and the robot's repeatability mainly leads to an offset or tilt of the entire set, the error between two data sets is calculated according to the previous section. Therefore, the hereby evaluated repeatability does not include the robot's position repeatability. Figure 5.14

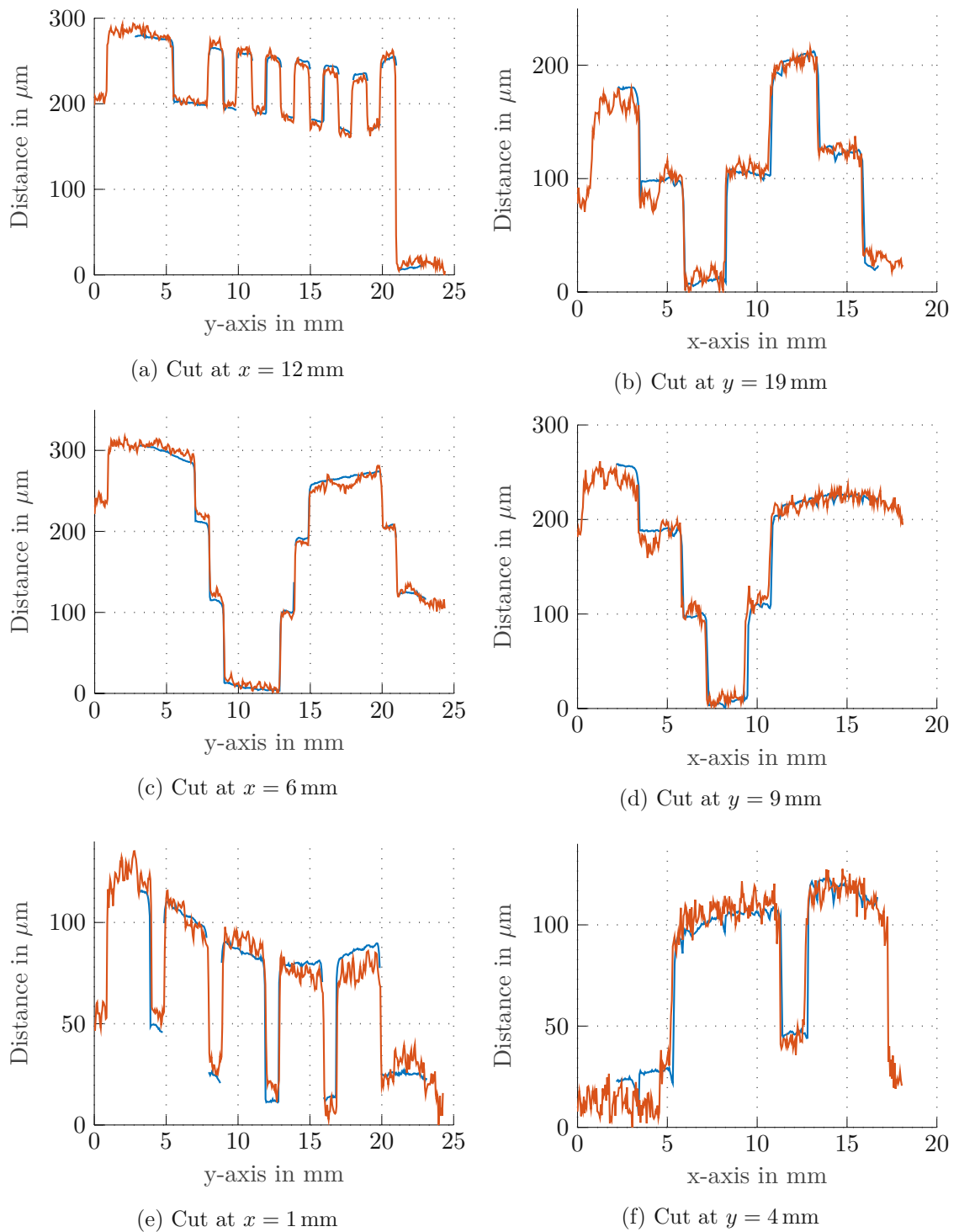


Figure 5.13: Comparison of CMM (blue) and robot-based metrology system (red) for cross sections in yz (a-c-e) and xz (b-d-f) plane.

displays the z-axis error which shows a standard deviation of $2.4\ \mu\text{m}$ and a mean value of zero. This leads to a repeatability of $7.2\ \mu\text{m}$. Local deviations between scans are caused by random errors such as sensor noise and induced vibrations from different sources and also temperature behaviour of the stages, e.g. thermal expansion of the precision lead screws that guide the carriage.

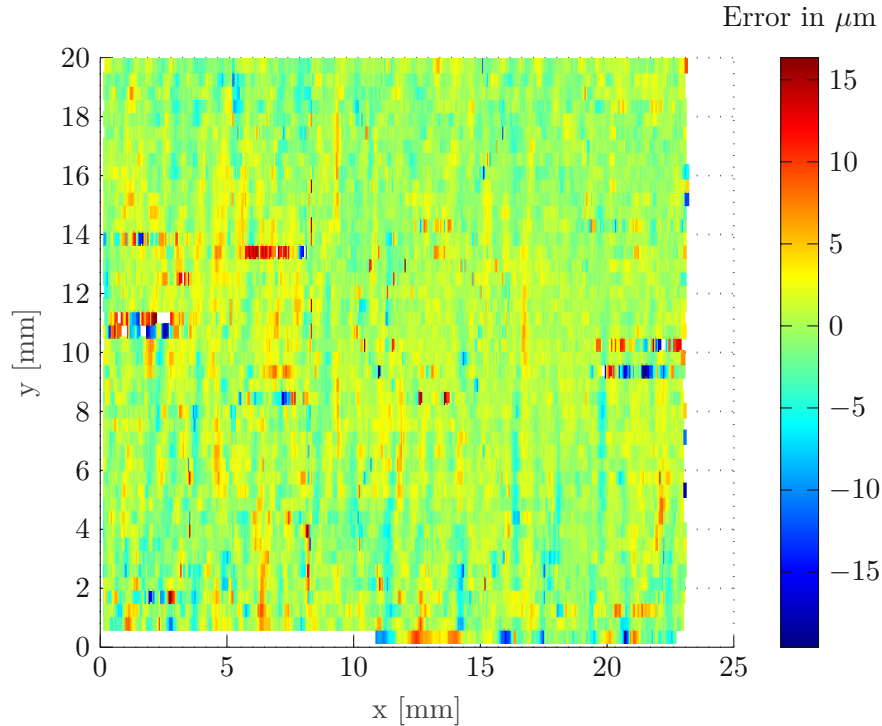


Figure 5.14: Error normal to the xy-plane between two scans of the robot-based system.

5.4 Robot pose adjustment

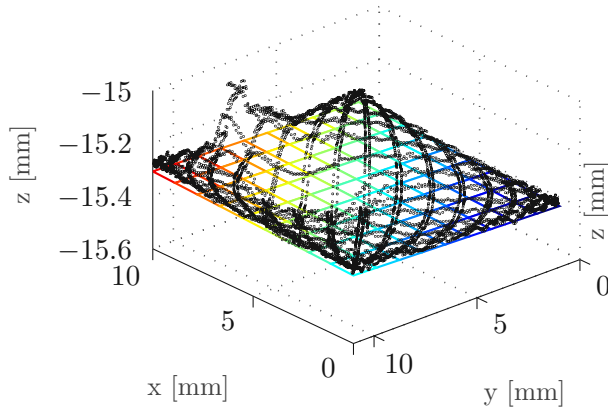
Optical measurement systems (e.g. confocal or triangulation sensor) show a dominant focus point and a varying spot size over their measurement range as shown in Figure 4.5 for the used triangulation sensor. As discussed in Chapter 4.3, the data from a coarse scan can be used to compensate for sample orientation and to align the measurement system in optimal distance. In this section, an approach by utilizing plane fits is presented. For parallel alignment of measurement and sample plan, a dominant plane within the measurement area has to be determined. In relation to the flat scan plane, a linear plane fit is desired. Therefore, it is assumed that a plane with low curvature κ , with κ below 0.008, exists within the scan area, leading to a unique solution. To solve this problem, multiple solutions are available, e.g. least-squares and RANSAC algorithms, for a large variety of applications. Least-squares is based on finding a suitable parameter vector to minimize a function which represents the sum of the squared errors between measurement data and the resulting plane values. In general, a basic least-squares algorithm is not robust

against noise or the presence of outliers which significantly alter the quality of the fit. To overcome this issue, a weighted least-squares problem can be formulated by penalizing large residuals and preferring small residuals. While this method reduces the influence of outliers, in some cases, starting with too many outliers will prevent the algorithm from converging. [61]. A widely used approach, especially for machine vision applications, is the so-called random-sample-consensus (RANSAC) [102]. This approach starts by selecting a random number of samples (e. g. three samples for a plane fit), which are used to compute an initial estimate for the model. Afterwards, the residuals of the model to the sample data are computed, and the number of inliers is counted. RANSAC typically requires a parameter defining the maximum distance to sample points to be accepted as inliers. This parameter depends on application and structural dimensions. This process is repeated for a fixed number of repetitions or until a certain quality criterion is fulfilled.

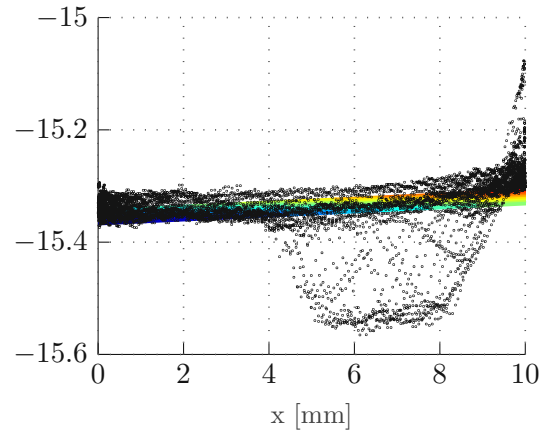
Figure 5.15 shows the result when performing plane fits with least-squares and RANSAC algorithm. Figure 5.15a-c show a least-squares fit for the weld spot and the surrounding area from the previous section (cf. Figure 4.11), data points of the Lissajous scan are marked with black circles. The least-squares algorithm leads to the same solution for each repetition of a given set of data and is an appropriate choice if only one main plane is to be expected. Figure 5.15d shows the result of a raster scan over an area that includes a step with a height of 10 mm and clearly shows limitations of the basic least-squares algorithm due to a large number of outliers. When using the RANSAC algorithm the resulting plane parameters may vary between multiple repetitions depending on the randomly selected starting points but the algorithm allows higher flexibility for data with multiple planes. As seen in (Figure 5.15d) the fit with the highest proportion of inliers (points within a threshold) is selected, and outliers are neglected. By removing data points which were assigned to the initial plane model, multiple planes can be detected within a data set.

After the fit, the plane model is used to calculate translation and orientation with respect to the robot arm. The position, of the end-effector (tool-centre-point) is defined by a vector containing xyz coordinates for the translational part. In contrast, the orientation is defined using quaternions which simplifies mathematical operations compared to the usage of rotation matrices, e. g. when using Euler-angle convention.

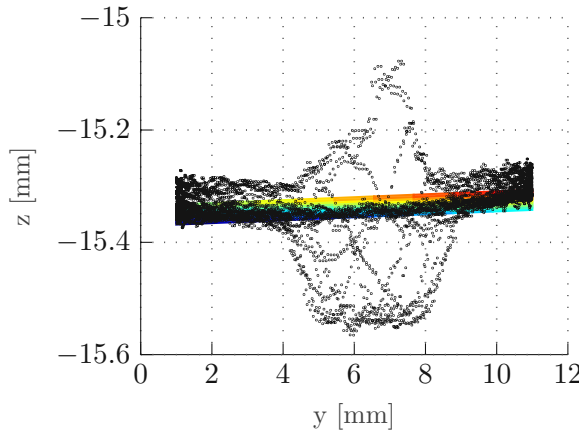
Figure 5.16 shows the result of two scans. For the first scan Figure 5.16a, a coarse scan is performed by using a Lissajous trajectory, followed by a plane fit utilizing a RANSAC algorithm. In general, the tilt of the measurement plane can also be determined by using a raster scan, but a Lissajous trajectory is selected since this trajectory type is also used during a feature detection process. Furthermore, as discussed in Section 4.3.2, for the complete process, e.g. for the measurement of welding spots, the robot repositioning is based on the data from the feature detection process. The optimal sensor distance is defined according to the point of minimal spot diameter specified in the datasheet, which is equal to a distance of 6 mm. The spot diameter depending on the distance is shown in Figure 4.5. The plane's resulting data is used to calculate a new position of the robot arm expressed in quaternions. The position data is sent automatically to the robot controller by utilizing socket communication between Matlab and the IRC5 controller, as mentioned



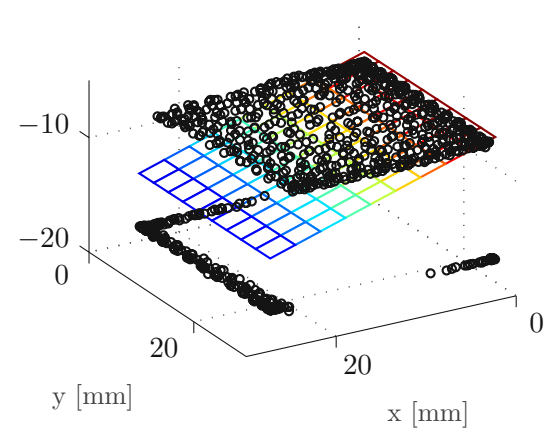
(a) Least-squares fit for spot weld area (cf. Figure 4.11).



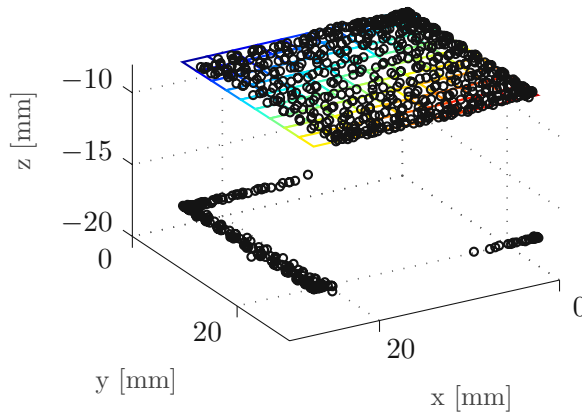
(b) Least-squares fit xz -plane.



(c) Least-squares fit yz -plane.



(d) Plane fit 10 mm step using least-squares.



(e) Plane fit 10 mm step using RANSAC.

Figure 5.15: Comparison of least-squares and RANSAC algorithm.

in Section 4.4.1. The robot performs the pose adjustment, and the high-resolution scan is performed. For this example an offset of approximately 15 mm is correct. The scan result is similar to Figure 5.12 and shows the harmonic pattern due to a combination of straightness, flatness and Abbe error.

As mentioned in previous chapters the lateral resolution is defined by the spot diameter on the surface [98]. Therefore, deterioration of lateral resolution is expected to occur if the sensor is not positioned at the optimal distance to the sample. Figure 5.16a shows the scan without repositioning process. The spot diameter at a distance of 21 mm is approximately $380 \times 300 \mu\text{m}$ which is equal to an increase by a factor of 6.9 and 6. The data shows a lower distinction and sharpness of edges and has a blurred appearance. The sample structures also show doubled edges that are expected to be a consequence of the large spot diameter. Also, the harmonic pattern is not visible anymore due to a blurring of the surface. By calculating the error between the CMM-scan and the scan in the optimal and non-optimal distance for 10 scans each, as discussed in Section 5.3, the overall error is found to be larger by a factor 30 to 40 % if the measurement system is positioned in the non-optimal distance.

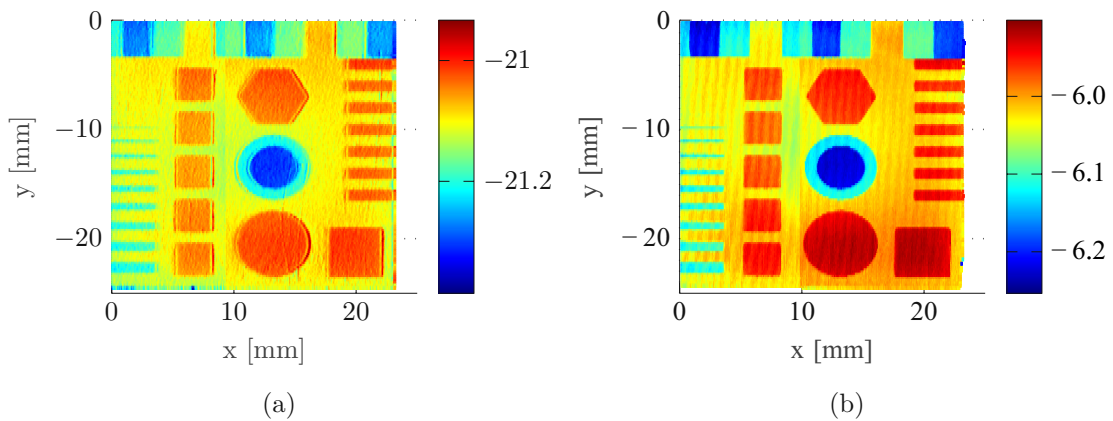


Figure 5.16: Scan without repositioning (a), scan with optimal sensor distance after repositioning (b).

Figure 5.17 shows the scan result for the section of the reference sample with the smallest structures. Figure 5.17a shows the result of the CMM. Figure 5.17b shows the result of the complete process as discussed above, by positioning the sensor in the optimal distance. Figure 5.17c once again shows the scan result for a non-ideal distance to the sample. By comparing the results to the desired dimensions of the 3D-printed part (cf. Figure 5.2), the SLA printer's limitations can be recognized. The smallest indentation with a desired width and depth of $100 \mu\text{m}$ at approximately $y = 16.2 \mu\text{m}$ is barely visible on the surface, and the data of the CMM scan indicates a maximum indentation of only $12 \mu\text{m}$. In addition, the average width of all indentations falls $50 \mu\text{m}$ below the desired dimensions according to the CMM-scan. Similar to Figure 5.16 it can be seen that the CMM scan and the scan in the optimal distance show a sharp delineation of edges. The

scan in the non-ideal distance shows a blurred appearance, and degradation of lateral resolution can be observed.

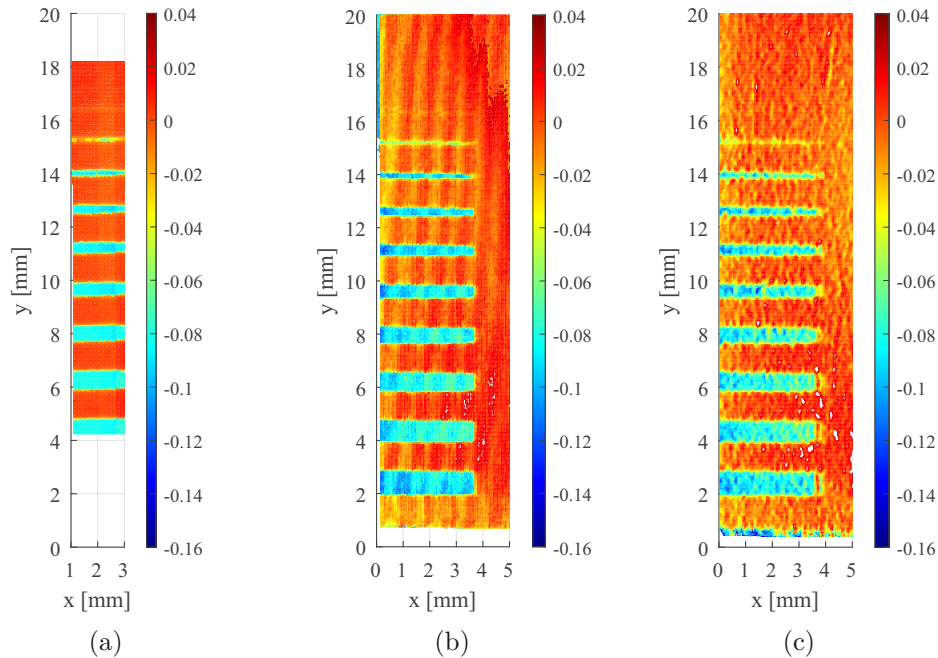


Figure 5.17: CMM-scan (a), sample in optimal distance (b) and scan in non-ideal distance (c).

Figure 5.18 shows a sectional view of the two smallest indentations of the reference sample with a desired width of $200\ \mu\text{m}$ and $100\ \mu\text{m}$, and a desired depth of $100\ \mu\text{m}$ for the three measurements referenced to the same coordination system. The CMM-scan leads to the conclusion that the smallest structures show a deviation from the desired dimension due to the limitations of the SLA printer. The indentations at $y = 15.1\ \text{mm}$ and $y = 16.2\ \text{mm}$ shows a depth of $66\ \mu\text{m}$ and $8\ \mu\text{m}$ respectively. Both indentations are clearly visible in the scan result when the metrology system is positioned at an optimal distance parallel to the surface. Nevertheless, the scan result is limited by random errors and the predominant error resulting from straightness, flatness and Abbe error the linear stages, as discussed in Section 5.3, which limits the achievable precision. This results in a measured indentation depth of $55\ \mu\text{m}$ and $15\ \mu\text{m}$. The scan without repositioning process for non-ideal distance to the sample shows a significantly worse result. The indentation at $y = 15.1\ \text{mm}$ shows a depth of only $15\ \mu\text{m}$ and the smallest indentation can't be observed. In addition, the measured distance shows a higher fluctuation on areas of constant height.

The measurement results lead to the conclusion that, by following the discussed procedure, the data of the coarse scan can be used to utilize the maximum possible resolution of an optical measurement system by reorienting and repositioning the measurement system mounted on the robot flange which leads to an improvement of the measurement result and reduction of the measurement error.

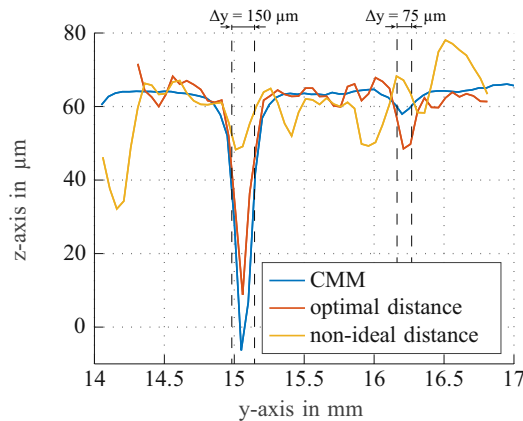


Figure 5.18: Sectional view of the two smallest indentations at $x = 3$ mm.

5.5 Error budget review

As discussed in Section 3.6, error sources are divided into systematic and random errors. This section starts with a summary of error sources that were characterised as systematic errors during the experiments and characterisation processes, followed by random errors and the resulting overall error.

The repeatability and accuracy of the stages was found to be $1.372 \mu\text{m}$ and $0.355 \mu\text{m}$, which is of interest for point-to-point measurements. For the motorized linear stages, mainly the dynamic behaviour is of interest, because it represents behaviour during a continuous scan process. The stages show a dominant harmonic component during phases of constant velocity with an amplitude of up to $2.9 \mu\text{m}$ as shown in Figure 4.22. This can be considered in a predictable manner and is therefore considered as systematic error. The triangulation sensor is characterized by the temperature behaviour, which can be modelled over time, e. g. by an exponential fit, and therefore can be compensated (Figure 4.26), and its repeatability of $1 \mu\text{m}$.

Furthermore, the utilization of Lissajous trajectories allows prediction of the impact of acceleration forces onto the measurement accuracy since the frequency of the sine-movement dominates the displacement error Figure 5.4. Therefore, to achieve optimal results, Lissajous trajectories should be preferred over raster scans for this application. Raster scans lead to a strong excitation of high-frequency components in the mechanical structure of the robot and the measurement system, especially at turning points due to acceleration forces. While phases of constant velocity (cf. Figure 5.4) also show dominant frequency components, whose amplitude decays over time, which could be formulated in a mathematical manner, if not, the data close to turning points has to be discarded if maximum precision is desired. For example, for one repetition of a bidirectional raster movement, including two acceleration and deceleration phases, data points corresponding to approximately 40% of the duration have to be neglected to avoid large errors and ease the creation of a mathematical model.

Considering those deterministic error sources in terms of a mathematical model during the data evaluation process, accuracy and precision can be improved dramatically. Nevertheless, the main sources of error of the positioning system, straightness, flatness and Abbe error, require more precise characterisation of the setup, which would exceed this thesis's scope.

As mentioned above, the sensor fulfils the specifications defined by the manufacturer and shows a repeatability of $1\ \mu\text{m}$. The influence of vibrations onto the sensor lead to a degradation of the repeatability from $1\ \mu\text{m}$ to $1.8\ \mu\text{m}$. The error sources were separated as described in Section 4.6.3. These led to the conclusion that the impact of floor vibrations present in the laboratory falls below the sensor resolution. Nevertheless, this evaluation goes for reasonably stable laboratory conditions. In an industrial environment, floor vibrations from heavy machinery might be the main reason for an additional loss in repeatability and accuracy, even though this impact can be compensated to a certain degree by using appropriate vibration-isolation techniques.

The next factor that leads to a degradation of the measurement resolution is the repeatability of the robot in combination with the optical measurement system. The varying spot diameter results in a change of lateral resolution over the measurement range. The evaluation of the robot performance has shown that the repeatability is mainly influenced by thermal drift, especially after a fresh start of the robotic system. The decay duration depends on velocity, acceleration, number of repetitions and duration of the movement. Under the assumption that the robot is positioned relative to the sample at a distance that minimizes the laser diameter, a maximum change of lateral resolution of $15\ \mu\text{m}/\text{mm}$ can occur. Therefore, by including thermal drift, which led to a maximum positioning change over time of approximately $180\ \mu\text{m}$ the lateral resolution deteriorates by $2.7\ \mu\text{m}$, which is equal to 4.9% of the spot diameter. In general, the structure (e. g. step height of a sample) has the most decisive impact on the lateral resolution. Nevertheless, a defined plane of the sample can always be scanned with the highest resolution due to the repositioning feature and optimal utilization of the measurement range.

The following Table 5.2 gives a final overview of all error sources and their type, with σ denoting the standard deviation of the random error source resulting from the validation of the system and its components. σ_d represents the error standard deviation according to the error budget from Section 3.6.

Error type	Characterization	σ	σ_d
Random	Floor vibrations σ_f	n.a.	67 nm
	Robot vibrations σ_r	499	150 nm
	Sensor noise σ_s	333	333 nm
	Linear stage position repeatability σ_p	457	667 nm

	Data synchronisation σ_{sync}	833	833	nm
	Robot repeatability along z-axis σ_{rz}	2	TBD	
Systematic	Triangulation sensor thermal drift			
	Linear stage dynamic behaviour			
	Abbe error of the linear stages (out-of-plane)			
	Abbe error of the linear stages (in-plane)			
	Straightness of the linear stages			
	Flatness of the linear stages			
	Robot warm-up phase			
	Acceleration forces depending on trajectory			

Table 5.2: Overview of systematic and random errors.

Similar to Section 3.6 the overall error standard deviation for the error along z-axis σ_z , the lateral error for point-to-point measurements σ_{pxy} and the lateral error for a continuous scanning motion σ_{cxy} , and their respective repeatability are calculated since these errors follow a normal distribution. The results show that the error budget serves as a good foundation for the selection of components. Nevertheless, the impact of robot vibrations on the out-of-plane error is larger than expected which leads to a deterioration of the out-of-plane repeatability by a factor of 1.6, not including floor vibrations.

$$\sigma_z = \sqrt{\sigma_r^2 + \sigma_s^2} = 592 \text{ nm} \quad (5.3)$$

$$R_z = 1777 \text{ nm} \quad R_{zd} = 1113 \text{ nm}$$

$$\sigma_{pxy} = \sqrt{\sigma_r^2 + \sigma_p^2} = 677 \text{ nm} \quad (5.4)$$

$$R_{pxy} = 2029 \text{ nm} \quad R_{pxyd} = 2058 \text{ nm}$$

$$\sigma_{cxy} = \sqrt{\sigma_r^2 + \sigma_{sync}^2} = 971 \text{ nm} \quad (5.5)$$

$$R_{cxy} = 2913 \text{ nm} \quad R_{cxyd} = 3009 \text{ nm}$$

5.6 Specification overview

This section gives a summary of the prototype's characteristics and lists the achieved specifications in Table 5.3.

The measurement volume is defined by the measurement range of the sensor and the linear stages. All further specifications are listed without considering the robot accuracy and repeatability since both only lead to an offset or tilt of the measurement plane and don't affect the actual measurement result. The robot accuracy can be compensated either manually or by utilizing the combined feature detection (see Section 4.3.2) and repositioning process (see Section 5.4). In addition, the robots repeatability was found to have a minimal impact on the lateral resolution as discussed in Section 4.6.2.

Out-of-plane and in-plane resolution are defined and limited by the sensor system. Accuracy and repeatability are defined and evaluated according to Section 5.3 and apply to the individual scan process. Repeatability is defined and evaluated according to Section 5.3.1 and applies to a repetitive scan process by following the complete measurement procedure according to Figure 4.13. Therefore, it is necessary to distinguish between these specifications.

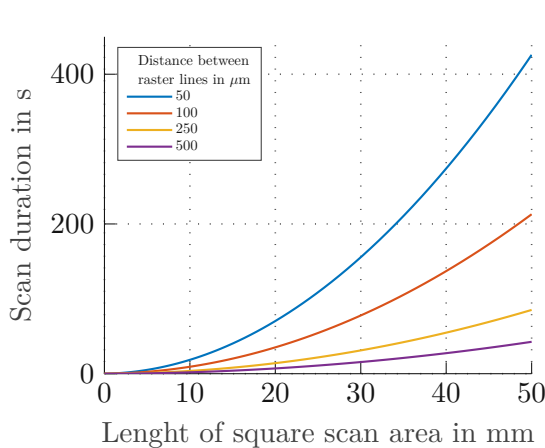
Specification	Value
Measurement volume xyz	50.8x50.8x25 mm
Out-of-plane resolution z	0.385 μm
In-plane resolution xy	50 μm
Accuracy in z	3.4 μm
Precision (individual scan) in z	22.2 μm
Repeatability (repetitive scan) in z	7.2 μm

Table 5.3: Main specifications of prototype components.

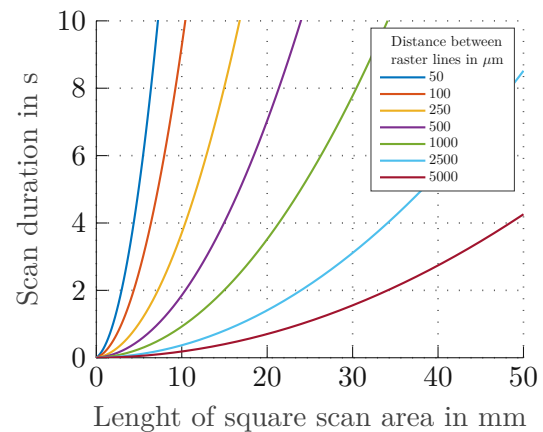
Figure 5.19 provides an overview of different aspects of the robot-based in-line measurement system's prototype. Figure 5.19.a shows the scan duration of a raster scan for different lengths of a square scan area for the maximum velocity of 120 mm/s and for different spacing of the raster lines. Since the linear stages cover a scan area up to 50.8x50.8 mm the scan can take up to multiple minutes for high-resolution scans. For industrial application, high-throughput and short scan duration is desired. This requires a trade-off between scan duration and resolution. Figure 5.19.b shows scan duration with a maximum time of 10 s over the length of a square scan area for a varying spacing of raster lines. As discussed in Section 5.1 high acceleration forces of raster scans lead to a lateral error, especially around turning points. If the error is not compensated, a lower acceleration is desired to minimize lateral error compared to the laser spot size of the triangulation sensor. Especially for large scan areas and high scan durations an increase in acceleration shows a limited reduction of the total duration as seen in Figure 5.19.c. If minimum scan time is desired, maximum acceleration and compensation of the resulting lateral error are desired and illustrated in Figure 5.19.d.

In general, the maximum velocity can limit the achievable lateral resolution. In this case, the sensor measurement frequency of 4 kHz exceeds the ratio of maximum velocity to sensor spot size by a factor of 1.67 by considering the minimal spot diameter of $50\ \mu\text{m}$. Therefore, the velocity does not limit the lateral resolution along the scan trajectory. The relation of lateral measurement point spacing to velocity is linear as seen in Figure 5.19d. This property has to be considered if stages with higher maximum velocity or a sensor with a lower sample rate are used. The used sensor allows an adjustment of the measurement frequency from 0.25 to 4 kHz. For a high-speed scanning system, the highest measurement frequency is desired to avoid motion blur.

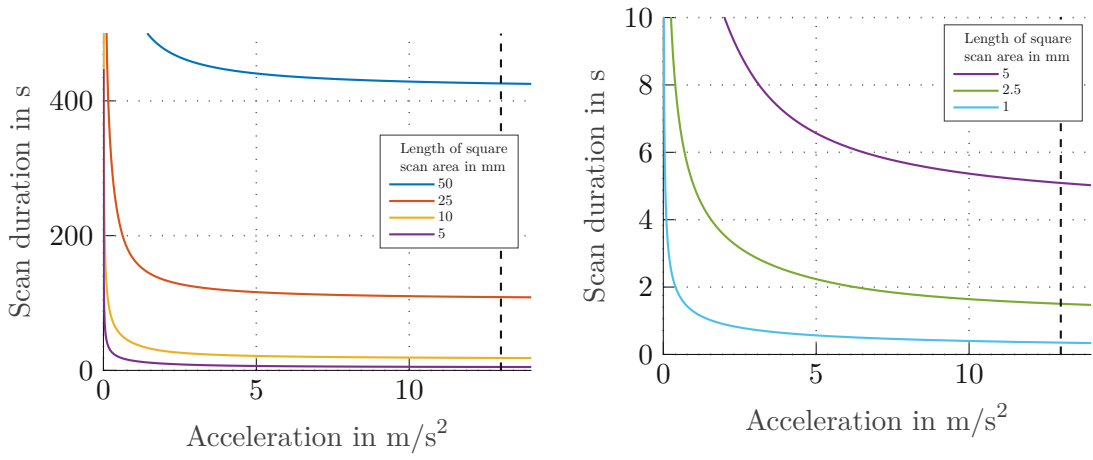
Figure 5.19.f and Figure 5.19.g show an estimation of the maximum scan time of a Lissajous trajectory that is required to detect a feature with a specific size under the assumption of a circular feature, e.g. a weld spot. A resolution greater or equal to the double sample size is demanded. As discussed in Section 2.3 the resolution shows a $1/k$ behaviour depending on the scan time, which can be realized by multiple frequency combination. Once again, it has to be considered that the maximum frequency depends on the range of motion due to the maximum velocity of the stage. For the figures one frequency is selected close to the maximum frequency while the second frequency is varied in 0.1 Hz steps.



(a) Scan duration for a square scan area.

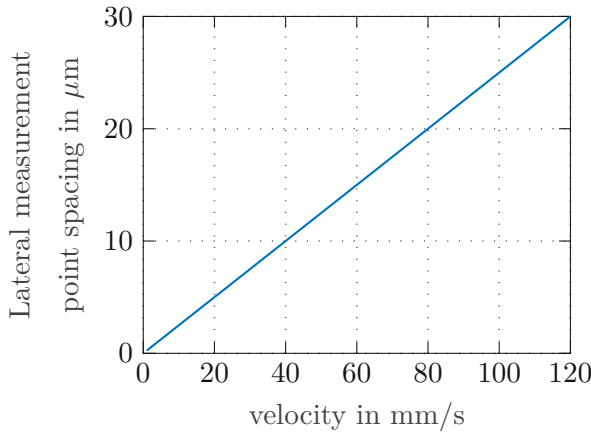


(b) Scan duration for a square scan area with maximum scan time $T = 10$ s.

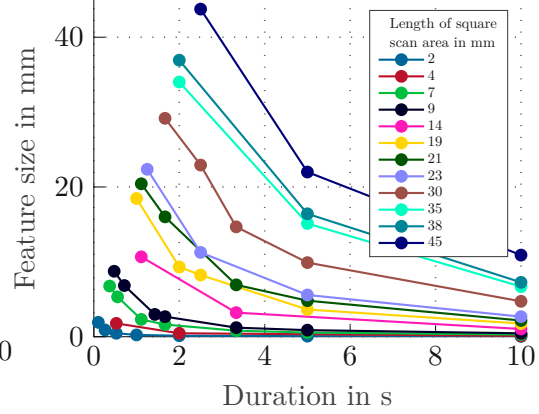


(c) Scan duration depending on the acceleration.

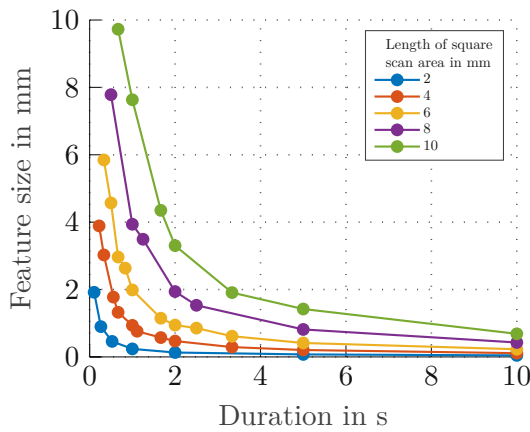
(d) Scan duration depending on the acceleration with maximum scan time $T = 10$ s.



(e) Lateral measurement point spacing depending on scan speed



(f) Maximum time to locate a feature.



(g) Maximum time to locate a feature for a maximum feature size of 10 mm.

Figure 5.19: Specifications of measurement system.

6 Conclusion and outlook

Within the course of this thesis, a fully automated robot-based in-line measurement system for optical surface inspection has been successfully designed and prototyped. This chapter summarizes findings related to this project and gives an outlook towards possible improvements on the existing prototype and the overall concept.

6.1 Conclusion

The robot-based in-line metrology system has been designed based on a dual-stage approach integrating an industrial robot arm to provide flexibility for the inspection of complex shapes and stepper-motor-based linear stages for performing a high-precision scanning motion. The system is equipped with a triangulation sensor. Compared to the typical state of the art inspection systems based on active stereo vision, as introduced in Section 2.4, this setup allows flexible surface inspection and 3D-imaging without the limitation of a fixed field of view and fixed lateral resolution and allows the usage of optical inspection systems that exceed the in-plane resolution of camera-based inspection systems by a factor of 10 and more. To compensate for manufacturing tolerances and allow adaptivity for samples of varying dimensions, the utilization of Lissajous trajectories and a feature detection algorithm provide an intelligent scan and measurement process as shown in Chapter 4.3. The resulting data of a coarse scan is used to adjust the robot pose and optimally utilize the optical sensor system's measurement range to achieve maximum resolution as shown in Section 5.4. By considering the task of surface inspection of spot welds, as discussed in Section 2.1, a typical spot weld with a diameter of 4 mm can be located within a maximum time of 1.5 s, within an area of 10x10 mm and can be scanned with the maximum possible lateral resolution of 50 μm within 3.5 s.

Based on the developed system and analysis the research questions formulated in Section 2.8 can be answered as follows:

Research question 1:

Is it possible to create a robot-based metrology system for optical surface inspection that provides single micrometre resolution, accuracy and repeatability in axial and lateral direction?

The analysis of the individual components and the overall system has shown that the main sources of random errors, characterized by their standard deviation, are sensor noise $\sigma_r = 333$ nm, robot vibrations $\sigma_r = 499$ nm, the repeatability of the linear stages $\sigma_p = 457$ nm when point-to-point measurements are performed, and an error during

data synchronization 833 nm when a continuous scanning motion is performed. The impact of floor vibrations present during the analysis and experiments has been found to fall below the sensor resolution of 382 nm for the laboratory environment. This results in an out-of-plane precision (3σ) of $1.78 \mu\text{m}$, an in-plane precision for point-to-point measurements of $2.03 \mu\text{m}$ and an in-plane precision for a continuous scanning motion of $2.91 \mu\text{m}$. The lateral error is considered small compared to the minimum spot size of $55 \times 50 \mu\text{m}$ of the triangulation sensor, which defines the lateral resolution. Furthermore, the evaluation process has shown that a combination of straightness, flatness and Abbe error has the strongest impact on achievable accuracy and precision (see Section 5.3). Without compensating for this error, an in-plane accuracy and precision of $3.4 \mu\text{m}$ and $22.2 \mu\text{m}$ is achieved. The repeatability between individual scan processes by executing the complete measurement procedure according to Section 4.4.2 is found to be $7.2 \mu\text{m}$. Therefore, to achieve a precision of at least single-digit micrometres, compensation of the remaining error and calibration is crucial. Given these results the first question can be answered with yes, it is possible for a laboratory environment by selecting suitable components and by performing proper calibration measures. Nevertheless, as discussed in Section 3.6 additional floor vibrations have to be considered and might have to be compensated for the application in an industrial field.

Research question 2:

Can error sources of the robot-based metrology system components be captured in a systematic manner to improve measurement accuracy, repeatability and overall performance, and can this knowledge be used to optimize the measurement process?

The experimental validation of the system's performance and the characterisation of the individual components according to Chapter 4 and Chapter 5 have shown that error sources can be captured systematically and divided into systematic and random errors. The creation of an error budget (see Section 3.6), which served as a criterion for the selection of individual components, has proved to be a good estimation for the resulting error of the prototype as discussed in Section 5.5. The main proportion of the error, which affects accuracy and precision, can be traced back to systematic errors which can be compensated. As mentioned above, the main source of error arises from the linear stage's straightness, flatness and Abbe error. As discussed in Section 3.6 compensation of these errors is possible but requires a complex calibration process that would exceed the scope of this thesis. Nevertheless the second question and can be answered with yes and additional measures, by using the data of a coarse scan to adjust the robot pose, to optimally utilize the measurement range of the triangulation sensor, have been proven to improve the final scan result as shown in Section 5.4.

6.2 Outlook

The final section of this thesis gives an outlook on future works and possible adaptations to increase the overall performance and flexibility of the robot-based metrology system. First of all, the source of the main error has to be treated. To compensate for straightness, flatness and Abbe error, different solutions are possible as discussed in Section 3.6. Suitable measurement setups which utilize either, a linear encoder as an optical displacement sensor, interferometers or capacitive sensors can be used to perform precise characterization of this deterministic error source. An alternative would be the usage of a different actuator or stage type. The system's functionality can be extended by using additional sensor systems, for example, laser-ultrasound testing systems. Either the position of excitation, detection or both can be varied using the xy-scan system. Ultrasonic testing usually requires constant distance to a sample, especially when using an optical microphone as a detector (cf. Section 2.1.1). Therefore, the triangulation laser can be used for feature detection, repositioning the robot, and surface inspection, while the laser-ultrasound system allows the detection of internal defects. Typically these applications set lower requirements on the precision of the positioning systems which eases the adaptation for a different non-destructive-testing sensor system.

For operation in an industrial environment, modelling of the robot arm and collision detection and avoidance measures are necessary. The next step would be to extend the system's functionality for the inspection of free-form surfaces. Pointcloud registration and stitching can be utilized to create 3D-scans of large-scale areas. By assuming repetitive scans of samples or bodies, an iterative-learning-control approach can be applied to improve the positioning performance of the robot-arm by utilizing the scan data as feedback.

Bibliography

- [1] D. Imkamp, R. Schmitt, and J. Berthold, Blick in die Zukunft der Fertigungsmesstechnik, *tm-Technisches Messen*, vol. 79, no. 10, pp. 433–439, 2012.
- [2] D. Imkamp, J. Berthold, M. Heizmann, K. Kniel, M. Peterek, R. Schmitt, J. Seidler, and K.-D. Sommer, Herausforderungen und Trends in der Fertigungsmesstechnik-Industrie 4.0, *Tm-Technisches Messen*, vol. 83, no. 7-8, pp. 417–429, 2016.
- [3] T.-F. Yao, A. Duenner, and M. Cullinan, In-line metrology of nanoscale features in semiconductor manufacturing systems, *Precision Engineering*, vol. 47, pp. 147–157, 2017.
- [4] O. Semeniuta, S. Dransfeld, and P. Falkman, Vision-based robotic system for picking and inspection of small automotive components, *IEEE International Conference on Automation Science and Engineering (CASE)*, pp. 549–554, 2016.
- [5] M. Liebens, A. Jourdain, J. De Vos, T. Vandeweyer, A. Miller, E. Beyne, S. Li, G. Bast, M. Stoerring, S. Hiebert, *et al.*, “In-line metrology for characterization and control of extreme wafer thinning of bonded wafers,” in *2017 28th Annual SEMI Advanced Semiconductor Manufacturing Conference (ASMC)*, IEEE, 2017, pp. 331–336.
- [6] M. Sackewitz, *Marktstudie 3-D-Messtechnik in der deutschen Automobil-und Zuliefererindustrie*. Fraunhofer Verlag, 2010.
- [7] *Kuka AG, Industrieroboter von KUKA*, <https://www.kuka.com/de-de/produkte-leistungen/robotersysteme/industrieroboter>, Accessed: 2020-30-12.
- [8] *ABB AG, ABB Robotics*, <https://new.abb.com/products/robotics/de>, Accessed: 2020-30-12.
- [9] R.-F. Fung, Y.-L. Hsu, and M.-S. Huang, System identification of a dual-stage XY precision positioning table, *Precision Engineering*, vol. 33, no. 1, pp. 71–80, 2009.
- [10] H. Zhu, C. K. Pang, and T. J. Teo, Integrated servo-mechanical design of a fine stage for a coarse/fine dual-stage positioning system, *IEEE/ASME Transactions on Mechatronics*, vol. 21, no. 1, pp. 329–338, 2015.
- [11] J. Segeborn, J. S. Carlson, K. Wärmefjord, and R. Söderberg, Evaluating genetic algorithms on welding sequence optimization with respect to dimensional variation and cycle time, *International Design Engineering Technical Conferences and Computers and Information in Engineering Conference*, vol. 54822, pp. 697–704, 2011.
- [12] M. Zhou, H. Zhang, and S. Hu, Relationships between quality and attributes of spot welds, *WELDING JOURNAL-NEW YORK-*, vol. 82, no. 4, 72–S, 2003.

- [13] A. Standard, Recommended Practices for Test Methods for Evaluating the Resistance Spot Welding Behavior of Automotive Sheet Steel Materials, *AWS D8.9M*, 2012.
- [14] Y.-J. Xia, Z.-W. Su, M. Lou, Y.-B. Li, and B. E. Carlson, Online precision measurement of weld indentation in resistance spot welding using servo gun, *IEEE Transactions on Instrumentation and Measurement*, vol. 69, no. 7, pp. 4465–4475, 2019.
- [15] C. Mineo, S. G. Pierce, P. I. Nicholson, and I. Cooper, Robotic path planning for non-destructive testing—A custom MATLAB toolbox approach, *Robotics and Computer-Integrated Manufacturing*, vol. 37, pp. 1–12, 2016.
- [16] K. Ikeuchi, Y. Matsushita, R. Sagawa, H. Kawasaki, Y. Mukaigawa, R. Furukawa, and D. Miyazaki, *Active Lighting and Its Application for Computer Vision*. Springer, 2020.
- [17] LMI Technologies Inc., *Automatisierung. Inspektion. Optimierung. Gocator, Snapshot Sensoren*, <https://lmi3d.com/de/products/gocator/g3/snapshot-sensors>, Accessed: 2020-11-12, 2020.
- [18] MICRO-EPSILON MESSTECHNIK GmbH & Co. KG, *Laser-Sensoren für Weg, Abstand, Position*, <https://www.micro-epsilon.de/displacement-position-sensors/laser-sensor/>, Accessed: 2020-11-12, 2020.
- [19] Keyence, *Oberflächenabtastender konfokaler Laser-Wegmesssensor - Modellreihe LT-9000*, <https://www.keyence.eu/dede/products/measure/laser-1d/lt-9000/specs/>, Accessed: 2020-11-13, 2020.
- [20] MICRO-EPSILON MESSTECHNIK GmbH & Co. KG, »Spektra-kuläre« Messungen mit konfokal-chromatischen Sensoren, *Mechatronik*, vol. 6, pp. 18–21, 2018.
- [21] —, *Konfokale Sensorsysteme für Weg, Abstand, Position und Dicke*, <https://www.micro-epsilon.de/displacement-position-sensors/confocal-sensor/>, Accessed: 2020-11-13, 2020.
- [22] R. Singh, *Applied welding engineering: processes, codes, and standards*. Butterworth-Heinemann, 2020.
- [23] J. P. Kruth, M. Bartscher, S. Carmignato, R. Schmitt, L. De Chiffre, and A. Weckenmann, Computed tomography for dimensional metrology, *CIRP annals*, vol. 60, no. 2, pp. 821–842, 2011.
- [24] M. Müller, I. de Sena Oliveira, S. Allner, S. Ferstl, P. Bidola, K. Mechlem, A. Fehringer, L. Hehn, M. Dierolf, K. Achterhold, *et al.*, Myoanatomy of the velvet worm leg revealed by laboratory-based nanofocus X-ray source tomography, *Proceedings of the National Academy of Sciences*, vol. 114, no. 47, pp. 12 378–12 383, 2017.
- [25] J. M. Warnett, V. Titarenko, E. Kiraci, A. Attridge, W. R. Lionheart, P. J. Withers, and M. A. Williams, Towards in-process x-ray CT for dimensional metrology, *Measurement Science and Technology*, vol. 27, no. 3, p. 035 401, 2016.

- [26] Z. Qu, P. Jiang, and W. Zhang, Development and Application of Infrared Thermography Non-Destructive Testing Techniques, *Sensors*, vol. 20, no. 14, p. 3851, 2020.
- [27] F. Jonietz, P. Myrach, M. Rethmeier, H. Suwala, and M. Ziegler, Laser based spot weld characterization, *AIP Conference Proceedings*, vol. 1706, no. 1, p. 100 010, 2016.
- [28] P. Myrach, F. Jonietz, D. Meinel, H. Suwala, and M. Ziegler, Calibration of thermographic spot weld testing with X-ray computed tomography, *Quantitative InfraRed Thermography Journal*, vol. 14, no. 1, pp. 122–131, 2017.
- [29] L. Drain, *Laser Ultrasonics Techniques and Applications*, 2019.
- [30] W. Rohringer, R. Sommerhuber, L. Csaszar, N. Panzer, S. Wald, B. Fischer, H. Garrecht, F. Grüner, and J. Frick, Material characterization via contact-free detection of surface waves using an optical microphone, *Proceedings on the 5th International Conference on Sustainable Construction Materials and Technologies SCMT5*, vol. 1, pp. 361–373, 2019.
- [31] B. Fischer, Optical microphone hears ultrasound, *Nature Photonics*, vol. 10, no. 6, pp. 356–358, 2016.
- [32] P. C. Krause, O. Wasynczuk, and S. D. Pekarek, *Electromechanical motion devices*. John Wiley & Sons, 2012, vol. 90.
- [33] S. Derammelaere, B. Vervisch, F. De Belie, B. Vanwalleghem, J. Cottyn, P. Cox, G. Van den Abeele, K. Stockman, and L. Vandeveldel, The efficiency of hybrid stepping motors: Analyzing the impact of control algorithms, *IEEE Industry Applications Magazine*, vol. 20, no. 4, pp. 50–60, 2014.
- [34] Zaber Technologies Inc., *Linear Stages*, <https://www.zaber.com/products/linear-stages>, Accessed: 2020-11-13, 2020.
- [35] S. Ito and G. Schitter, Comparison and classification of high-precision actuators based on stiffness influencing vibration isolation, *IEEE/ASME Transactions on Mechatronics*, vol. 21, no. 2, pp. 1169–1178, 2015.
- [36] Physik Instrumente GmbH & Co.KG, *Miniature Linear Stages*, <https://www.physikinstrumente.com/en/products/linear-stages/miniature-linear-stages/>, Accessed: 2020-11-13, 2020.
- [37] —, *Nanopositioning Piezo Flexure Stages*, <https://www.physikinstrumente.com/en/products/nanopositioning-piezo-flexure-stages/>, Accessed: 2020-11-13, 2020.
- [38] A. Bazaei, Y. K. Yong, and S. R. Moheimani, High-speed Lissajous-scan atomic force microscopy: Scan pattern planning and control design issues, *Review of Scientific Instruments*, vol. 83, no. 6, p. 063 701, 2012.
- [39] T. Tuma, J. Lygeros, A. Sebastian, and A. Pantazi, Optimal scan trajectories for high-speed scanning probe microscopy, *2012 American Control Conference (ACC)*, pp. 3791–3796, 2012.

- [40] B. P. Lathi and R. A. Green, *Linear systems and signals*. Oxford University Press New York, 2005, vol. 2.
- [41] E. Csencsics and G. Schitter, System design and control of a resonant fast steering mirror for lissajous-based scanning, *IEEE/ASME Transactions on Mechatronics*, vol. 22, no. 5, pp. 1963–1972, 2017.
- [42] T. Tuma, J. Lygeros, V. Kartik, A. Sebastian, and A. Pantazi, High-speed multiresolution scanning probe microscopy based on Lissajous scan trajectories, *Nanotechnology*, vol. 23, no. 18, p. 185 501, 2012.
- [43] I. Mahmood and S. R. Moheimani, Fast spiral-scan atomic force microscopy, *Nanotechnology*, vol. 20, no. 36, p. 365 503, 2009.
- [44] E. Csencsics, S. Ito, J. Schlarp, M. Thier, and G. Schitter, Hochpräzise roboter-basierte 3D-In-Prozess-Messtechnik, *e & i Elektrotechnik und Informationstechnik*, vol. 135, no. 6, pp. 382–388, 2018.
- [45] G. B. de Sousa, A. Olabi, J. Palos, and O. Gibaru, 3D metrology using a collaborative robot with a laser triangulation sensor, *Procedia Manufacturing*, vol. 11, pp. 132–140, 2017.
- [46] Kuka AG, KUKA Industrierobotik Niedrige Traglast, 2018.
- [47] ABB Automation GmbH, IRB 1600 Industrieroboter, 2017.
- [48] FANUC Europe Corporation, ARC Mate 100iD/8L, 2020.
- [49] MOTOMAN MPX1950 Kompakter Roboter für flexibles Lackieren, Interface Manual IDS3010, 2019.
- [50] *LMI Technologies Inc.*, *Gocator Linienprofilsensoren*, <https://lmi3d.com/de/products/gocator/g2/line-profile-sensors>, Accessed: 2020-30-12.
- [51] *LMI Technologies Inc.*, *Gocator Snapshot-Sensoren*, <https://www.kuka.com/de/de/produkte-leistungen/robotersysteme/industrieroboter>, Accessed: 2020-30-12.
- [52] *Creaform*, *R-Series Schnelle und präzise 3D-Scanlösungen für die automatisierte Qualitätssicherung*, <https://www.creaform3d.com/de/messtechnik/produkte/automatische-pruefungsloesungen-der-r-serie>, Accessed: 2020-30-12.
- [53] *API Metrology*, *Scanning & Inspection*, <https://apimetrology.com/scanning-and-inspection/>, Accessed: 2020-30-12.
- [54] *Creaform*, *R-Series, Schnelle und präzise 3D-Scanlösung für die automatisierte Qualitätssicherung*, <https://www.creaform3d.com/de/messtechnik/produkte/automatische-pruefungsloesungen-der-r-serie>, Accessed: 2020-02-05.
- [55] *Allied Automation, Inc.*, *Smart 3D Robot Vision with Gocator*, <https://www.allied-automation.com/smart-3d-robot-vision-with-gocator-discover-the-universal-robots-ur-hardware-kits-from-lmi-technologies/>, Accessed: 2020-02-05.

- [56] *Automated Precision, Inc (API), Scanning & Inspection - SMART FACTORY INSPECTION SYSTEMS (SFIS)*, <https://apimetrology.com/scanning-and-inspection/>, Accessed: 2020-02-05.
- [57] C. Mineo, C. MacLeod, M. Morozov, S. G. Pierce, R. Summan, T. Rodden, D. Kahani, J. Powell, P. McCubbin, C. McCubbin, *et al.*, Flexible integration of robotics, ultrasonics and metrology for the inspection of aerospace components, *AIP conference proceedings*, vol. 1806, no. 1, p. 020 026, 2017.
- [58] C. Deniz and M. Cakir, In-line stereo-camera assisted robotic spot welding quality control system, *Industrial Robot: An International Journal*, vol. 45, no. 1, pp. 54–63, 2018.
- [59] Y. Javadi, N. E. Sweeney, E. Mohseni, C. N. MacLeod, D. Lines, M. Vasilev, Z. Qiu, R. K. Vithanage, C. Mineo, T. Stratoudaki, *et al.*, In-process calibration of a non-destructive testing system used for in-process inspection of multi-pass welding, *Materials & Design*, vol. 195, p. 108 981, 2020.
- [60] R. Söderberg, K. Wärmefjord, L. Lindkvist, and R. Berlin, The influence of spot weld position variation on geometrical quality, *CIRP annals*, vol. 61, no. 1, pp. 13–16, 2012.
- [61] R. Szeliski, *Computer vision: algorithms and applications*. Springer Science & Business Media, 2010.
- [62] J. Canny, A computational approach to edge detection, *IEEE Transactions on pattern analysis and machine intelligence*, no. 6, pp. 679–698, 1986.
- [63] D. G. Lowe, Distinctive image features from scale-invariant keypoints, *International journal of computer vision*, vol. 60, no. 2, pp. 91–110, 2004.
- [64] H. Bay, A. Ess, T. Tuytelaars, and L. Van Gool, Speeded-up robust features (SURF), *Computer vision and image understanding*, vol. 110, no. 3, pp. 346–359, 2008.
- [65] S. Leutenegger, M. Chli, and R. Y. Siegwart, BRISK: Binary robust invariant scalable keypoints, *2011 International conference on computer vision*, pp. 2548–2555, 2011.
- [66] B. Favre-Bulle, *Automatisierung komplexer Industrieprozesse: Systeme, Verfahren und Informationsmanagement*. Springer-Verlag, 2013.
- [67] R. Dietrich, Industrial Ethernet... from the Office to the Machineworld wide, *HARTING GmbH & Co. KG*, 2004.
- [68] G. Schnell, *Bussysteme in der Automatisierungs-und Prozesstechnik: Grundlagen, Systeme und Trends der industriellen Kommunikation*. Springer-Verlag, 2019.
- [69] P. Danielis, J. Skodzik, V. Altmann, E. B. Schweissguth, F. Golatowski, D. Timmermann, and J. Schacht, Survey on real-time communication via ethernet in industrial automation environments, *Proceedings of the 2014 IEEE Emerging Technology and Factory Automation (ETFA)*, pp. 1–8, 2014.

- [70] M. Wollschlaeger, T. Sauter, and J. Jasperneite, The future of industrial communication: Automation networks in the era of the internet of things and industry 4.0, *IEEE industrial electronics magazine*, vol. 11, no. 1, pp. 17–27, 2017.
- [71] G. Wellenreuther and D. Zastrow, *Automatisieren mit SPS: Theorie und Praxis*. Springer-Verlag, 2005.
- [72] MICRO-EPSILON MESSTECHNIK GmbH & Co. KG *Blue-Laser-Triangulationssensoren für schwierige Oberflächentypen*, <https://www.micro-epsilon.de/displacement-position-sensors/laser-sensor/BL-Laser-sensors/>, Accessed: 2020-24-11.
- [73] ABB AG, *IRB 2600*, <https://new.abb.com/products/robotics/industrial-robots/irb-2600>, Accessed: 2020-02-03.
- [74] Physik Instrumente GmbH & Co.KG, *XY Stages*, <https://www.physikinstrumente.com/en/products/xy-stages/>, Accessed: 2020-02-07.
- [75] Zaber Technologies Inc., *XY, XYZ & Gantry Stages*, <https://www.zaber.com/products/xy-xyz-gantry-systems>, Accessed: 2020-02-07.
- [76] R. M. Schmidt, G. Schitter, and A. Rankers, *The Design of High Performance Mechatronics-: High-Tech Functionality by Multidisciplinary System Integration*. Ios Press, 2020.
- [77] M. Thier, R. Saathof, A. Sinn, R. Hainisch, and G. Schitter, Six degree of freedom vibration isolation platform for in-line nano-metrology, *IFAC-PapersOnLine*, vol. 49, no. 21, pp. 149–156, 2016.
- [78] R. Saathof, M. Thier, R. Hainisch, and G. Schitter, Integrated system and control design of a one DoF nano-metrology platform, *Mechatronics*, vol. 47, pp. 88–96, 2017.
- [79] MICRO-EPSILON MESSTECHNIK GmbH & Co. KG *Laser-Sensoren f $\frac{1}{4}$ r Weg, Abstand, Position*, <https://www.micro-epsilon.de/displacement-position-sensors/laser-sensor/>, Accessed: 2020-12-11.
- [80] Zaber Technologies Inc., *STEP file for the LSM050-E*, <https://www.zaber.com/products/linear-stages/LSM-E/noAD/details/LSM050B-E03T4/documents>, Accessed: 2021-01-25, 2020.
- [81] R. Leach, *Fundamental principles of engineering nanometrology*. Elsevier, 2014.
- [82] A. Kimura, W. Gao, and Z. Lijiang, Position and out-of-straightness measurement of a precision linear air-bearing stage by using a two-degree-of-freedom linear encoder, *Measurement Science and Technology*, vol. 21, no. 5, p. 054005, 2010.
- [83] K.-I. Lee, J.-C. Lee, and S.-H. Yang, The optimal design of a measurement system to measure the geometric errors of linear axes, *The International Journal of Advanced Manufacturing Technology*, vol. 66, no. 1-4, pp. 141–149, 2013.
- [84] Y. He, R. Li, K. Fan, Q. Huang, P. Hu, Y. Wang, W. Liu, and Y. Hu, Abbe error compensation for a micro/nano CMM with a coplanar stage, *Journal of Physics: Conference Series*, vol. 1379, no. 1, p. 012032, 2019.

- [85] DIN EN 60825-1, *Safety of laser products - Part 1: Equipment classification and requirements*, Norm, 2015.
- [86] D. H. Murcia, M. Genedy, and M. R. Taha, Examining the significance of infill printing pattern on the anisotropy of 3D printed concrete, *Construction and Building Materials*, vol. 262, p. 120 559, 2020.
- [87] A. J. Fleming and A. G. Wills, Optimal periodic trajectories for band-limited systems, *IEEE Transactions on Control Systems Technology*, vol. 17, no. 3, pp. 552–562, 2009.
- [88] M. Dinham and G. Fang, Autonomous weld seam identification and localisation using eye-in-hand stereo vision for robotic arc welding, *Robotics and Computer-Integrated Manufacturing*, vol. 29, no. 5, pp. 288–301, 2013.
- [89] K. Bowyer, C. Kranenburg, and S. Dougherty, Edge detector evaluation using empirical ROC curves, *Computer Vision and Image Understanding*, vol. 84, no. 1, pp. 77–103, 2001.
- [90] P. Arbelaez, M. Maire, C. Fowlkes, and J. Malik, Contour detection and hierarchical image segmentation, *IEEE transactions on pattern analysis and machine intelligence*, vol. 33, no. 5, pp. 898–916, 2010.
- [91] DIN EN ISO 18595, *Resistance welding - Spot welding of aluminium and aluminium alloys- Weldability, welding and testing*, Norm, 2007.
- [92] H. J. Eichler and J. Eichler, *Laser: Bauformen, Strahlführung, Anwendungen*. Springer-Verlag, 2015.
- [93] A. S. AG, Interface Manual IDS3010, *attoSENSORICS Ultra Precision Sensors*, vol. 1.4.0, 2017.
- [94] ISO 9283, *Manipulating industrial robots- Performance criteria and related test methods*, Norm, 1998.
- [95] M. Slamani, A. Nubiola, and I. Bonev, Assessment of the positioning performance of an industrial robot, *Industrial Robot: An International Journal*, 2012.
- [96] J. Bryan, International status of thermal error research (1990), *CIRP annals*, vol. 39, no. 2, pp. 645–656, 1990.
- [97] P. J. Besl and N. D. McKay, Method for registration of 3-D shapes, *Sensor fusion IV: control paradigms and data structures*, vol. 1611, pp. 586–606, 1992.
- [98] J. Schlarp, E. Csencsics, and G. Schitter, Design and evaluation of an integrated scanning laser triangulation sensor, *Mechatronics*, vol. 72, p. 102 453, 2020.
- [99] C. Haider, “Coordinate measuring machine for simultaneous double-sided optical surface metrology using a confocal chromatic sensor,” Master thesis, Advanced Mechatronic Systems Group, 2020.
- [100] J. H. Friedman, J. L. Bentley, and R. A. Finkel, An algorithm for finding best matches in logarithmic expected time, *ACM Transactions on Mathematical Software (TOMS)*, vol. 3, no. 3, pp. 209–226, 1977.

- [101] C. Chinrungrueng and A. Suvichakorn, Fast edge-preserving noise reduction for ultrasound images, *IEEE Transactions on Nuclear Science*, vol. 48, no. 3, pp. 849–854, 2001.
- [102] M. A. Fischler and R. C. Bolles, Random sample consensus: a paradigm for model fitting with applications to image analysis and automated cartography, *Communications of the ACM*, vol. 24, no. 6, pp. 381–395, 1981.

Eidesstattliche Erklärung

Hiermit erkläre ich, dass die vorliegende Arbeit gemäß dem Code of Conduct - Regeln zur Sicherung guter wissenschaftlicher Praxis (in der aktuellen Fassung des jeweiligen Mitteilungsblattes der TU Wien), insbesondere ohne unzulässige Hilfe Dritter und ohne Benutzung anderer als der angegebenen Hilfsmittel, angefertigt wurde. Die aus anderen Quellen direkt oder indirekt übernommenen Daten und Konzepte sind unter Angabe der Quelle gekennzeichnet. Die Arbeit wurde bisher weder im In- noch im Ausland in gleicher oder in ähnlicher Form in anderen Prüfungsverfahren vorgelegt.

Vienna, April 2021



Naverschnigg Christopher, BSc.